

**APPLICATION OF CONJUGATED
CUCURBIT[8]URIL PORPHYRIN
SUPRAMOLECULAR ASSEMBLY IN
ELECTROCHEMICAL HYDROGEN
GENERATION**

A THESIS SUBMITTED TO
THE GRADUATE SCHOOL OF ENGINEERING AND SCIENCE
OF BILKENT UNIVERSITY
IN PARTIAL FULFILLMENT OF THE REQUIREMENTS FOR
THE DEGREE OF
MASTER OF SCIENCE
IN
MATERIALS SCIENCE AND NANOTECHNOLOGY

By
Bouthaina Aoudi
August 2020

Application of Conjugated Cucurbit[8]uril – Porphyrin supramolecular
assembly in Electrochemical Hydrogen Generation

By Bouthaina Aoudi

August 2020

We certify that we have read this thesis and that in our opinion it is fully adequate,
in scope and in quality, as a thesis for the degree of Master of Science.

Dönüş Tuncel(Advisor)

İrem Erel Göktepe

Ferdi Karadaş

Approved for the Graduate School of Engineering and Science:

Ezhan Karaşan
Director of the Graduate School

ABSTRACT

APPLICATION OF CONJUGATED CUCURBIT[8]URIL PORPHYRIN SUPRAMOLECULAR ASSEMBLY IN ELECTROCHEMICAL HYDROGEN GENERATION

Bouthaina Aoudi

M.S. in Materials science and nanotechnology

Advisor: Dönüş Tuncel

August 2020

The ever-increasing demands for energy have encouraged an enormous consumption of fossil fuels worldwide. This has presented major concerns due to their limited resources and serious environmental issues. Therefore, the search for an alternative clean energy fuel has been intensively under study. In the past decade, hydrogen has attracted great attention as a promising fuel for the future. Hydrogen is an eco-friendly fuel that is readily abundant, highly efficient and clean since water is its only combustion product. Herein, this thesis highlights the synthesis and characterization of a novel supramolecular assembly based on cucurbit [8] uril -porphyrin functionalized on electrochemically reduced graphene oxide sheets for application in electrochemical hydrogen evolution. The study conveys optimization procedures for choosing the best catalytic system. Electrochemical analysis including potentiometry, cyclic voltammetry, chronoamperometry and electrochemical impedance spectroscopy were used to evaluate activity and stability. Characterization techniques were also performed to analyze the morphology and chemical structures of composites. Electrochemical studies demonstrated that ERGO: Ni-P composite (which comprises of a layer of graphene oxide drop-casted on FTO followed by a layer of nickel CB[8]-porphyrin) can serve as an excellent electrocatalyst for hydrogen evolution in alkaline medium. The composite exhibited high activity (onset potential \sim -20 mV, 56.9 mmol h⁻¹g⁻¹ hydrogen, faradaic efficiency of 93%), remarkable rate of charge transfer ($R_{ct} \sim$ 210 Ω), large electrochemical surface area ($C_{dl} \sim$ 1.67 mFcm⁻²) and significant stability without requiring additional noble metals.

Keywords: supramolecular electrocatalyst, cucurbituril, water-splitting, electrochemical hydrogen production, porphyrin, graphene oxide.

ÖZET

ELEKTROKİMYASAL HİDROJEN ÜRETİMİNDE KONJUGE KÜKÜRBIT[8]ÜRİL-PORFİRİN SUPRAMOLEKÜLER DÜZENEGİNİN UYGULANMASI

Bouthaina Aoudi

Malzeme Bilimi ve Nanoteknoloji, Yüksek Lisans

Tez Danışmanı: Dönüş Tuncel

Ağustos 2020

Sürekli artan enerji talepleri, dünya çapında muazzam miktarda fosil yakıt tüketimine sebep oldu. Bu durum, sınırlı kaynaklar ve ciddi çevre sorunları nedeniyle büyük endişeler ortaya çıkarmıştır. Bu nedenle, alternatif temiz bir enerji yakıtı arayışı yoğun bir şekilde incelenmektedir. Son on yılda hidrojen, gelecek için umut vaat eden bir yakıt olarak büyük ilgi görmüştür. Hidrojen kolayca bol miktarda bulunan, yüksek verimli ve tek yanma ürünü su olduğu için temiz, çevre dostu bir yakıttır. Bu tezde elektrokimyasal hidrojen evriminde uygulama için elektrokimyasal olarak indirgenmiş grafen oksit tabakaları üzerinde işlevselleştirilmiş kükürbit[8]üril-porfirine dayanan yeni bir supramoleküler düzeneğin sentezini ve karakterizasyonu vurgulanmaktadır. Çalışma, en iyi katalitik sistemi seçmek için optimizasyon prosedürlerini aktarıyor. Aktiviteyi ve stabiliteyi değerlendirmek için potansiyometri, döngüsel voltametri, kronoamperometri ve elektrokimyasal empedans spektroskopisini içeren elektrokimyasal analizler kullanıldı. Kompozitlerin morfolojisini ve kimyasal yapılarını analiz etmek için karakterizasyon teknikleri de uygulandı. Elektrokimyasal çalışmalar, ERGO: Ni-P kompozitinin (FTO üzerine damla dökülmüş bir grafen oksit tabakasından ve ardından bir nikel KB[8]-porfirin tabakasından oluşan) alkali ortamda hidrojen oluşumu için mükemmel bir elektrokatalizör görevi görebileceğini göstermiştir. Kompozit ek asal metaller gerektirmeden yüksek aktivite (başlangıç potansiyeli ~ -20 mV, 56.9 mmol $\text{h}^{-1}\text{g}^{-1}$ hidrojen, %93 faradaik verimliliği), dikkat çekici yük aktarım oranı ($R_{ct} \sim 210$ Ω), geniş elektrokimyasal yüzey alanı ($C_{dl} \sim 1.67$ mF cm^{-2}) ve önemli stabilite göstermiştir.

Anahtar sözcükler: supramoleküler elektrokatalizör, kükürbitüril, su ayırma,

elektrokimyasal hidrojen üretimi, porfirin, grafen oksit.

Acknowledgement

First and Foremost, I would like to express my sincere gratitude to my supervisor Assoc.Prof.Dönüş Tuncel for her exceptional guidance and immense knowledge that has greatly helped me fulfil my thesis studies. I would like to thank committee members Assoc.Prof.İrem Erel Göktepe and Asst.Prof.Ferdi Karadaş for their time and valuable efforts.

I want to extend my thanks to all faculty members and staff of UNAM and chemistry department for their tremendous help and contributions. I also thank Bilkent University, UNAM, and TÜBİTAK for their financial support throughout my master's studies. I am thankful to all present and former members of Prof. Tuncel's group, especially Melis Özkan, Yasaman Sheidaei and Aisan Khaligh for their valuable assistance and amazing energies. I am deeply grateful for Melis Özkan, Hüseyin Can Çamiçi, Doğu Özyiğit, Merve Üstünelik, Ilkay Çisil Köksaldı, Gökçe Özkul and Kerem Kurban for their precious friendship and treasured memories. I am very lucky I got to meet such wonderful people, thank you all for adding something special to my life.

My acknowledgement would be incomplete without thanking the biggest source of my strength, my family. I am forever indebted to my father Tarek Aoudi and mother Nazek Arabi, for their continuous and unparalleled love and support that shaped the person I am today. Not to mention, my success wouldn't have been possible without the three backbones in my life, my brothers Imad, Abdelrahman and Hussain who always believed in me and encouraged me to pursue my dreams. Finally, my special thanks go to my best friend and my sister, Joudi Maskoun for her presence by my side in every step. This journey would not have been possible if it wasn't for them, and I dedicate this milestone to them.

Contents

1	Introduction	1
1.1	Hydrogen as an alternative fuel	1
1.1.1	Hydrogen production methods	2
1.1.2	Applications of Hydrogen	5
1.2	Electrochemical water splitting	7
1.2.1	Thermodynamics	7
1.2.2	Factors affecting efficiency of the electrochemical cell	9
1.2.3	Electrocatalysts for HER	10
1.3	Activity parameters for HER	18
1.3.1	Overpotentials	18
1.3.2	Tafel plots	19
1.3.3	Turnover Frequency (TOF)	22
1.3.4	Faradaic Efficiency (FE)	23

1.3.5	Electrochemical Active Surface area (ECSA)	23
1.3.6	Electrochemical impedance spectroscopy (EIS)	24
1.3.7	Amount of hydrogen produced	25
1.4	Aim of study	26
2	EXPERIMENTAL AND INSTRUMENTATION	27
2.1	Materials	27
2.2	Synthesis	28
2.2.1	Synthesis of CB8-porphyrin assembly	28
2.2.2	Synthesis of graphene oxide	30
2.3	Experimental	30
2.3.1	Experimental setup	30
2.3.2	Sample preparation for electrochemical analysis	30
2.3.3	Electrochemical reduction of GO: Ni-P films	31
2.4	Instrumentation	31
2.4.1	Scanning Electron Microscope	31
2.4.2	X-ray Photoelectron Spectroscopy	32
2.4.3	X-ray Diffraction	32
2.4.4	Infrared spectroscopy	32
2.4.5	Raman Spectroscopy	33

2.4.6	Electrochemical characterization	33
3	RESULTS AND DISCUSSION	34
3.1	Introduction	34
3.2	Synthesis and characterization	35
3.2.1	CB8-porphyrin frameworks	35
3.2.2	Graphene oxide	40
3.2.3	Electrochemically Reduced Graphene Oxide	44
3.2.4	ERGO nickel CB[8]-porphyrin composites	47
3.3	Electrochemical analysis	52
3.3.1	Nickel CB[8]-porphyrin	53
3.3.2	GO Nickel CB[8]-porphyrin	56
3.3.3	ERGO Nickel CB[8]-porphyrin	62
3.3.4	The optimum sample	66
4	CONCLUSION	73
A	Data	89

List of Figures

1.1	Structure of graphene oxide and the different methods to reduce it	12
1.2	Randell cell's electrical circuits (left) and their equivalent Nyquist plots (right) with and without Warburg element	25
3.1	SEM images of CB[8]-porphyrin assembly at different magnifications using 15.0 kV beam energy	39
3.2	High resolution XPS spectra of C 1s, O 1s and N 1s of CB[8]-porphyrin assembly	39
3.3	Experimental procedure for the sythesis of graphene oxide	40
3.4	SEM images for GO-modified FTO at different magnifications	41
3.5	High resolution XPS spectra of (a) C 1s and (b) O 1s of GO	42
3.6	(a)XRD patterns for graphite flakes and GO-modified FTO (b)XPS elemental survey (c) Raman spectra and (d) FT-IR measurements for GO-modified FTO	43
3.7	SEM images for ERGO-modified FTO at different magnifications	44
3.8	High resolution XPS spectra of the (a) C 1s and (b) O 1s of ERGO	45

3.9	(a)XRD patterns for ERGO-modified FTO (b)XPS elemental survey (c) Raman spectra and (d) FT-IR measurements for ERGO-modified FTO	46
3.10	SEM images for ERGO:Ni-P-modified FTO at different magnifications	48
3.11	High resolution XPS spectra of the (a) C 1s and (b) O 1s (c) N1s and (d) Ni 2p of ERGO:Ni-P	49
3.12	(a)XRD patterns for graphite flakes and ERGO:Ni-P-modified FTO (b)XPS elemental survey (c) Raman spectra and (d) FT-IR measurements for ERGO:Ni-P-modified FTO	50
3.13	SEM images of ERGO: Ni-P (a) before and (b) after 3h CA experiment showing C, O , N and Ni mappings	51
3.14	XPS spectra of (a) C 1s and (b) O 1s (c) N 1s and (d) Ni 2p after 3h CA for ERGO: Ni-P	52
3.15	(a) Polarization curves of Ni ₅ -P, Ni ₁ -P and Ni ₂ -P in 0.1 M KOH at scan rate of 1 mV s ⁻¹ (b) Tafel plot of same composites showing Tafel slope(c) CV curves in double layer region at scan rates of 50, 60, 70, 80, 90 and 100 mV s ⁻¹ of Ni ₂ -P (d)The capacitive currents at 0.81 V as a function of scan rate for Ni ₂ -P ($\Delta j=j_{anodic}-j_{cathodic}$)	55
3.16	(a) Chronoamperometry (CA) for Ni ₂ -P at -0.34 V in 0.1 M KOH(b) Polarization curves for Ni ₂ -P in acidic, neutral and basic mediums at a scan rate of 1 mV/s	56

- 3.17 (a) Polarization curves of $\text{GO}_1\text{-Ni}_{1.5}\text{-P}$, $\text{GO}_1\text{-Ni}_1\text{-P}$, $\text{GO}_1\text{-Ni}_2\text{-P}$, $\text{GO}_{.5}\text{-Ni}_2\text{-P}$ and $\text{GO}_2\text{-Ni}_2\text{-P}$ in 0.1 M KOH at scan rate of 1 mV s^{-1} (b) Tafel plot of same composites showing Tafel slope (c) CV curves in double layer region at scan rates of 50, 60, 70, 80, 90 and 100 mV s^{-1} of $\text{GO}_1\text{-Ni}_2\text{-P}$ (d) The capacitive currents at 0.81 V as a function of scan rate for $\text{GO}_1\text{-Ni}_2\text{-P}$ ($\Delta j = j_{anodic} - j_{cathodic}$) 59
- 3.18 (a) Polarization curves of $\text{GO}_1\text{:Ni}_{1.5}\text{-P}$, $\text{GO}_1\text{:Ni}_1\text{-P}$, $\text{GO}_1\text{:Ni}_2\text{-P}$, $\text{GO}_{.5}\text{:Ni}_2\text{-P}$ and $\text{GO}_2\text{:Ni}_2\text{-P}$ in 0.1 M KOH at scan rate of 1 mV s^{-1} (b) Tafel plot of same composites showing Tafel slope (c) CV curves in double layer region at scan rates of 50, 60, 70, 80, 90 and 100 mV s^{-1} of $\text{GO}_1\text{:Ni}_2\text{-P}$ (d) The capacitive currents at 0.81 V as a function of scan rate for $\text{GO}_1\text{:Ni}_2\text{-P}$ ($\Delta j = j_{anodic} - j_{cathodic}$) 61
- 3.19 (a) Polarization curves of $\text{ERGO}_1\text{-Ni}_{1.5}\text{-P}$, $\text{ERGO}_1\text{-Ni}_1\text{-P}$, $\text{ERGO}_1\text{-Ni}_2\text{-P}$, $\text{ERGO}_{.5}\text{-Ni}_2\text{-P}$ and $\text{ERGO}_2\text{-Ni}_2\text{-P}$ in 0.1 M KOH at scan rate of 1 mV s^{-1} (b) Tafel plot of same composites showing Tafel slope (c) CV curves in double layer region at scan rates of 50, 60, 70, 80, 90 and 100 mV s^{-1} of $\text{ERGO}_1\text{-Ni}_2\text{-P}$ (d) The capacitive currents at 0.81 V as a function of scan rate for $\text{ERGO}_1\text{-Ni}_2\text{-P}$ ($\Delta j = j_{anodic} - j_{cathodic}$) 63
- 3.20 (a) Polarization curves of $\text{ERGO}_1\text{:Ni}_{1.5}\text{-P}$, $\text{ERGO}_1\text{:Ni}_1\text{-P}$, $\text{ERGO}_1\text{:Ni}_2\text{-P}$, $\text{ERGO}_{.5}\text{:Ni}_2\text{-P}$ and $\text{ERGO}_2\text{:Ni}_2\text{-P}$ in 0.1 M KOH at scan rate of 1 mV s^{-1} (b) Tafel plot of same composites showing Tafel slope (c) CV curves in double layer region at scan rates of 50, 60, 70, 80, 90 and 100 mV s^{-1} of $\text{ERGO}_1\text{:Ni}_2\text{-P}$ (d) The capacitive currents at 0.81 V as a function of scan rate for $\text{ERGO}_1\text{:Ni}_2\text{-P}$ ($\Delta j = j_{anodic} - j_{cathodic}$) 65
- 3.21 (a) Polarization curves showing the effect of adding GO and nickel separately (b) Polarization curve showing the effect of number of layers on $\text{ERGO}_1\text{:Ni}_2\text{-P}$ in 0.1 M KOH 67

3.22	(a) Impedance spectra of ERGO ₁ : Ni ₂ -P in 0.1 M KOH solution at different applied overpotentials. The inset shows the equivalent circuit (b) Bode plot of ERGO ₁ : Ni ₂ -P showing phase and impedance (c) The capacitive currents at 0.81 V as a function of scan rate ($\Delta j=j_a-j_c$) and (d) Impedance spectra of ERGO, GO ₁ :Ni ₂ -P and ERGO ₁ : Ni ₂ -P modified FTO electrode in 0.1 M KOH.	68
3.23	Polarization curves for ERGO ₁ :Ni ₂ -P in acidic, neutral and basic mediums	69
3.24	Impedance spectra of ERGO ₁ : Ni ₂ -P-modified FTO in 1 M KOH. The inset shows the equivalent circuit	70
3.25	(a) CV curves in non-faradaic region at scan rates from 50 to 100 mV/s for ERGO ₁ : Ni ₂ -P in 1 M KOH (b) The capacitive currents at 0.81 V as a function of scan rate ($\Delta=j_a-j_c$) (c)Chronoamperometry at -1.2 V vs RHE in 1 M KOH for 12000 seconds (d) Polarization curves of ERGO ₁ : Ni ₂ -P initially and after 12000 seconds chronoamperometry test at -1.2 V vs Ag/AgCl in 1 M KOH.	71
A.1	Chronoamperometry measurements for (a) Ni-P (b) GO-Ni-P (c)GO:Ni-P and (d) ERGO:Ni-P in 0.1 M KOH	89
A.2	EDX analysis showing elemental composition for (a) GO (b) ERGO and (c) ERGO:Ni-P	90
A.3	Cyclic voltammetry scans in 0.1 M PBS for (a) GO and (b) GO:Ni-P	90
A.4	¹ H NMR for TPP-4(OCH ₃)	91
A.5	¹ H NMR for TPP-4OH	91
A.6	ESI-MS for TPP-4OH	92

A.7 ESI-MS for TPP-n($\text{OC}_3\text{H}_6\text{Br}$) 92

List of Tables

3.1	Compositions of all Ni-P inks	53
3.2	Electrochemical parameters for Ni-P samples from potentiometry	54
3.3	Compositions of GO-Ni-P samples (all in one ink)	57
3.4	Electrochemical parameters for GO-Ni-P samples (all in one ink) .	58
3.5	Compositions of all GO:Ni-P samples	60
3.6	Electrochemical parameters for GO:Ni-P composites	60
3.7	Electrochemical parameters for ERGO:Ni-P composites	62
3.8	Electrochemical parameters for ERGO:Ni-P composites	64
3.9	Electrochemical parameter for ERGO1: Ni ₂ -P in 0.1 and 1 M KOH	72

List of abbreviations

b	Tafel slope (mVdec^{-1})
CA	Chronoamperometry
CB	Cucurbit[n]uril
CB[8]	Cucurbit[8]uril
CV	Cyclic voltammetry
ECSA	Electrochemical active surface area
EIS	Electrochemical impedance spectroscopy
ERGO	Electrochemically reduced graphene oxide
ERGO:Ni-P	Layer of nickel porphyrin functionalized on layer of electrochemically reduced graphene oxide
ERGO-Ni-P	Electrochemically reduced graphene oxide nickel porphyrin all in one ink
ES-MS	Electro Spray Mass Spectroscopy
F	Farady's constant (96485 C/mol)
FE	Faradaic efficiency
FT-IR	Fourier Transform Infrared Spectroscopy
GO	Graphene oxide
HER	Hydrogen evolution reaction
j	Current density (mAcm^{-2})
ja	Anodic current density
jc	Cathodic current density
jo	Exchange current density
LSV	Linear sweep voltammetry
N	Amount of hydrogen produced in moles
n	Number of electrons transferred

NA	Avogadro's number (6.023×10^{23} atoms/ mol)
NMR	Nuclear magnetic resonance
OER	Oxygen evolution reaction
Q	Total charge
R	Resistance
R'	Ideal gas constant
R_{ct}	Charge transfer resistance
RHE	Reversible hydrogen electrode
R_s	Solution resistance
S	Surface area of electrode
SEM	Scanning Electron Microscopy
T	Temperature (K)
TOF	Turnover frequency
TPP	Tetraphenyl porphyrin
XPS	X-ray Photoelectron Spectroscopy
XRD	X-ray Diffraction
Z	Impedance
Z'	Real part of Impedance
Z''	Imaginary part of Impedance
η	Overpotential
$\eta@ 10 \text{ mAcm}^{-2}$	Overpotential at 10 mAcm^{-2}

Chapter 1

Introduction

1.1 Hydrogen as an alternative fuel

The consistent increase in energy requirements has introduced the excessive utilization of non-renewable energy sources around the world. According to the World Coal Institute, with the current consumption rate of fuels, it is predicted that coal will completely deplete in 130 years, natural gas in 60 years and oil in 42 years.[1] In addition to their limited resources, these fuels introduce major concerns due to their serious environmental issues. Moreover, Fuels such as biodiesel or gasoline are not readily available everywhere and require a complicated engine technology for effective production. Therefore, the search for an alternative clean energy fuel has been intensively under study. Renewable fuels, produced from solar or wind energies, are capable of providing greater energy than any conventional fossil fuel.[2] It is predicted that by the years 2025 and 2050, 36% and 69% of the energy supplied will come from renewable sources. In specific, 11% of energy supplied will come from hydrogen in 2025 and 34% in the year 2050.[3]

In the past decade, hydrogen has attracted great attention as a promising fuel for the future. It is the simplest, most readily abundant element on earth. It easily combines with other chemicals and produces only water as a combustion

product, allowing it to be a potential candidate for an eco-friendly fuel. Furthermore, hydrogen releases three times more energy (122 kJ/g) than fuels based on hydrocarbon. [4]

1.1.1 Hydrogen production methods

Hydrogen can be produced using renewable (solar, wind, hydroelectric and geothermal energy) or nonrenewable resources (natural gas, coal, biomass and nuclear). Currently, most hydrogen is produced from fossil fuels. This is achieved by several process technologies namely: steam reforming of natural gas, thermal cracking of natural gas, partial oxidation of hydrocarbons (heavier than naphtha) and coal gasification. Another production technique is by pyrolysis or gasification of biomass which produces a mixture of gases (H_2 , CH_4 , CO_2 , CO and N_2). Finally, hydrogen could be produced from water via electrolysis, photolysis, thermochemical process, direct thermal decomposition (thermolysis) and biological production. [5]

Currently, more than 95% of the global hydrogen is produced by non-renewable fossil fuels, mostly by steam reforming of natural gas. The rest, less than 5%, is produced by water electrolysis and biomass.[6] The production of hydrogen from steam reforming of natural gas and hydrocarbons results in a high yield with low operational and production costs.[7] The process involves two steps: first the hydrocarbon fuel reacts with steam producing syngas (H_2/CO gas mixture). In the second step, the cooled syngas gas is fed into the carbon monoxide catalytic converter where it is converted into carbon dioxide and hydrogen by the help of steam. The foremost disadvantage of this process is the enormous release of carbon dioxide, 7.05 kg $CO_2/kg H_2$. [8] The efficiency of hydrogen production by this process is usually limited by two main parameters. One is the characteristics of catalysts (e.g. effectiveness factor) due to the heat and mass transfer limitations of reformers. Typically, nickel catalysts are used so the kinetics is scarcely a limitation. [9] The other crucial factor is the ratio of hydrogen to carbon atoms in the reactant fuel. The higher this ratio the less carbon dioxide emission. [10]

Another method for producing hydrogen gas is using Biomass as the starting material. Biomass is any living matter that is produced by organic residues and wastes which is used as a form of energy. The main sources of biomass include: wood, agriculture crops, animal waste and industrial wastes from food processing and aquatic plants. [11] Biomass will play a major role in the future in the production of chemicals and fuels since it is a renewable and sustainable energy source. [12] It is anticipated that 25% of the world's primary energy supply will be derived from biomass by the year 2050. [13] Secondary energy carriers such as heat, electricity and fuels can be generated from raw biomass in various conversion methods that could be biological, chemical or thermal.[14] Hydrogen gas in specific, can be produced from biomass by biological means using anaerobic digestion, fermentation and metabolic processing or thermochemical processes such as gasification, high pressure aqueous and pyrolysis.[15] Biomass gasification involves the partial oxidation of materials into a mixture of hydrogen, methane, hydrocarbons, carbon monoxide and carbon dioxide.[16] This process results in a product with low thermal efficiency, due to the vaporization of biomass, and high cost since a large amount of biomass is used initially.[17]

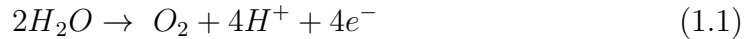
Pyrolysis is the process of heating a biomass in the absence of air at temperature of 650-800K and pressure between 0.1 and 0.5 MPa. Pyrolysis can be classified into slow and fast pyrolysis depending on the speed of heating. Hydrogen production is normally performed under fast pyrolysis where the biomass feedstock is quickly heated to form vapor which further forms a condensed liquid.[18] This process results in products in the three states, gaseous products (H_2 , CH_4 , CO and CO_2), liquid products (tar, oils...) and solid state (char and carbon).[19] Besides the gaseous products, hydrogen can be produced by processing the produced oils. Pyrolysis oil separates into two parts based on solubility where hydrogen can be produced from the water-soluble fraction. The four crucial parameters that influence the efficiency of this process are: Temperature, heating rate, residence time and type of catalyst. For large production rate of hydrogen, long residence time, high temperature and heating rate are desired.[20]

The most recent, green and environmentally-friendly hydrogen production

methods include the use of water. This is achieved by either electrolysis, photo-electrolysis or thermolysis. Electrolysis is the simplest water splitting method in which an electrochemical cell is composed of two electrodes and an electrolyzer. When electricity is supplied to the system, water essentially splits into hydrogen and oxygen at cathode and anode respectively. In acidic medium, water oxidizes at the anode forming oxygen, four protons and electrons. The electrons then flow through the external circuit towards the cathode. Meanwhile, protons from anode move across the electrolyte to the cathode. The protons combine with the electrons that came from external circuit to produce hydrogen gas.[21]

The half-reactions that occur at anode and cathode in acidic electrolyte can be written as:

Anode reaction:



Cathode reaction:



The most common electrolysis system involves using an alkaline electrolyzer, mainly aqueous potassium hydroxide (KOH) but other techniques such proton exchange membrane (PEM) electrolysis and solid oxide electrolysis cells (SOEC) units are developing. Although alkaline systems are frequently used, they have a low efficiency hence use a huge amount of energy. Therefore, the use of solid oxides for electrolysis is much more efficient than alkaline however, it imposes challenges due to corrosion and seals.[21]

Photoelectrolysis, as the name suggests involves the same working principles as electrolysis with the extra addition of a light source. The sun provides us with 4.3×10^{20} Joules/hr which is enough to fulfil our global energy need for a year. This implies that if only 0.8% of the land on earth is covered with solar cells with an efficiency of 10%, the total power generated is 30TW which is more than enough to satisfy the current annual energy needs (17.7 TW). In a photo-electrochemical cell (PEC), typically a light source, similar to sunlight, is used

to decompose water into hydrogen and oxygen on the surface of a semiconductor. When the energy of the photon incident is greater than the semiconductor's bandgap, the photon gets absorbed onto the material releasing an electron hence forming a hole. When a p-type semiconductor (excess holes) or a n-type (excess electrons) is immersed into an aqueous electrolyte, electrons and holes are forced to travel opposite directions. Holes move to the anode where they decompose water to form hydrogen ions and gaseous oxygen, while electrons flow through the outer electrical circuit to the cathode. The hydrogen ions then diffuse into the electrolyte and gain electrons to form hydrogen gas at the cathode. The photoelectrode and semiconductor materials are the most crucial variables that determine the activity of this system.[22]

In order to achieve a PEC cell with good efficiency, the electrode material must have the following characteristics: the semiconductor material must generate a sufficient voltage (>1.23 eV) for water splitting. This means that the irradiated light should attain energy greater than the bandgap of the material. It is convenient to have a material with a small band gap (< 2.2 eV) for sufficient photocatalytic activity. The electrode material must also be resistant to corrosion in electrolyte and light exposure. Typically, metal oxides are known to be stable semiconductor catalysts, but their band gaps are usually too large for absorption of light (around 3 eV). The material should have a reasonable price of production and operation with a high quantum yield.[21]

Finally, in thermochemical water splitting, or otherwise known as thermolysis, only heat is used to decompose water into hydrogen and oxygen. Water decomposes at a temperature of 2500°C but it is difficult to sustain materials at such a high temperature. Recent researches are aimed on reducing this temperature and using higher pressures. [21]

1.1.2 Applications of Hydrogen

Hydrogen gas is a foreseen alternative fuel for the near future owing to its outstanding properties that permit its usage in numerous fields. Along with its

application in fuel cells to produce electricity, hydrogen gas is used as transportation fuel in vehicles and even as a rocket fuel in NASA since the 1950s.[23] It has also been used in industry in fertilizer production, pharmaceuticals, glass purification and in petroleum refineries.

Renewable electricity is produced mainly from solar, hydropower, geothermal and wind energies that are challenging to store for later use. Currently, industrial scale electricity is stored in pumped hydropower stations. These storage systems or adiabatic air systems have high efficiencies since the potential energy of various levels or compression can instantly be converted to electricity. But as the demands for renewable energy will increase in future, larger electricity storage systems will be required. Hydrogen has the potential to serve as electricity storage as it stores in the range of 100 GWh in underground salt caverns.[2] This high energy density allows it to store a huge amount of energy, however due to the additional conversions by electrolysis and fuel cell it has a lower efficiency in comparison to pumped hydropower stations. Considering the three main criteria: energy density, efficiency and price, hydrogen makes the best fit for future renewable energy storage that is ready for basic power supply.

As the carbon dioxide emission continues to increase drastically with excessive use of vehicles, more environmentally friendly transportation fuels are constantly under investigation. Recently, fuel cell-based vehicles are being constructed. These vehicles consist of a fuel cell, hydrogen tank, electric motor and a Lithium-Ion battery. It is essential to have a battery in order to recover braking energy by using electric energy as a generator. Also, it is useful in low temperatures as it can preheat the car using waste heat of fuel cell. Typically, the electricity from motor is used to fill the battery and the heat from fuel cell is used for warming up the car. Furthermore, vehicles operated by hydrogen gas are found to be twice as efficient as conventional fuels and power trains used today. Therefore, in order to achieve longer operating ranges, higher payloads and fast refueling abilities vehicles will very likely be based on hydrogen fuel cell in the foreseeable future.[2]

1.2 Electrochemical water splitting

1.2.1 Thermodynamics

The general water splitting reaction at standard conditions (298 K, 1 bar) is described by:



At reversible conditions, when pressure and temperature are constant:

$$\Delta G = \Delta H - T\Delta S \quad (1.4)$$

Where ΔH is the enthalpy change, that is the total amount of energy required for the water splitting reaction to occur, it is measured in J/mol. The enthalpy of water splitting reaction is positive which indicates an endothermic reaction. ΔS is the entropy change which is positive for non-spontaneous reactions such as the reaction above. Here, ΔG is the Gibbs free energy that is the electrical energy demand for water splitting. At room temperature and pressure, ΔG is equal to 237.13 kJ for water splitting ($\Delta H^\circ=285.83$ kJ/mol and $\Delta S^\circ=163.09$ J/mol.K). The positive value of Gibbs indicate that water splitting is a non-spontaneous reaction hence requires a large external input to proceed. The standard cell potential E° is related to Gibbs free energy by the following relation.

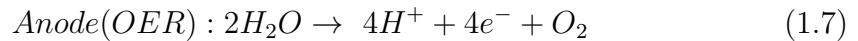
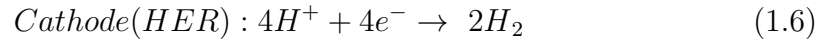
$$\Delta G^\circ = -nFE^\circ \quad (1.5)$$

where n is the number of electrons transferred ($n= 2$ in this case) and F is the Faraday constant (96,485 C/mol). Using these parameters, the value of standard potential of the water electrolysis is calculated to be -1.229 V at 25°C . [21]

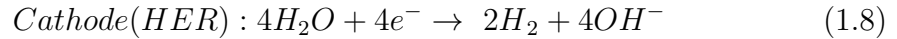
The minimum voltage at room temperature required for water splitting is 1.23V. However, additional energy is required to make the reactions proceed

at appreciable rates (that is, activation energy). The faster the rate of water splitting (measured as charge flowing per unit area of electrode per unit time, or ‘current density’), the greater the activation energy that must be supplied. This additional energy manifests as a requirement for potential bias above the 1.23V minimum. The term ‘overpotential’ (often given the symbol η) describes how much additional voltage must be applied to obtain a given current density. The role of electrocatalysts is then to reduce this overpotential as far as possible. The electrochemical water splitting undergoes different mechanisms depending on the electrolyte of use. In acidic mediums for instance, water splits into oxygen gas and protons that further gets reduced at the cathode forming hydrogen gas. In basic mediums however, the absence of protons in electrolyte forces the charge transfer by hydroxide ions instead, as shown in the equations below. Hydrogen gas is again evolved at the cathode and oxygen at the anode.[24]

In H_2SO_4



In KOH



Under acidic conditions (Equation 1.6, Equation 1.7), the best electrocatalysts are precious metals (platinum at the cathode and IrO_2 or RuO_2 at the anode). Under basic conditions, the HER and OER proceed according to Equation 1.8 and Equation 1.9, in which case first row transition metals (and their alloys) and

oxides make excellent HER and OER catalysts, respectively. The best-known heterogeneous catalysts for the HER are based on platinum. Because platinum is rather expensive and rare, there has been considerable interest in hydrogen evolution electrocatalysts featuring more plentiful elements. Under very alkaline conditions (30% KOH in water), first row transition metals, such as nickel, have long been known to be effective HER catalysts.

1.2.2 Factors affecting efficiency of the electrochemical cell

The most crucial factor that affects water splitting, is the choice of electrocatalyst. The ideal electrode material for electrochemical water splitting should have a suitable price range, is chemically stable, inert and resistant to corrosion.[25] Platinum, gold, and silver are well-known electrode materials but their high price limits their excessive use at the commercial level. Usually metal oxides and phosphides such as nickel and cobalt are used as electrode materials in alkaline and acidic electrolytic baths.

Another factor that influences the efficiency of an electrochemical cell is temperature. The extent of water splitting is reduced as temperature increases because energy demand of reaction decreases.[26] Heat can also reduce the equilibrium voltage resulting in larger bubbles with lower rising velocities and a decline in efficiency due to larger void fraction.[27] An increase in temperature may introduce other issues concerning stability of electrode material, glass ware or may lead to disturbance in the system.

Furthermore, the electrolyte quality and resistance affect the performance of water splitting. The presence of mobile ions in the water is crucial for water splitting to occur therefore, the electrolyte must be either acidic or basic since pure water is strongly resistive to electricity.[28] However, high acidic or basic concentrations of electrolyte are not desired due to their corrosive nature, for example, 25%–30% aqueous KOH is widely used in electrolyzers. Likewise, very low

concentrations are not used as they increase electrical resistance hence decrease electrocatalytic performance and efficiency of electrochemical cell.[29] Basic mediums are more common electrolytes as most electrocatalysts are not very stable in acidic environments. It is also important to free the electrolyte from dissolved gases, therefore, the mediums are usually degassed with argon or nitrogen prior to electrochemical measurements.

Finally, the orientations of the electrodes should also be considered. Size, alignment, and space between the electrodes are factors that may affect the efficiency of electrocatalysts. It is crucial to use electrodes with similar heights to prevent introducing larger volume of void fractions that lead to additional power dissipation to the cell.[27] Furthermore, vertically placing the electrodes result in easier release of bubbles hence increasing efficiency. Likewise, reducing the distance between the electrodes minimizes the electrical resistance in electrochemical cells. However, too close electrodes will increase void fractions hence reduce efficiency of the process.

1.2.3 Electrocatalysts for HER

Platinum-based catalysts are the most prominent leading catalysts for hydrogen evolution reaction with a nearly zero onset potential and a rapid current increase with voltage.[30] However, their scarcity, high cost in large scale utilization encourages the continuous search for cheaper and more durable alternatives with high performance. Other less expensive noble metal-based catalysts (Pd, Ru) have been investigated for this purpose yet they have poorer performance.[31] The strong need for an effective HER catalyst has devoted the research on non-precious metals such as Mo, Co, Ni and Fe. Nickel-based materials are potentially considered for HER owing to their low cost, high electrical and thermal conductivity, good ductility, resistance to corrosion and durable strength.[32] Nickel-based electrocatalysts could be very effective alternative to Pt since they both have very similar chemical properties, are in the same group in periodic table and

are much cheaper and more readily abundant than Pt.[33] Besides metal hydroxides and oxides, many scholars are modifying nickel based catalysts by implanting other non-metals such as C, N, P and S to control their structures. Gong et al. reported a highly effective HER catalyst based on NiO/Ni–CNT with current density -81 mA cm^{-2} at η @-10 mV. Both Ni and NiO enhanced the HER activity in distinct ways. The study predicts that Ni metal boosts the adsorption of hydrogen onto catalyst surface while NiO was the favored region for absorption of OH^- produced by nickel sites. The positive charge of Ni^{2+} ions along with the larger number of d orbitals present in the oxide in comparison to metal Ni is the root of the strong electrostatic attraction between NiO and hydroxide ions.[34]

Although metal-free HER catalysts are not that common, organic-based catalysts are being taken into consideration owing to their exclusive synthetic flexibility, excellent chemical stability, strong tolerance to acid and alkaline medium and low processing costs.[35]

1.2.3.1 Graphene oxide

Graphene is a 2-D honey comb structure comprising of a single layer of tightly bonded sp^2 carbon atoms.[36] Over the past few years, graphene has drawn significant attention because of its unique mechanical, thermal, optical and electrical properties. In particular, graphene has a high thermal conductivity ($5000 \text{ W m}^{-1}\text{K}^{-1}$), attains good charge carrier mobility at room temperature ($200,000 \text{ cm}^2\text{V}^{-1}\text{s}^{-1}$) and has an exceptionally large surface area ($2600 \text{ m}^2\text{g}^{-1}$).[36, 37]

The oxidation of graphite powder by strong oxidizing agents result in the formation of layered graphite oxide that is rich in hydroxyl and epoxide functional groups on its basal planes and carbonyl, carboxyl groups on its edges.[38] Owing to these oxygen-containing functional groups, graphite oxide is readily dispersible in water, forming stable suspensions of extremely hydrophilic graphene oxide sheets.[39, 40] Exfoliation of graphite oxide has been proven to be a reliable method to produce stable suspensions of quasi-2D carbon sheets, making this a strategic starting point for large-scale synthesis of graphene sheets.[41]

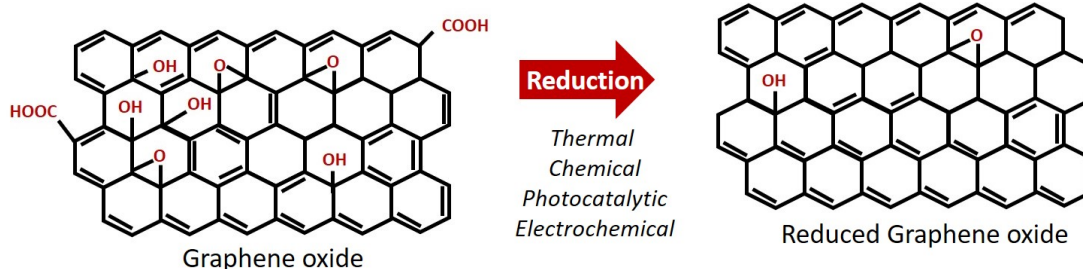


Figure 1.1: Structure of graphene oxide and the different methods to reduce it

As shown in Figure 1.1, there are many techniques for synthesis of graphene and the reduction of graphene oxide.[42] To date various methods have been established to produce graphene including micromechanical exfoliation, chemical and electrochemical reduction of graphite oxide and bottom-up organic synthesis.[43, 44, 45] Due to its low cost and significant scalability, reduction of graphene oxide (GO) has shown to be an efficient and reliable process for synthesizing graphene nanosheets. [46]

GO is not a readily abundant compound; its chemical composition and the mechanism of its oxidation remain unclear due to its non-stoichiometric character, robust hygroscopic properties as it is rich in oxygen groups.[47] The removal of these oxygen entities results in the production of reduced graphene oxide which resembles pristine graphene.[48] Therefore, it is vital to choose a suitable reducing method for this reaction. The reduction process can intensely enhance the electrical conductivity of graphene oxide. The excessive charge carrier concentration and mobility in the material improves the reflection to incident light hence, RGO results in metallic shine film while GO remains in brown color.[49] Furthermore, the chemical reduction of GO (with hydrazine) produces a black precipitation from the yellow–brown GO suspension. This is most likely due to the increase in the hydrophobicity of the material caused by a decline in polar functional groups on the surface of the sheets.[50]

There are numerous methods to reduce graphene oxide; namely: *thermal*, *chemical*, *photocatalytic* and *electrochemical*. Graphene oxide can be reduced exclusively by rapid heating (>2000 °C/min) in a process named *thermal*

annealing reduction. In the primary stages of reduction, the excessive heat is used to exfoliate graphite oxide to achieve graphene.[51, 52] This abrupt rise in temperature promotes the decomposition of oxygen containing groups on the carbon plane that results in a massive pressure between the stacked layers. The final product is named graphene rather than reduced graphene oxide as the heating not only exfoliates graphite oxide but also intensively reduces the functionalized oxygen-containing groups on graphene sheets by decomposing at elevated temperature.

Chemical reduction involves the usage of strong chemical reducing agents under room temperature or moderate heating. This method doesn't require special equipment and environment as that of *thermal annealing* treatment making it a cheaper and an easily obtainable technique for the mass production of graphene compared with thermal reduction. Hydrazine and many of its derivatives have been considered as the best-known chemical agents for graphene oxide reduction.[53] However, due to its toxic nature hydrazine exhibits some concerns with environment and safety, which have encouraged researchers look for alternative "green reduction agents". Ascorbic acid (Vitamin C) is a recently studied green reducing reagent for graphene oxide, which is considered to be an ideal alternative for hydrazine. Fernandez-Merino et al. discovered that graphene oxide reduced by Ascorbic acid could attain a carbon to oxygen ratio of about 12.5 and a conductivity of 77 S/cm, which are comparable to the values obtained by using hydrazine.[54] Therefore, the use of Ascorbic acid is favored over hydrazine on account of its non-toxicity and high chemical stability.

Furthermore, reduced graphene oxide can be produced by *photocatalyst reduction* with the support of a photocatalyst such as TiO_2 . Williams et al. conveyed the reduction of colloidal GO by TiO_2 particles under ultraviolet (UV) irradiation. A change in color from light brown to dark brown/black was also observed after UV irradiation for 2h in ethanol.[55]

Another promising method for producing reduced graphene oxide is *electrochemical reduction*. Electrochemically reduced graphene oxide is found to

be more conductive while possessing a lower oxygen to carbon ratio than the conventional chemically reduced one.[56] The electrochemical reduction of graphene oxide is achieved by applying a negative potential that reduces the oxygen functional groups on its surface.[57, 58] Graphene or reduced graphene oxide is used as an effective electron acceptor that can be used to improve photoinduced charge transfer and prevent the reverse reaction by separating the evolution sites of hydrogen and oxygen resulting in an enhanced hydrogen production efficiency.[59] Electrochemical reduction of graphene oxide sheets or films can be conducted in a conventional electrochemical cell at room temperature using an aqueous buffer solution as an electrolyte. This reduction technique requires no special chemical agent, and is primarily triggered by the electron exchange between graphene oxide film and electrodes. After depositing a thin film of graphene oxide onto the working electrode, an inert electrode is placed opposite the film, the reduction process begins as the cell is charging. The reduction can be achieved by cyclic voltammetry scanning in the negative potential window and is confirmed by observing a single cathodic current peak in the first cycle. The position of this peak varies from one study to another, due to the choice of buffer medium and the method of synthesis of graphene oxide.[60] Nevertheless, it is clear that in most cyclic voltammetry studies GO-coated electrode, the cathodic current peak in the first cycle of scanning decreases considerably in the following scanning cycle and vanishes almost completely after several scanning cycles indicating that the electrochemical reduction of GO to ERGO is an irreversible process.[61, 62]

1.2.3.2 Porphyrin and its derivatives

Organic materials are recently being considered for various applications due to their unique properties. The molecular structures and functions of these materials can be modified by molecular design and tailoring. These π -conjugated molecules can be used for the fabrication of functionalized nanomaterials and nanodevices owing to their delocalized π -electron system.[63, 64] Porphyrins in particular have attracted major attentions because of their exceptional ability to harvest light, chemical stability, good semiconducting behavior and effective supramolecular

assembly that can be easily modified.[65, 66]

Porphyrins are a group of conjugated macrocycles consisting of 4 pyrrole rings aromatically interconnected through a methylene bridge (=CH-), containing 11 conjugated double bonds.[67] In many cases porphyrin is coordinated with a transition metal in its core which is often used to modify its properties. Such compounds are called metalloporphyrins. This metal center induces the formation of a metal-hydrogen and behaves as a redox center in multielectron reduction processes.[68] Unlike metalloporphyrins, the two basic imine nitrogen atoms in metal-free porphyrins' core results in the formation of deprotonated porphyrin species.[69] Furthermore, the four nitrogen atoms in the porphyrin core are adequate for combining protons close together to lower the activation energy of hydrogen production by modifying the transition state of H-H bond formation.[70] Owing to the four available nitrogen atoms in the inner core of porphyrin, it can be conjugated to various functional groups. Tetrakis(4-hydroxyphenyl)porphyrin (THPP) for instance, consists of four phenol unit, 5,10,15,20-tetraphenyl-21H,23H-porphyrin (TPP) is made up of 3 benzene rings and one phenol unit while 5-(4-hydroxyphenyl)-10,15,20-tri-(p-phenyl)porphyrin (TPPOH) composes of four benzene groups on its extremes.

With the aid of a catalyst, electron donor and an electron carrier, porphyrins have been extensively implemented in electrocatalytic systems for application in water splitting reactions. Owing to their exclusive properties, porphyrins may act artificial photosensitizers behaving analogously to the naturally found photosensitizers chlorophyll and ferredoxin.[71] Qian et al, reported a conjugated polymer based catalytic system for application in hydrogen production. The photosensitizer used was zinc meso-tetra(1-methylpyridinium-4-yl) porphyrin chloride $[\text{ZnTMPyP}^{4+}] \text{Cl}_4$, electron carrier and donor were viologens and ethylenediaminetetraacetic acid (EDTA) respectively and the catalyst utilized was hydrogenase.[72] Another similar report by Lazarides et al. studied the same $[\text{ZnTMPyP}^{4+}] \text{Cl}_4$ as a photosensitizer but used cobaloxime complex as a catalyst. This system resulted in good hydrogen efficiency with TON of 280 and over a 20 h stability.[73] Moreover, another study involved the use of conjugated monohydroxylated cucurbit(7)uril(CB7) to tetraphenyl porphyrin (TPP-4CB7)

as a photosensitizer for HER. This novel assembly together with TiO_2 and platinum (TPP-CB- TiO_2 @Pt) resulted in excellent activity with low potentials (onset = -10 mV and $\eta@10\text{mAcm}^{-2} = -470$ mV) and produced a large amount of hydrogen ($24.5 \text{ mmol h}^{-1} \text{ g}^{-1}$).[74] Other studies involved the application of different photosensitizers that photoinitiated Co, Fe, and Rh porphyrins catalysts for hydrogen evolution reaction. In one study for example, hydrogen evolution was achieved in 1 M phosphate buffer solution using $[\text{Ru}(\text{bpy})_3]^{2+}$ as the photosensitizer, ascorbic acid as the electron donor and cobalt (II) porphyrin as the catalyst. The resulting system was found to be very effective with fast electron transfer ($2.3 \times 10^9 \text{ M}^{-1}\text{s}^{-1}$) and high TON (725).[75]

Cucurbit[n]urils are robust macrocyclic structures synthesized by a condensation reaction between glycoluril units and formaldehyde with the help of an acid catalyst.[76] After its initial discovery, Mock et.al successfully crystallized it from the reaction and the resulting product composed of 6 glycoluril units tightly bound by 12 methylene bridges. This macrocycle was given the name cucurbit[6]uril (CB6), owing to its six glycoluril units.[77] The unique properties of this macrocycle permit easy non-covalent bindings due to its ability to form complexes with cations via interactions with carbonyl units and internalize alkyl chains within its hydrophobic cavity. The Cucurbituril family was further studied by Kim [78] and Day [79, 80] which resulted in the discovery of new CB[n] homologues containing 5,7,8 and 10 glycoluril units that were named CB[5], CB[7], CB[8] and CB[10] respectively. The variation in the number of glycoluril units lead to difference in cavity size, guest binding affinity, water solubility and size selectivity in the Cucurbituril family.[77] The application of cucurbiturils (mainly CB[5]-CB[8]) have been widely studied in various fields including applications in drug delivery,[81] catalysis [82] fluorescence spectroscopy,[83] and nanotechnology[84].

1.2.3.3 Porphyrin - GO composites

Porphyrin has been commonly investigated in the field of catalysis due to its unique structure, high thermal stability and outstanding electrical properties.[85]

The properties of porphyrin can be improved and modified by introducing distinct functional groups or metal ions. Recently, porphyrin has been linked to carbon based functional groups such as carbon nanotubes and graphene either by covalent or non-covalent interactions.[86] Similarly, the presence of epoxide, hydroxyl and carboxyl functional groups in graphene oxide permit covalent or non-covalent functionalization with various organic and inorganic materials. In many cases, the composite requires a metal linker to promote electron transfer between the two entities. Non-noble metal ions act as interfacial electron-transfer mediators and endorse charge separation by quickly transferring electrons which is the root to enhancing the electrocatalytic activity of GO/porphyrin composites. The composite can be thought of as a donor-acceptor combination where electrons from GO are accepted by porphyrin rings that are delocalized in the π conjugated structures.

Over the past few decades, a series of porphyrin- graphene oxide complexes have been synthesized for the use in various applications. For instance, reduced graphene oxide-porphyrin complex was used for electrochemical biosensor to regulate dopamine and serotonin[87], nanorod composites for solar light harvesting[88], photothermal therapy of brain cancer[89], amperometric biosensing [90] and photocatalytic degradation over TiO_2 nanotubes.[91] Furthermore, porphyrin functionalized on reduced graphene oxide sheets has been used for oxygen evolution reactions (OER) and hydrogen evolution reactions (HER). Ma, et al. reported the synthesis of Co porphyrin and electrochemically reduced graphene oxide hybrid film (CoTMPyP/ERGO) for HER in alkaline medium.[92] The onset potential was found to be -220 mV and the Tafel slope was 99 dec^{-1} in 0.1 M KOH. Another study on Co porphyrin/electrochemically reduced graphene oxide hybrid film was prepared using alternating layer by- layer (LBL) assembly.[93] The overpotential at 1 mAcm^{-2} was found to be -474 mV and the Tafel slope was 116 dec^{-1} . One more study by Luo, et al. involved the synthesis of graphene oxide hybrid functionalized on tetrakis-(4-hydroxyphenyl) porphyrin (THPP) and 1-pyrenesulfonic acid (PSA) for photocatalytic hydrogen evolution.[94] The average rate of hydrogen evolution for GO/THPP/PSA hybrid was found to be 44.3 $\mu\text{mol h}^{-1} \text{g}^{-1}$.

1.3 Activity parameters for HER

Linear sweep voltammetry, cyclic voltammetry, chronoamperometry and electrical impedance spectroscopy are all techniques in potentiostat used to evaluate electrochemical activity of a catalyst. Since water splitting is a non-spontaneous process, it requires an addition potential to drive the reaction, this is known as overpotential (η).

The Nernst equation is used to convert all the potentials measured by potentiostat (vs reference electrode) to the reversible hydrogen electrode (RHE). In the case when Ag/AgCl is used as a reference electrode, the potentials obtained are converted as shown below.

$$E_{RHE} = E_{Ag|AgCl|KCl(sat.)} + 0.059pH + E_{Ag|AgCl|KCl(sat.)}^{\circ} \quad (1.10)$$

Where E_{RHE} is potential estimated vs. RHE, $E_{Ag|AgCl|KCl(sat.)}$ is the measured potential vs. Ag|AgCl|KCl(sat.) electrode and $E_{Ag|AgCl|KCl(sat.)}^{\circ}$ is the standard electrochemical potential of the Ag|AgCl|KCl(sat.) electrode i.e. 0.1976 V at room temperature.

1.3.1 Overpotentials

The reversible potentials with respect to standard hydrogen electrode (vs. RHE) for hydrogen evolution reaction (HER) and oxygen evolution reaction (OER) are 0 V and 1.23 V respectively. Therefore, the overpotentials of HER and OER without iR compensations can be calculated as: $\eta_{OER} = E_{RHE} - 1.23$ V and $\eta_{HER} = E_{RHE} - 0$ V. The current density of 10 mAcm^{-2} has been recognized as a benchmark for the analysis and characterization of different electrocatalytic materials in all media for both HER and OER. The onset potential is the potential at which a drastic increase in reduction current is observed.[96]

1.3.2 Tafel plots

A plot of overpotential(η) vs log current density is known as a Tafel plot, which is a useful tool for evaluating kinetic parameters. The relationship between overpotential and current density at the electrode surface is given by Butler–Volmer equation.[97]

$$j = j_0 \left[e^{\frac{\alpha_A n F}{RT} \eta} - e^{\frac{-\alpha_C n F}{RT} \eta} \right] \quad (1.11)$$

Where j is the current density, j_0 is exchange current density respectively, α_A and α_C are the charge transfer coefficients for the anodic and cathodic reactions, respectively. F is the Faraday constant (96485 C/mol), n is the number of electrons transferred, R is the ideal gas constant, and T is the absolute temperature in K.[97] At high overpotentials, Butler–Volmer equation give rise to Tafel equations of the cathodic and anodic polarizations.

$$\text{Cathodic : } \ln(j) = \ln(j_0) + \frac{-\alpha_C n F}{RT} \eta \quad (1.12)$$

$$\text{Anodic : } \ln(j) = \ln(j_0) + \frac{\alpha_A n F}{RT} \eta \quad (1.13)$$

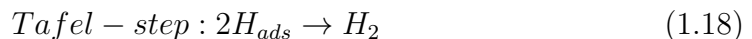
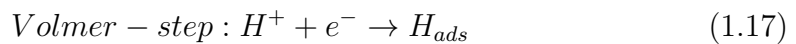
The two polarization equations have the form $y=b+mx$, and will result in a linear plot (Tafel plot) when $\log(j)$ is plotted versus η . Considering the conversion from \ln to \log ($\ln x = 2.303 \log x$) the slopes of cathodic and anodic reactions in Tafel plot become:

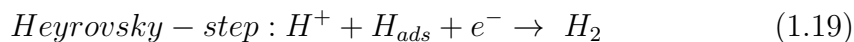
$$\text{Cathodic} = \frac{2.3RT}{-\alpha_C n F} \quad (1.14)$$

$$\text{Anodic} : \frac{2.3RT}{\alpha_A n F} \quad (1.15)$$

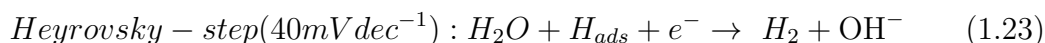
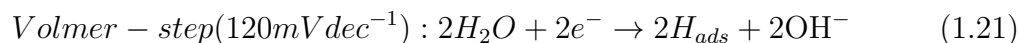
The exchange current density j_0 is found by extrapolating the linear Tafel plot to the log of current density at the reversible potential. In other words, j_0 for HER is the inverse log of current density at 0 V and similarly, for OER j_0 is the inverse log of current density at 1.23 V overpotential. The Tafel slope and exchange current density are used to predict the kinetics of reaction at electrocatalytic interface. As shown in the Tafel slope equations, the slope is inversely proportional to charge transfer coefficient (α), which indicates the smaller the Tafel slope, the faster the charge transfer across the electrolyte/ catalyst interface. In HER, the Tafel slope is typically associated with the HER mechanism at a the electrocatalytic interface. The value of Tafel slope gives an indication on the mechanism of hydrogen evolution reaction at the catalyst interface. There are two main mechanisms for HER, namely: Volmer–Heyrovsky and Volmer–Tafel mechanisms. Usually, the first step, Volmer, involves the adsorption of hydrogen ions from electrolyte onto the electrode surface. The second step includes either the recombination of two adsorbed hydrogen atoms (Tafel step) or the direct bonding of an adsorbed hydrogen atom and a hydrated proton that includes an electron transfer (Heyrovsky step).[98] The catalysts for HER follow quite different paths in acid and alkaline mediums. The readily available protons in acidic electrolytes promotes a facile electron transfer unlike the basic medium where excess energy is required to break the water molecules. The overall reactions in acidic (Equation 1.16) and basic (Equation 1.20) along with the intermediate reactions are given below. [99]

In acidic electrolyte





In basic electrolyte



A low Tafel slope (30 – 40 mV dec⁻¹) designates a facile Tafel pathway, rich in electroactive sites at the catalyst interface. Given the large number of available active sites, the initial step in Tafel pathway is the adsorption of hydrogen atom onto active site and the generation of hydrogen in rate determining step. For a material to undergo Tafel pathway, the distance between two active surface sites should be less than the van der Waals radius of the two adsorbed H atoms to increase the chance of desorption. Such materials include precious metals such as platinum and phosphides of 3d transition metals.[97] Other non-precious metal-based electrocatalysts for HER (chalcogens of Fe, Co, Ni, and Mo) undergo a slightly different mechanism that includes an additional adsorption and electrochemical release of another previously produced proton on active site.[100] This mechanism is called Volmer–Heyrovsky that results in a Tafel slope between 50 and 120 mV dec⁻¹. This pathway is usually taken when there is a small accessibility to active sites. These mechanisms are valid for acidic medium, alkaline mediums require additional intermediate number of steps that involve water or

hydroxide ions. This is due to the scarcity of free protons in solution that require extra potential resulting in higher Tafel slopes.

1.3.3 Turnover Frequency (TOF)

Turn over frequency is another kinetic parameter that specifies how quickly a catalyst may catalyze an anticipated electrochemical reaction. The general equation for calculation of TOF is shown below.[97]

$$TOF = j \times \frac{N_A}{n} \times F \times \Gamma \quad (1.24)$$

where j stands for the current density (Acm^{-2}), N_A is Avogadro's number ($6.023 \times 10^{23} \text{ mol}^{-1}$), n is the number of electrons transferred to evolve one molecule of product ($n=2$ for HER, $n=4$ for OER), F is the Faraday constant (96485 C) and Γ is the surface concentration of active sites or number of atoms involved in the catalyst material. TOF is rarely used as a distinguishing parameter to evaluate electrocatalysts for water splitting due to the difficulty in calculating the surface concentration (Γ). Usually, the mass of the loaded catalyst is used to determine the surface-active concentration of metal sites available assuming a 100% participation of all atoms in the catalyst together with atoms in the inner core of the catalyst. With this assumption in mind, TOF can be calculated as follows[101]

$$TOF = \frac{jS}{2Fm} \quad (1.25)$$

The number 2 in the equation implies two electrons per H_2 . S is the surface area of electrode and m is the number of moles of the metal ions calculated from loading density.

1.3.4 Faradaic Efficiency (FE)

The faradaic efficiency of electrocatalyst indicates the selectivity of catalyst for HER processes. Faradaic efficiency is calculated by comparing experimentally measured evolved hydrogen gas to the theoretically calculated amount obtained from Faraday's law of electrolysis. The experimental amount of gas evolved is calculated by collecting it and converting the volume obtained to moles. This is compared to the value from Faradaic law using passed charge. A 100% faradaic efficiency indicates that the electrocatalyst is highly specific to hydrogen evolution with no other side reactions. Therefore, faradaic efficiency is an essential parameter of HER electrocatalyst as it reflects the selectivity of the catalyst. It is independent of the size, shape or morphology of the catalyst. The faradaic efficiency can be theoretically estimated as follows:

$$\text{Faradaic efficiency} = \frac{nNF}{Q} \times 100 \quad (1.26)$$

Where n is the number of electrons transferred in the faradaic process, Q is total charge passed through the whole reaction (calculated from potentiometry), N is the amount of H_2 generated in moles (calculated from chronoamperometry).

1.3.5 Electrochemical Active Surface area (ECSA)

ECSA represents the available active sites for an electrochemical reaction. It is a poor activity parameter which cannot be used to compare or evaluate electrocatalysts of different studies. This is due to the fact that the meaning of electrochemical surface area differs from one electrochemical process to another and one material to another. However, it can still be used to assess the activities of similar catalysts in the same study. ECSA is commonly estimated using the double layer capacitance of the interface between electrode and electrolyte. From cyclic voltammetry studies at different scan rates in the non-faradaic region, a plot of the difference in anodic and cathodic current densities ($\Delta j = j_a - j_c$)

against scan rate yields a linear line with double layer capacitance as the slope. Since ECSA is calculated from the non-faradaic ion adsorption and desorption processes, it would result in a poor prediction of gas evolution reactions which are faradaic processes.

1.3.6 Electrochemical impedance spectroscopy (EIS)

Electrochemical impedance spectroscopy (EIS) analysis has become a significant technique in studying the charge transfer process involved in a three-electrode system. Typically, in EIS, the steady state response of the cell to distortions by a small alternating signal is monitored by plotting electrode impedance against frequency. The behavior of an electrochemical cell can be mimicked with an electrical circuit. If we consider a resistance R and a capacitance, C in series, when a voltage (E) is applied, the sum of individual components is equal to this total voltage. This eventually leads to the following relation for real and imaginary impedance:

$$Z(\omega) = Z_{real} + iZ_{imaginary} \quad (1.27)$$

The variation of impedance with frequency is present in a Bode plot ($\log Z$ vs ϕ) or a Nyquist plot ($Z_{imaginary}$ vs Z_{real}). For simplicity, $Z_{imaginary}$ and Z_{real} are noted with Z' and Z'' respectively. A Randel's circuit represents an electrochemical cell consisting of a solution resistance R_s in series with a combination of double layer capacitance (C_{dl}) and an impedance of faradic reaction represented by charge transfer resistance element (R_{ct}) positioned in parallel. Often a diffusion element needs to be added to the total faradaic impedance of the system, this component is called a Warburg element and is presented by Z_W as shown in second row of Figure 2.[98]

In kinetically controlled reactions, the charge transfer resistance gives an indication of the speed of reaction. The smaller this value, the easier the charge is transferred and the faster the reaction occurs.

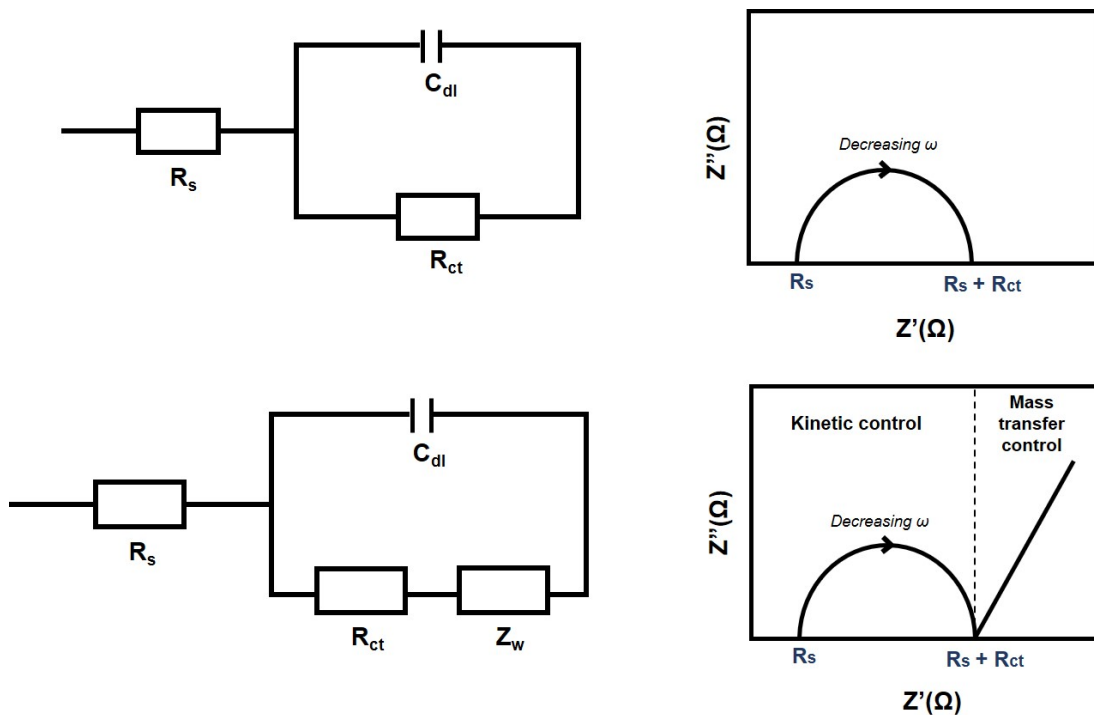


Figure 1.2: Randell cell's electrical circuits (left) and their equivalent Nyquist plots (right) with and without Warburg element

1.3.7 Amount of hydrogen produced

The number of moles of hydrogen gas produced in an hour per mass of catalyst (mol/h.g) is calculated using Faraday's law:

$$\text{Number of moles of } H_2(\text{mol/hr.g}) = \frac{j t}{n F m} \quad (1.28)$$

Where j is the current density from chronoamperometry at 3600 seconds in amperes.

1.4 Aim of study

This study focuses on the application of a nickel CB[8]-porphyrin framework functionalized on electrochemically reduced graphene oxide in electrochemical hydrogen production. The work examines the effect of implementing graphene oxide and reduced graphene oxide along with the choice of electrolyte, weight ratios of nickel acetate, ERGO/GO on the electrocatalytic activity of the composite. Initially, nickel porphyrin composites are investigated in acidic, basic and neutral electrolytes while varying nickel concentration. Graphene oxide synthesis is then discussed along with the procedure taken to reduce it. Accordingly, GO nickel porphyrin samples were synthesized by either mechanically adding it to Ni porphyrin (all in one ink) or by drop-casting a layer of Ni-P on top of GO layer. Later, these samples were electrochemically reduced. Here the impact of varying GO and nickel salt were separately examined. All samples were evaluated according to the electrochemical parameters aforementioned. The optimum sample was further characterized and tested in other mediums. The prepared films were characterized by X-ray photoelectron spectroscopy (XPS), scanning electron microscopy (SEM), Energy dispersed X-ray (EDX), Raman spectroscopy, Fourier Transform Infrared Radiation (FT-IR) and X-ray diffractometer (XRD).

To our knowledge, this is the first study on CB-based porphyrin electroactive supramolecular assembly functionalized on ERGO for the application in electrocatalytic hydrogen production. In this work, nickel ions are used as metal linkers between graphene oxide and porphyrin assembly. Since graphene oxide is negatively charge due to the ionization of carboxylic acid and phenolic hydroxyl groups on their edge sand surface,[95] it develops electrostatic attraction forces to positively charged nickel porphyrin assembly as well as π - π stacking, which provide intimate contact between them. The composite can be thought of as a donor-acceptor combination where electrons from GO are accepted by porphyrin rings that are delocalized in the π conjugated structures.

Chapter 2

EXPERIMENTAL AND INSTRUMENTATION

2.1 Materials

All reagents and solvents (purchased from Aldrich, Merck) used throughout this study were of analytical grade and used as received with no further purification unless otherwise stated. Milli-Q water (18.2 MQcm at 25 °C) was used when required. ^1H NMR spectra were attained at 400 MHz, using Bruker Avance III 400 MHz NMR spectrometer. Mass spectra were recorded on Agilent 6210 LC/MS TOF mass spectrometer. Column chromatography was done using silica gel which is purchased from Sigma-Aldrich high-purity grade with a 60 Å pore size and between 70 to 230 mesh or using Sephadex G-15 medium. Reactions were examined by thin layer chromatography (TLC) using silica-coated or cellulose-coated TLC plates. Nickel source used for making the composites was Nickel acetate tetrahydrate salt ($\text{Ni}(\text{CH}_3\text{CO}_2)_2 \cdot 4 \text{H}_2\text{O}$). All solvents used in electrochemical measurements were saturated with argon.

2.2 Synthesis

2.2.1 Synthesis of CB8-porphyrin assembly

This work utilizes the conjugation of four perhydroxy cucurbit [8] uril units to 5,10,15,20-tetrakis(4-(3-bromopropoxy) phenyl) porphyrin, as the core electro-catalyst for HER. This structure is denoted with the letter P throughout this thesis for simplicity.

2.2.1.1 Synthesis of hydroxy Cucurbit[8]uril

12.50 g of glycoluril was added to 5.54 g of paraformaldehyde in a round bottom flask and 22.5 ml of concentrated hydrochloric acid was added while stirring at room temperature. The reaction mixture was then heated in an oil bath at 95 °C and stirred overnight then left aside for five days allowing crystals to grow. The solid phase composes of CB6 and CB7 while the crystalline part consists of CB6 and CB8. With further purifications, CB8 was obtained.

Cucurit[8]uril (1g) was hydroxylated using 2.92 g $K_2S_2O_8$ and 1.89 g K_2SO_4 with deionized water. This mixture was refluxed at 85 °C for 12 h under nitrogen atmosphere, this was then cooled to room temperature and precipitate was removed while filtrate was concentrated. The resulting white solid was dissolved in DMSO then filtered. The filtrate was finally dropwise added to acetone and the precipitate of $CB8(OH)_n$ was collected and washed again with acetone.

2.2.1.2 Synthesis of TPP-4(OCH₃)

The porphyrin core was synthesized by first dissolving 1.5 g of 4-methoxy benzaldehyde and 764 of μ l pyrrole in 1.5 L $CHCl_3$ under continuous stirring then adding 450 μ L of the Lewis acid catalyst, $Et_2O \cdot BF_3$. After an hour of stirring, 614 μ l triethylamine and 2.04 g Tetrachloro-1,4-benzoquinone (TCBQ) were added

and left to stir overnight at room temperature then heated under reflux at 60 °C for an hour. The solvent was then evaporated using vacuum dryer under pressure. The resulting solid was further washed several times with chloroform while passing through silica gel. The filtrate was evaporated then suspended and washed several times with methanol to result in TPP-4(OC₃H₆Br) powder after drying.

2.2.1.3 Synthesis of TPP-4(OH)

BBr₃ was added to 250 mg of TPP-4(OCH₃) in 30 ml dry DCM while stirring for an hour at 0 °C then over-weekend at room temperature. The reaction mixture was again cooled to 0 °C then quenched with 10 ml water and sodium bicarbonate solutions to remove unreacted materials and undesired products resulting in TPP-4OH.

2.2.1.4 Synthesis of TPP-4(OC₃H₆Br)

The porphyrin precursor for the desired final conjugated polymer was achieved by bromination of TPP-4OH . Typically, 200 mg of TPP-4OH was stirred in 5 mL DMF and NaH under nitrogen atmosphere for half an hour then 0.418 mL 1,3-bromopropane and stirred for 72 hours. The final TPP-4(OC₃H₆Br) product was first washed with ice water then extracted by chloroform. The progress of the reaction was checked with ESI-MS and NMR analysis.

2.2.1.5 Synthesis of CB[8]-TPP-4(OC₃H₆Br)

The supramolecular assembly was synthesized by adding 300 mg of CB[8](OH)_n to 5 ml of DMSO and NaH under nitrogen atmosphere. Under stirring, 3ml of TPP-4(OC₃H₆Br) was poured after 30 min to the solution in DMSO then left to stir for 72 hour. The product was added dropwise into 15 ml water, centrifuged and washed with water then finally oven-dried to obtain a black solid.

2.2.2 Synthesis of graphene oxide

Graphite oxide was prepared by improved Hummers method (Tour's method). Typically, 3g of available graphite flakes was added to a 9:1 mixture of concentrated $\text{H}_2\text{SO}_4/\text{H}_3\text{PO}_4$ (360:40 mL) under magnetic stirring. Then, 18.0 g of potassium permanganate (KMnO_4) was slowly dispensed in small portions to the reaction mixture resulting in a slightly exothermic reaction ($\sim 40^\circ\text{C}$). The reaction was further heated to 50°C and left to stir for 12 hours. After stirring, the mixture was left to cool to room temperature and was poured onto 400 ml of ice and 3 ml of H_2O_2 (30%). The resulting product is a yellowish-brown slurry of graphite oxide and many impurities that was excessively purified and dried to give graphite oxide powder.

2.3 Experimental

2.3.1 Experimental setup

A conventional three electrode cell was used with Ag/AgCl (3.5 M KCl) as reference electrode, catalyst-modified FTO as the working electrode, and Pt wire as counter electrode. All of the electrochemical experiments were performed using CHI-670 potentiostat at room temperature. The FTO surface was first cleaned with detergent, then with deionized water and isopropanol by ultrasonication for 15 minutes with each. It was then activated by drying in vacuum oven at 450°C for 2 hours. The reaction system was purged with Argon for 30 min to remove the dissolved gases in electrolyte prior to taking measurements.

2.3.2 Sample preparation for electrochemical analysis

The samples studied in this work can be divided into three main sections: Nickel CB[8]-porphyrin, GO nickel CB[8]-porphyrin and ERGO nickel CB[8]-porphyrin.

The composites were prepared by mechanically mixing nickel acetate and porphyrin assembly in certain weight ratios while adding DH_2O , ethanol and Nafion (5%) then magnetically stirring overnight. GO Nickel CB[8]-porphyrin composites were achieved either by mechanically adding graphene oxide powder to nickel CB[8]-porphyrin ink (GO-Ni-P) or by dropcasting a layer of GO first on FTO followed a layer of nickel porphyrin (GO:Ni-P).

2.3.3 Electrochemical reduction of GO: Ni-P films

Once the thin films with desired concentration were prepared, the corresponding GO-Ni-P and GO: Ni-P composites were electrochemically reduced by cyclic voltammetry in argon-saturated 0.1 M phosphate-buffered solution (PBS, pH 7.4) to enhance the conductivity in the HER process. The system was swept for 50 cycles between 0.0 and -1.5V (vs Ag/AgCl) at 50 mV s^{-1} to achieve ERGO-Ni-P and ERGO: Ni-P thin film.

2.4 Instrumentation

CB[8]-porphyrin framework, graphene oxide and electrochemically reduced graphene oxide were all characterized using the available instrumentation techniques before using in electrochemical analysis. The optimum sample was then chosen based on best electrochemical activity and further characterized in depth using SEM, XPS, XRD, FT-IR and Raman. For these characterization measurements, samples were assembled onto FTO substrates.

2.4.1 Scanning Electron Microscope

To examine the surface topology and composition of a sample material, FEI-Quanta 200 FEG ESEM was used. EDX analysis system were also enabled to

carry out compositional analysis on specimens. Prior to analysis, all sample-modified FTO were coated with 3 μ m of Au/Pd to enhance their conductivity.

2.4.2 X-ray Photoelectron Spectroscopy

The surface chemistry and identity of chemical bond in the composites were analyzed using Thermo Scientific K-Alpha X-Ray Photoelectron Spectrometer system with a AlK α monochromator source operating at 400 mm spot size and $h\nu = 14.866$ eV accompanied by a flood gun for charge neutralization, 200 eV for survey scan and 30 eV for individual scans. All binding energies were referenced to C1s spectrum of the carbon support at 284.6 eV.

2.4.3 X-ray Diffraction

XPert Pro Multipurpose X-Ray Diffractometer (MPD) was used to study the crystalline structure of composites and their atomic spacing. XRD measurements were carried out using CuK α X-Ray Radiation ($\lambda = 1.5418$ Å) with 2θ diffraction angle range of 4-50 $^\circ$, step size of 0.05 and time per step of 500s.

2.4.4 Infrared spectroscopy

To further characterize the functional groups and bonds present in the specimens, Attenuated Total Reflectance – Fourier Transform Infrared Spectroscopy (ATR FT-IR) recorded by Bruker Alpha Platinum-ATR spectrometer model. The spectra were recorded in transmission mode using 32 scans in wavenumber range of 400- 4000 cm^{-1}

2.4.5 Raman Spectroscopy

The vibrational behavior of samples was determined by Raman spectroscopy. The Raman shifts were collected using the WITec Gmph alpha300 confocal Raman microscopes from 500 to 3000 cm^{-1} , at an excitation wavelength of 532 nm.

2.4.6 Electrochemical characterization

All electrochemical analysis including activity and stability measurements of electrocatalyst were performed in a three-electrode system using CHI-670 potentiostat. Potentiometry, cyclic voltammetry, impedance spectroscopy and chronoamperometry techniques were all obtained using CHI-670 potentiostat for evaluating electrocatalyst efficiency. Prior to any electrochemical analysis, dissolved oxygen was removed from the quartz cell by purging it with Argon gas for 30 minutes. Linear sweep voltammetry measurements were conducted at a scan rate of 1 mVs^{-1} from 0 to 2 V vs Ag/AgCl in Argon saturated electrolyte for HER. Electrochemical impedance spectroscopy (EIS) measurements were obtained at -0.4 V vs Ag/AgCl at an ac signal amplitude of 5 mV from 0.1 to 1×10^5 Hz. Cyclic voltammetry scans and chronoamperometry measurements were taken at the later specified parameters depending on the samples.

Chapter 3

RESULTS AND DISCUSSION

3.1 Introduction

This chapter comprises of three main sections. In the section 3.2, the synthesis and characterization of cucurbit [8] uril-porphyrin conjugate, graphene oxide and reduced graphene oxide are discussed. This section also represents SEM, XPS, XRD, IR and Raman images of the optimum sample which was chosen based on best electrocatalytic activity. Section 3.3 highlights the electrochemical measurements performed on all samples in this study. Initially, the electrochemical performance of nickel CB[8]-porphyrin composites is examined (section 3.3.1). The studies further investigate the influence of adding graphene oxide to this composite either mechanically (section 3.3.2.1) or as a separate layer (section 3.3.2.2). Finally the effect of graphene oxide reduction was explored by electrochemically reducing composites in section 3.3.2.

3.2 Synthesis and characterization

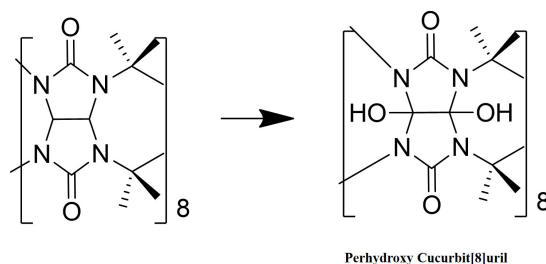
3.2.1 CB8-porphyrin frameworks

The main aim of this study is to construct a novel supramolecular assembly for application in electrocatalytic hydrogen evolution. Multifunctional frameworks allow the modification of structure and functions of materials giving them the advantage to be used in various applications. Porphyrins are highly appealing building blocks for application in hydrogen evolution due to their stable hydrophobic cores that permit the conjugation to diverse functionalities forming supramolecular assemblies.[83] For this study, Tetraphenylporphyrin (TPP) in specific is selected as the core because of its high conductivity and ability to produce singlet oxygen.[102] Cucurbit[n]urils have exceptional properties that enable them to bind to many different guests while attaining high affinity and selectivity.[103] CB8 in particular is a unique host molecule that is able to simultaneously bind two guest molecules with high association (binding) constants ($K_a \geq 10^{11} \text{M}^{-2}$).[104] The conjugation of CB8 units to TPP could result in high efficiency for hydrogen evolution since the bulky nature of CB8 reduces their interaction with porphyrin core allowing more surface area for reaction. The distinctive structure of cucurbituril acts as an anchor in order to encapsulate donor/acceptor molecules for energy transfer processes.[102]

Although CB8- TPP-(OC₃H₆Br)_n on its own is a decent catalyst for hydrogen evolution reaction, its electrochemical activity can be enhanced by integrating reduced graphene oxide into the framework. The noncovalent functionalization of GO provides an ideal support for electroactive systems due to its strength, large surface area and excellent electrical conductivity.[105] Using nickel ions as metal linkers between graphene oxide and CB[8]-porphyrin can also induce electron transfer between the two entities. The electrostatic and $\pi - \pi$ stacking interactions between the positively charged nickel CB[8]-porphyrin assembly and the negatively charged ERGO sheets introduces a synergistic effect that improves electrocatalytic hydrogen evolution.

3.2.1.1 Synthesis of CB8-porphyrin framework

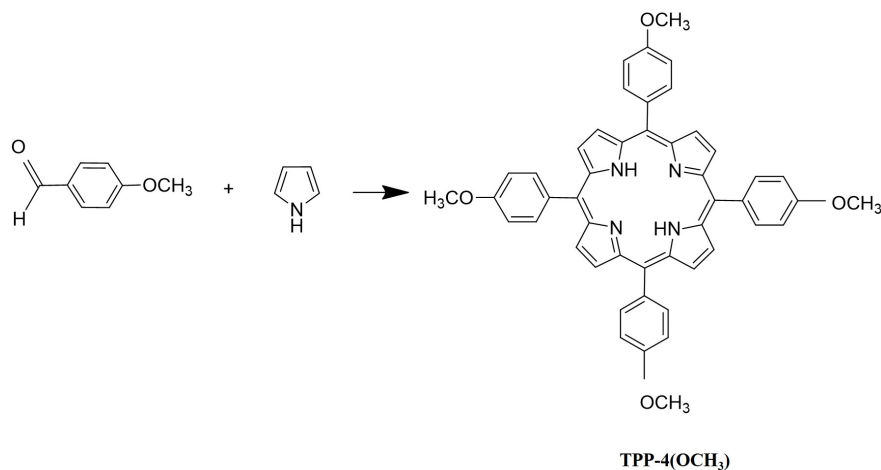
As described in chapter 2, this work focuses on the conjugation of four perhydroxy cucurbit [8] uril units to 5,10,15,20-tetrakis(4-(3-bromopropoxy) phenyl) porphyrin. The schemes for the reactions involved in the synthesis of the CB[8]-porphyrin framework are given in this section.



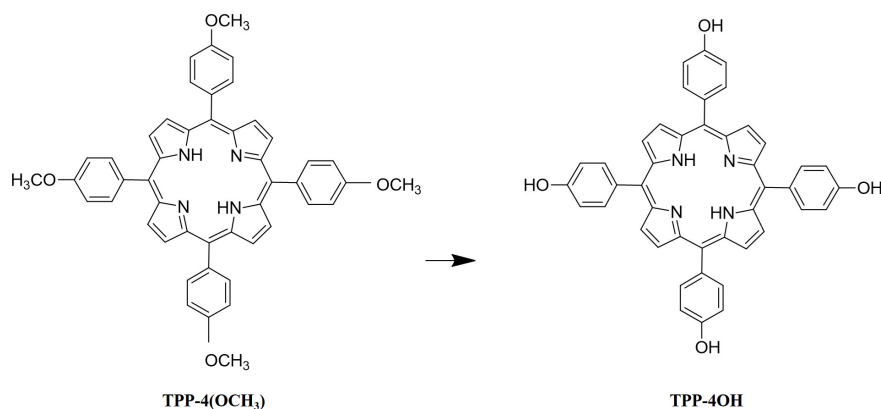
Scheme 3.1: Hydroxylation of Cucurbit[8]uril

The hydroxylation of cucurbit[8]uril can be observed in scheme 3.1. The ^1H NMR (400 MHz, CDCl_3) of the resulting purple powder displayed δ (ppm): 8.87 (s, 8H, pyrrolic H), 8.13 (d, $J = 8.0$ Hz, 8H, ArH), 7.29 (d, $J = 8.0$ Hz, 8H, ArH), 4.128 (s, 3H, OCH_3), -2.726 (s, 2H, NH) (Figure A.4).

The synthesis of TPP-4($\text{OC}_3\text{H}_6\text{Br}$) using methoxy benzaldehyde and pyrrole is described by the following schematic.

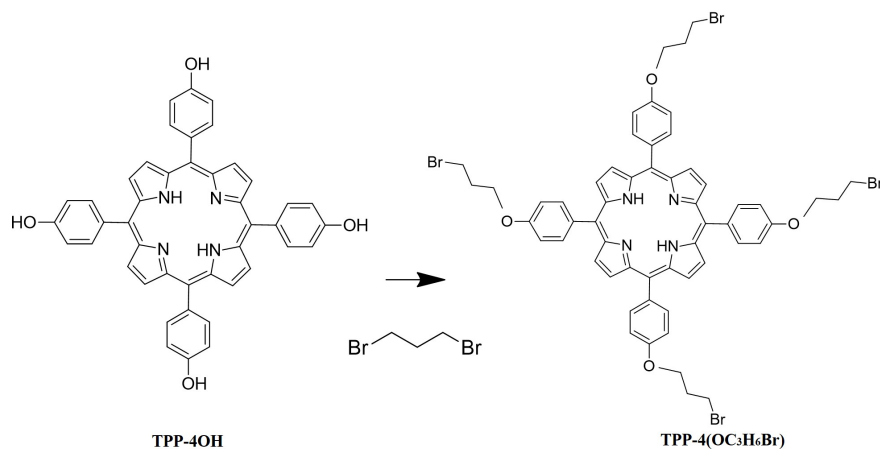


Scheme 3.2: Synthesis of TPP-4(OCH_3) using methoxy benzaldehyde & pyrrole



Scheme 3.3: Synthesis of TPP-4(OH) from TPP-4(OCH₃)

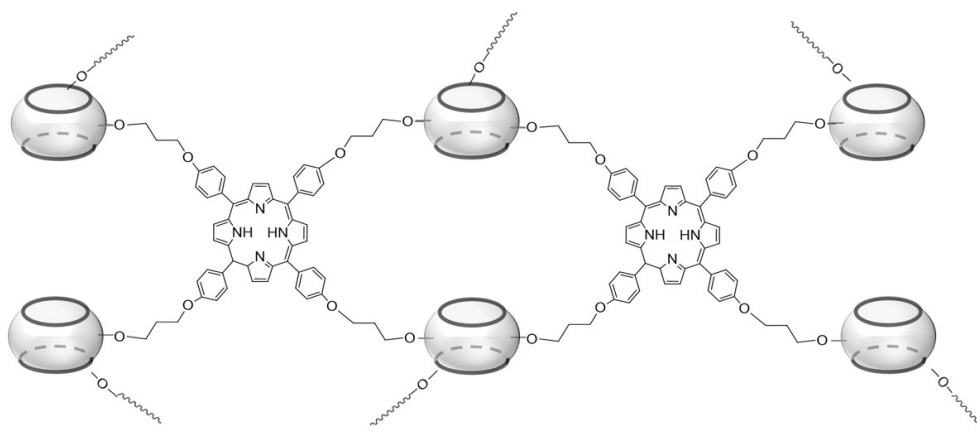
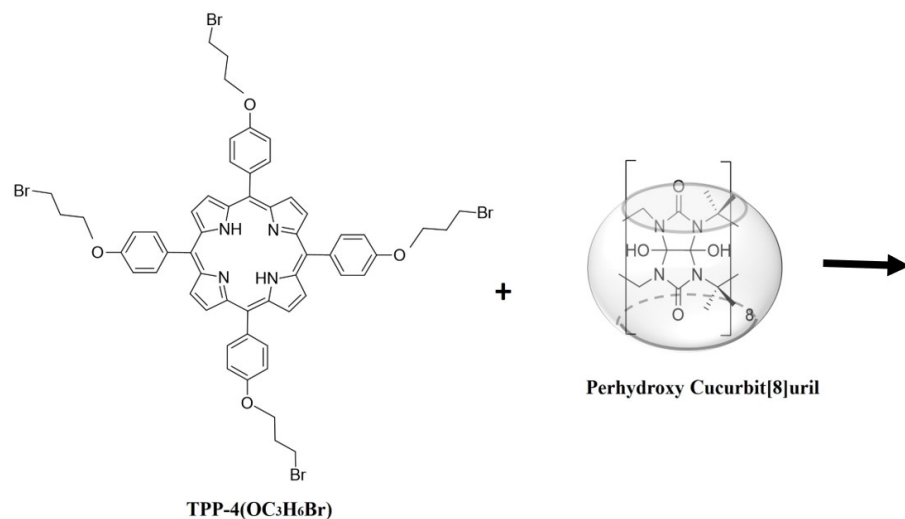
The resulting green solid of TPP-4(OH) (yield ~ 92 %) was characterized by NMR. ¹H NMR (400 MHz, DMSO-d₆) δ (ppm): 9.96 (br, s, 4H, OH), 8.85 (s, 8H, pyrrolic H), 8.00 (d, J = 8.0 Hz, 8H, ArH), 7.21 (d, J = 8.0 Hz, 8H, ArH), -2.88 (s, 2H, NH). ¹³C NMR (100 MHz, CDCl₃) ¹³ (ppm): 160.4, 157.5, 145.4, 144.0, 140.4, 135.7, 131.9, 131.1, 127.7, 124.2, 121.6, 120.7, 116.1, 114.0 (Figure A.5). The ES-MS (m/z) calculated for C₄₄H₃₁N₄ was found to be 679.2. (Figure A.6)



Scheme 3.4: Synthesis of TPP-4(OC₃H₆Br) from TPP-4(OH)

The final, desired porphyrin form for this study (TPP-4(OC₃H₆Br)) was analyzed by ES-MS where m/z was found to be 1083.6 (Figure A.7)

The synthesis of CB[8]-porphyrin framework using TPP-(OC₃H₆Br)_n and perhydroxy Cucurbit[8]uril precursors is shown in scheme 3.5. The pumpkin shaped



Scheme 3.5: Synthesis of CB[8]-porphyrin framework using TPP-(OC₃H₆Br)_n and perhydroxy Cucurbit[8]uril precursors

like structure corresponds to Cucurbi[8]uril units that is joined at the entites of porphyrin assembly. The resulting framework is used as the core structure for fabricating an effective catalytic system for hydrogen evolution.

3.2.1.2 Characterization of CB8-porphyrin framework

The SEM images of the CB8-porphyrin framework displayed a highly porous structure with numerous void ranging in the size of 250 to 500 nm.

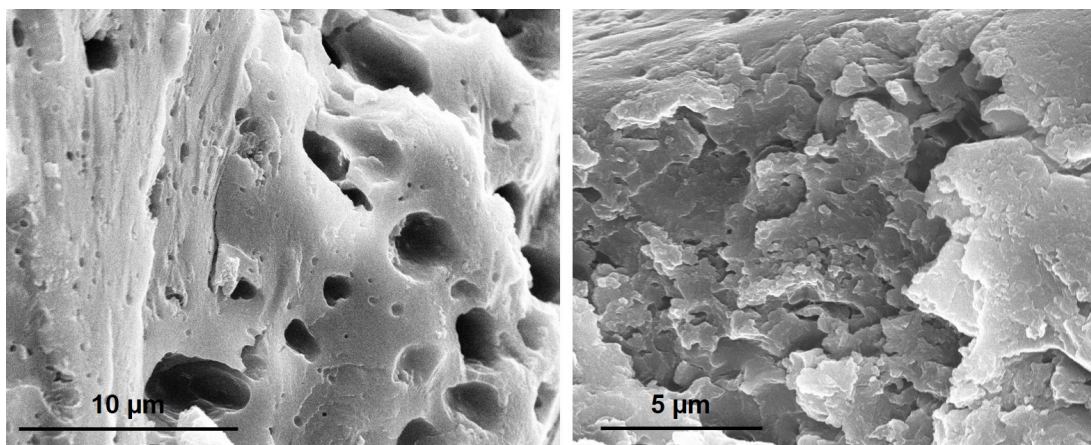


Figure 3.1: SEM images of CB[8]-porphyrin assembly at different magnifications using 15.0 kV beam energy

The XPS spectra of C 1s (Figure 3.2) in CB[8]-porphyrin framework displayed numerous peaks that are equivalent to N-C=O (288.8 eV), C=O (288.0 eV), C=N (287.0 eV), C-O (286.8 eV), N-C=O (288.8 eV), C-C (284.8 eV) and C=C (284.2 eV). O 1s spectra displayed two peaks at 533.0 (C-O) and 531.6 eV (C=O). The last spectra in Figure 3.2 belongs to N 1s spectra with three main peaks, N-(C=O)- at 400.8 eV, N(C₃) at 400 eV, C-NH-C (399.5 eV) and C-N=C (398.2 eV) from porphyrin core.

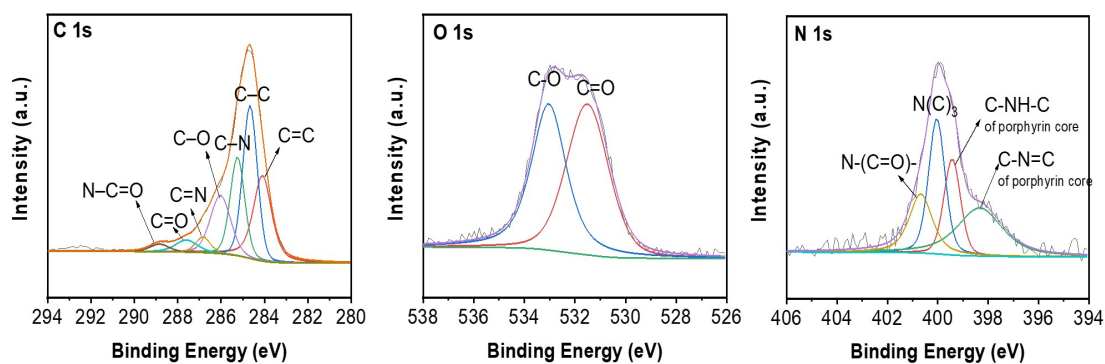


Figure 3.2: High resolution XPS spectra of C 1s, O 1s and N 1s of CB[8]-porphyrin assembly

3.2.2 Graphene oxide

3.2.2.1 Synthesis of graphene oxide

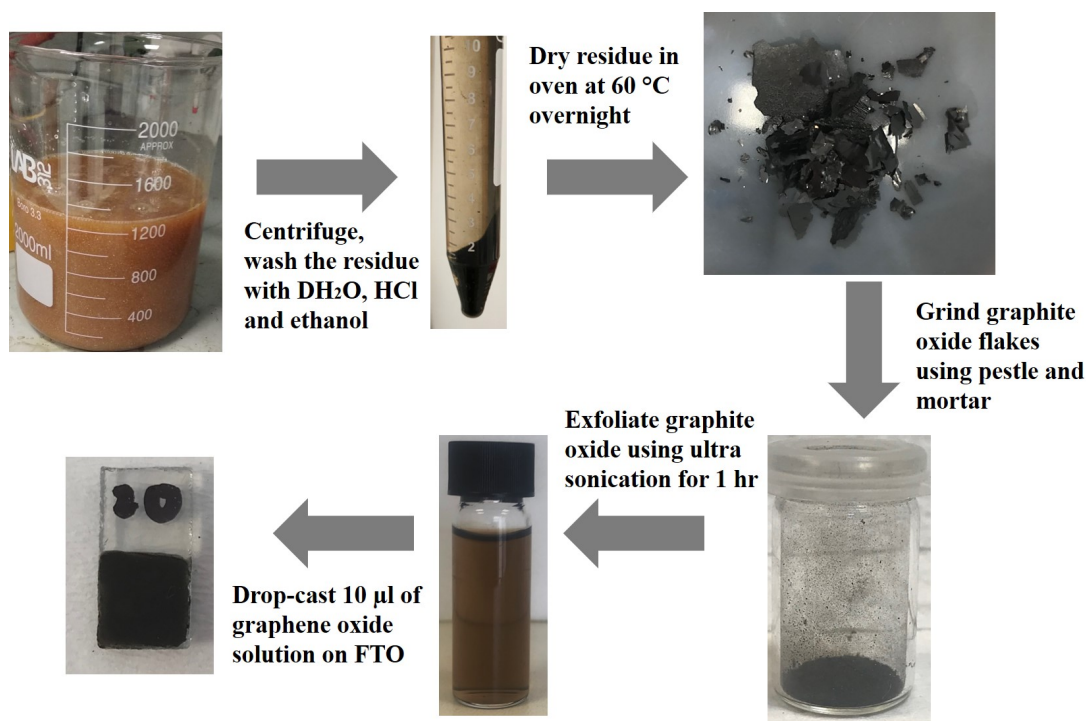


Figure 3.3: Experimental procedure for the sythesis of graphene oxide

Graphene oxide was synthesized by Tour's method as mentioned in chapter 2. The resulting yellowish-brown product from oxidation of graphite flakes was centrifuged at 6000 rpm for 4 h and the supernatant was decanted away. The residue was then washed consecutively with 200 mL of water, 200 mL of 30% HCl, and 200 mL of ethanol. The final solid was dried overnight at 60 °C resulting in graphite oxide flakes. The flakes were finely ground by pestle and mortar to obtain a fine dark-brown powder. The resulting solid was further washed with water when excessive electrostatic interactions with the surroundings was observed. A certain amount of graphite oxide powder was suspended in water while applying ultrasonication for an hour producing a stable graphene oxide solution. A small volume of this dispersion along with Nafion (for adhesion), were then easily drop-casted onto a clean FTO forming a smooth, uniform film. Figure 3.3 displays the step by step experimental procedure to achieve the final graphene oxide film on

FTO.

3.2.2.2 Characterization of graphene oxide

Morphological characterizations of GO- modified FTO was obtained at different beam voltages and spot sizes depending on the image quality (Figure 3.4). GO-modified FTO was coated with 3 μm of Au/Pd to enhance its conductivity. SEM images of GO displayed randomly wrinkled sheets that are firmly connected with one another forming a crumpled solid.

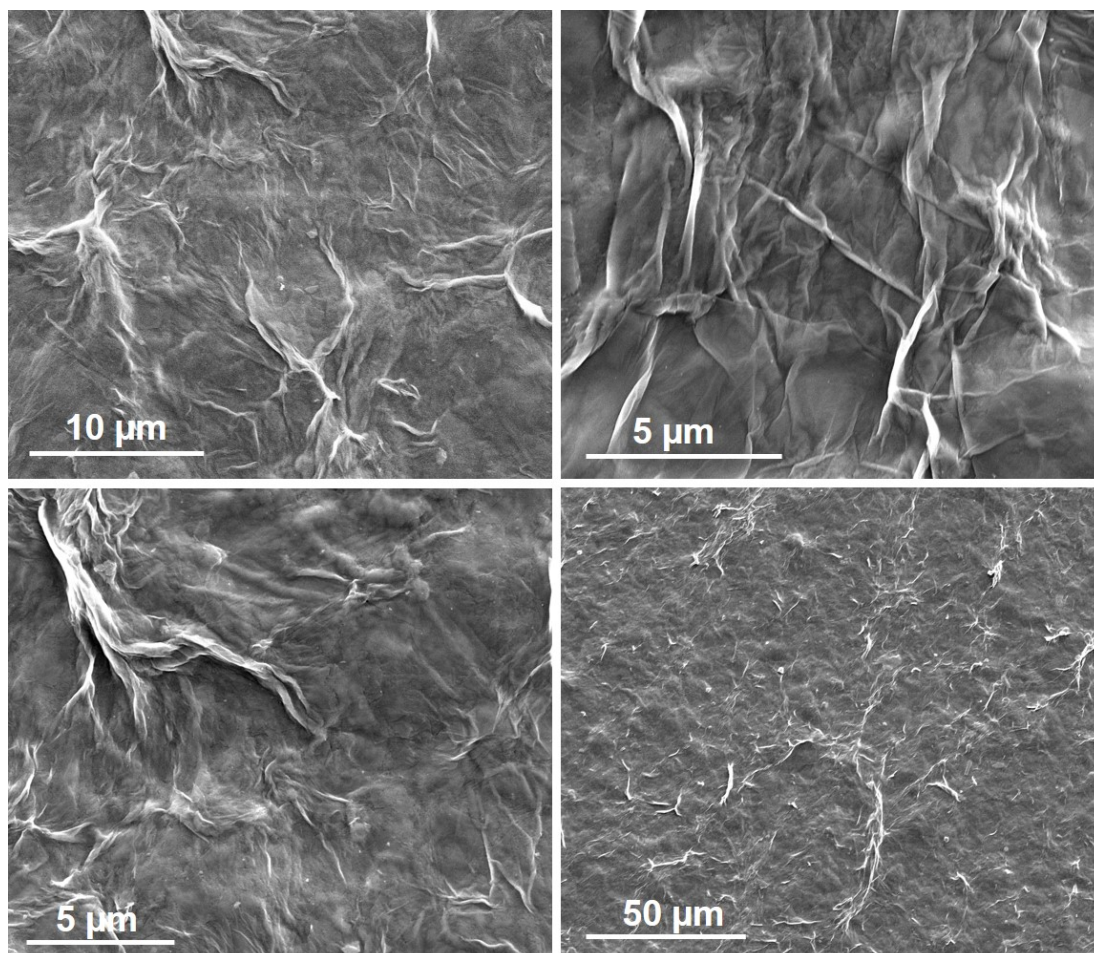


Figure 3.4: SEM images for GO-modified FTO at different magnifications

C 1s spectra in X-ray photoelectron spectroscopic (XPS) measurements of GO (Figure 3.5a) illustrates three main characteristic peaks namely C-C (284.8

eV), C-O (286.8 eV) and another peak of C=O (288.4 eV), which correspond to epoxide, hydroxyl and carboxyl functional groups. O 1s spectra of GO displays two peaks are 531.3 and 533.3 eV corresponding to C=O/O-C=O and C-O-C functional groups respectively (Figure 3.5b). The XPS elemental survey (Figure 3.6b) shows that C/O in GO is about 1.9 while the EDX analysis portray a value of 0.97 (Figure A.2). This difference could be due to the fact that graphene oxide is manually drop-casted onto the FTO hence, the resulting films may not be uniform. Furthermore, EDX gives the bulk concentration (μm depth) of elements in the sample, on the other hand, XPS elemental survey gives the surface chemical composition of the sample (top few nm).

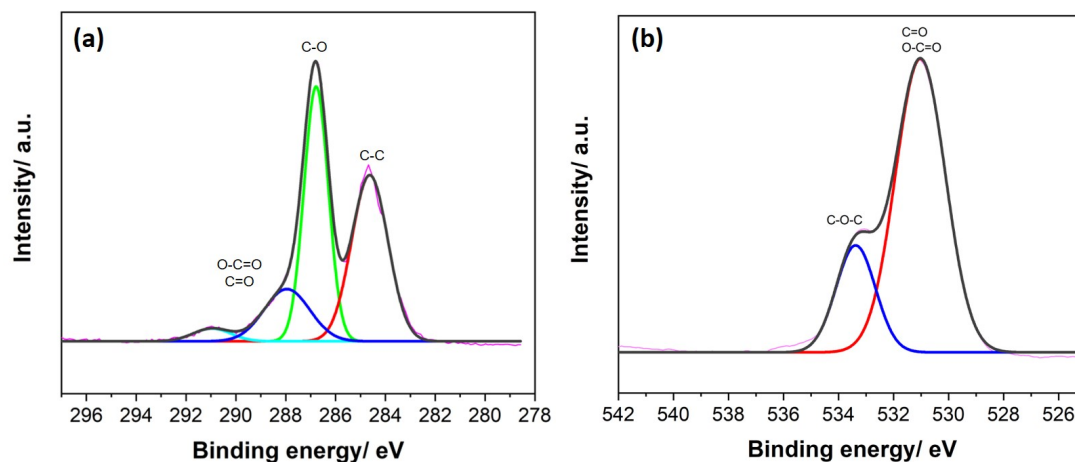


Figure 3.5: High resolution XPS spectra of (a) C 1s and (b) O 1s of GO

The crystal structure of GO was characterized by XRD. Figure 3.6a shows the XRD patterns recorded for graphite flakes and GO-modified FTO. Bragg's law ($n\lambda=2d\sin\theta$) was used to calculate the lattice spacings using $\lambda = 1.5406 \text{ \AA}$ and the 2θ values obtained from XRD patterns. The diffraction peaks of graphite flakes and exfoliated GO appeared at about 26.6° and 11.9° resulting in d-spacing of 0.33 and 0.73 nm respectively. The three latter sharp peaks (26.5° , 33.6° and 37.7°) observed in the GO-modified FTO correspond to signals from FTO glass itself.

The structural and vibrational behavior of GO was further analyzed by Raman spectroscopy (Figure 3.6c). As predicted, GO presented characteristic G and D bands in the region between 1000 and 2000 cm^{-1} . The G band and D bands

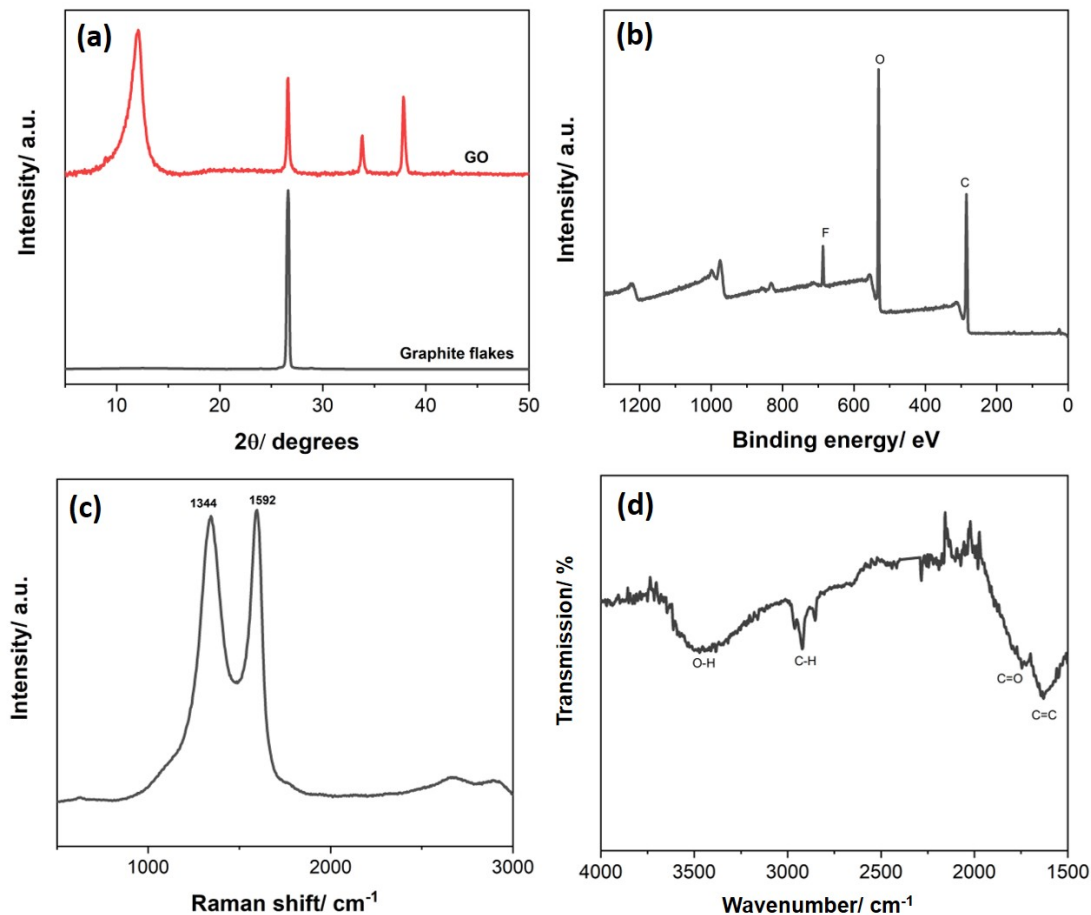


Figure 3.6: (a)XRD patterns for graphite flakes and GO-modified FTO (b)XPS elemental survey (c) Raman spectra and (d) FT-IR measurements for GO-modified FTO

appeared at around 1592 cm^{-1} and 1344 cm^{-1} respectively. In GO, the bands exhibited similar intensities, with a ratio of about 0.98.

Further characterization of GO was carried out to identify chemical bonding present using ATR FT-IR spectrometer.(Figure 3.6d) The main characteristic transmission signals include an intense, broad peak at $\sim 3470\text{ cm}^{-1}$ attributed to O-H stretching of carboxyl groups, an acute peak at $\sim 1740\text{ cm}^{-1}$ allocated to C=O stretching in carbonyl and carboxyl groups and deep peak at $\sim 1620\text{ cm}^{-1}$ related to C=C skeletal vibration of unoxidized graphitic domain. [106] Moreover, a transmission peak was noticed just below 3000 cm^{-1} , which is accounted for C-H asymmetric and symmetric stretching vibrations of the $-\text{CH}_2$ groups.[107]

3.2.3 Electrochemically Reduced Graphene Oxide

3.2.3.1 Synthesis of electrochemically reduced graphene oxide

The electrochemical reduction of graphene oxide was achieved by consecutive sweeping (50 cycles) of GO-modified FTO in 0.1 M PBS from 0 to -1.5 V vs Ag/AgCl. The cyclic voltammetry scan of GO exhibited a well-defined cathodic peak in the first cycle (Figure A.3a). This large change in current (at around -0.8 V) is attributed to the electrochemical reduction of oxygen-containing functional groups in graphene oxide.[108] This cathodic peak slowly levels out in the successive scans indicating that the reduction process is irreversible.

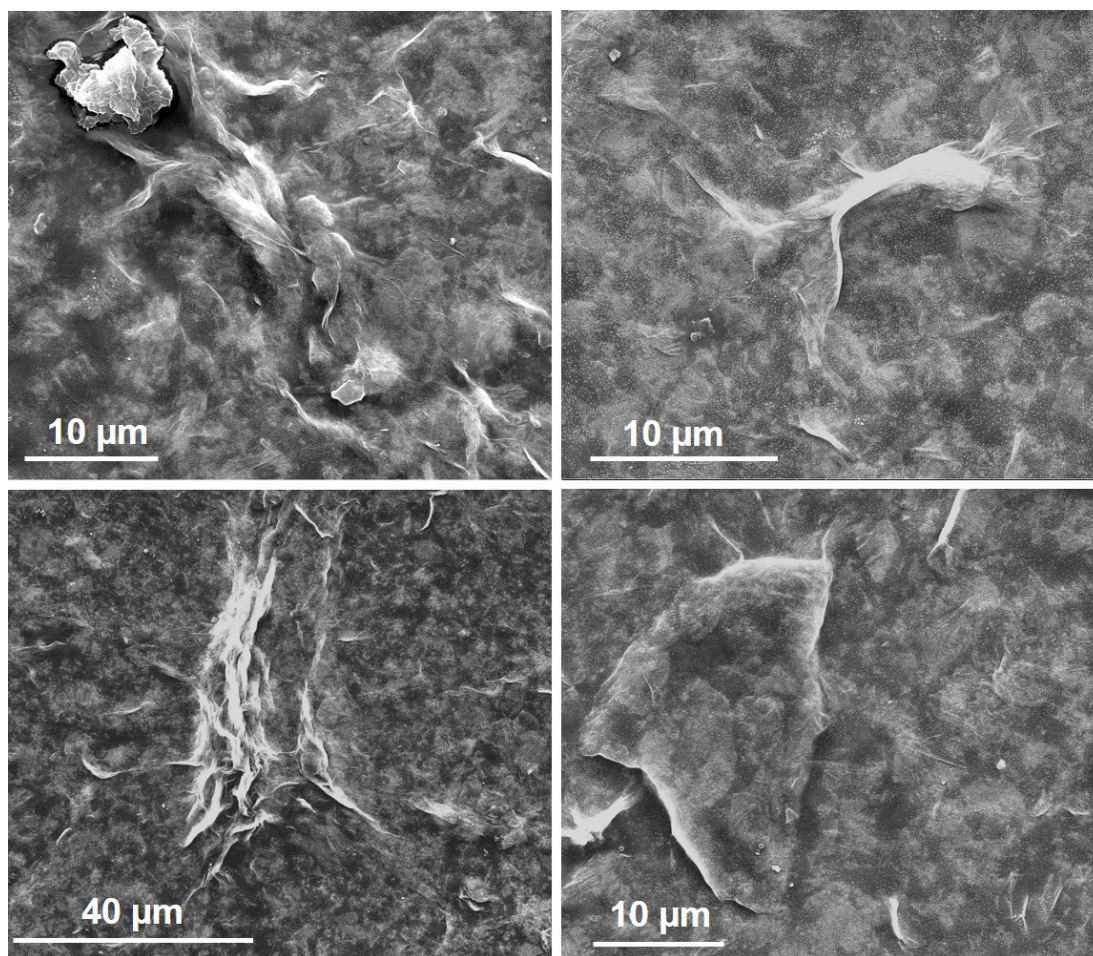


Figure 3.7: SEM images for ERGO-modified FTO at different magnifications

3.2.3.2 Characterization of electrochemically reduced graphene oxide

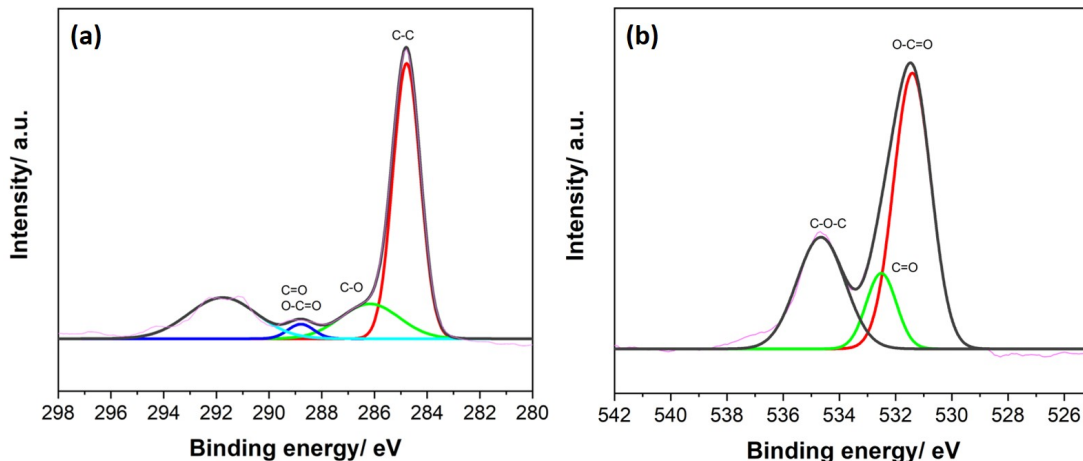


Figure 3.8: High resolution XPS spectra of the (a) C 1s and (b) O 1s of ERGO

After sweeping GO-modified FTO in 0.1 M PBS, the color of GO coating on FTO changed from yellowish-brown to dark brown, providing a slight indication of reduction. [55] Morphological characterization of ERGO- modified FTO (Figure 3.7) was obtained at different beam voltages and spot sizes depending on the image quality. The sample was coated with 3 μ m of Au/Pd to enhance its conductivity. SEM images of ERGO displayed less intense wrinkled sheets that are further apart with a rougher surface than in the case of GO.

X-ray photoelectron spectroscopic (XPS) measurements of ERGO (Figure 3.8) illustrated the same peaks as in GO but with different intensities. C 1s spectra of ERGO exhibited a noticeable decrease in oxygen content as shown by the reduction in C=O, O-C=O and C-O peaks intensities (Figure 3.8a) as well as an increase in C-C peaks due to the partial restoration of the sp² network in graphene. The atomic percentage of elements displayed in XPS survey of ERGO (Figure 3.9b) revealed that the oxygen content was reduced by 50% after reduction (C/O= 4.03 in ERGO). The change in C/O shown by EDX analysis was less significant where the ratio was about 1.4.(Figure A.2b)

The crystal structures of ERGO was characterized by XRD. Figure 3.9a shows the XRD patterns recorded for ERGO-modified FTO. The diffraction peak in

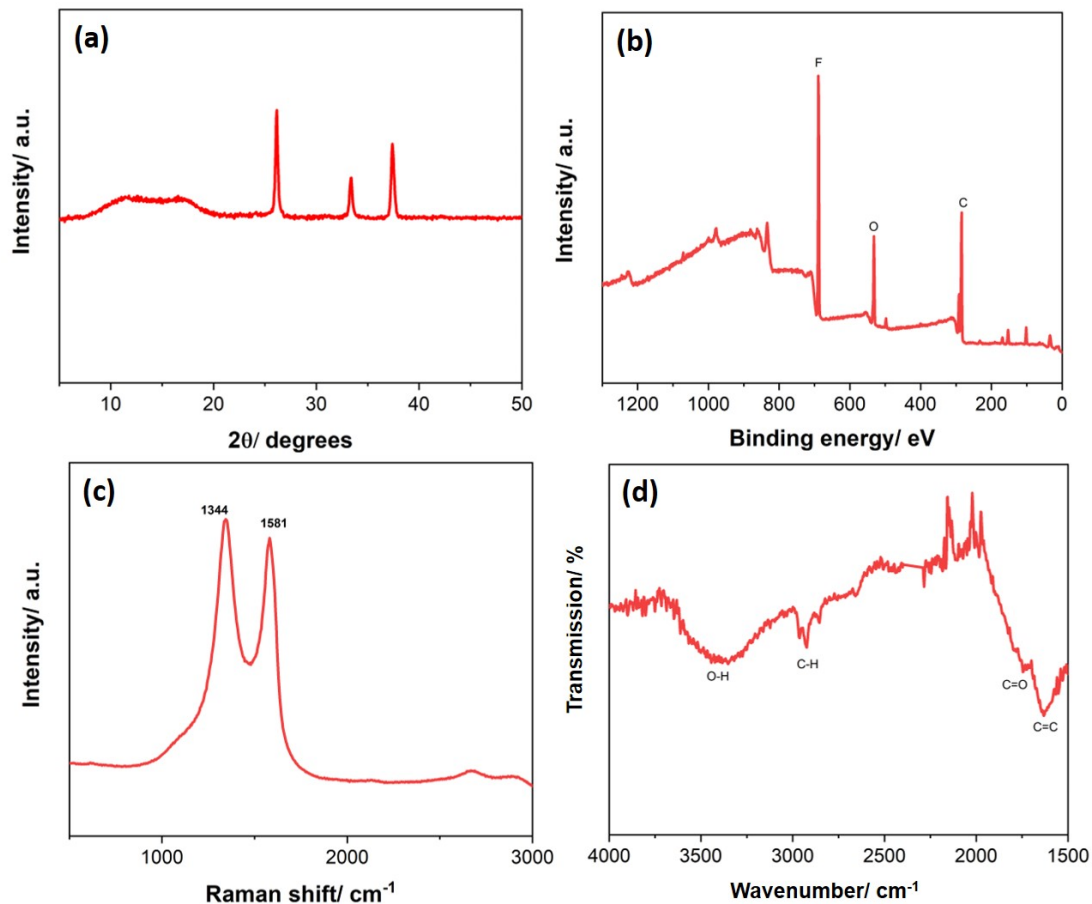


Figure 3.9: (a)XRD patterns for ERGO-modified FTO (b)XPS elemental survey (c) Raman spectra and (d) FT-IR measurements for ERGO-modified FTO

GO (at 11.9 °) completely disappeared after reduction, implying the absence of unreduced graphene oxide as reported in other studies. [61, 109]

The structural and vibrational behavior of ERGO was further analyzed by Raman spectroscopy (Figure 3.9c).As predicted, ERGO presented characteristic G and D bands in the region between 1000 and 2000 cm^{-1} . In comparison to GO, the G band was shift (1581cm^{-1}) due to decrease in the number of defeacts and increase in sp^2 restoration. The intensity of D band was also higher than G ($I_D/I_G \sim 1.1$) which was similar to the value reported by Renteria et. al.[110]

Further characterization of ERGO was carried out to identify chemical bonding present using ATR FT-IR spectrometer.(Figure 3.9d) The same signals presented

in GO are present in ERGO but with slight variations. The main characteristic transmission signals include an intense, broad peak at $\sim 3470\text{ cm}^{-1}$ attributed to O-H stretching of carboxyl groups, an acute peak at $\sim 1740\text{ cm}^{-1}$ allocated to C=O stretching in carbonyl and carboxyl groups, that have slightly decreased upon reduction and small peak at $\sim 1620\text{ cm}^{-1}$ related to C=C skeletal vibration of unoxidized graphitic domain. [106]

3.2.4 ERGO nickel CB[8]-porphyrin composites

3.2.4.1 Synthesis of ERGO nickel CB[8]-porphyrin composites

The electrochemical reduction of graphene oxide nickel CB[8]-porphyrin composites were achieved in the same way as pure GO, by consecutive sweeping (50 cycles) of GO:Ni-P-modified FTO in 0.1 M PBS from 0 to -1.5 V vs Ag/AgCl. In the first run, the electrochemical reduction of the oxygen rich groups of graphene oxide in GO: Ni-P (Figure A.3) occurs at a more positive potential (-0.65 V) than that of pure GO which is around -0.8 V . This cathodic peak slowly levels out in the successive scans indicating that the reduction process is irreversible.

3.2.4.2 Characterization of ERGO nickel CB[8]-porphyrin composites

The ERGO:Ni-P-modified FTO characterized in this section was prepared by drop-casting a layer of Ni-P on top of FTO coated with GO. Morphological characterizations of ERGO:Ni-P-modified FTO (Figure 3.10) were obtained at different beam voltages and spot sizes depending on the image quality. The sample was coated with $3\mu\text{m}$ of Au/Pd to enhance its conductivity. SEM images ERGO:Ni-P displayed stacked ERGO sheets at a low magnification (Figure 3.10) along with many porous micro structures owing to CB[8]-porphyrin assembly.

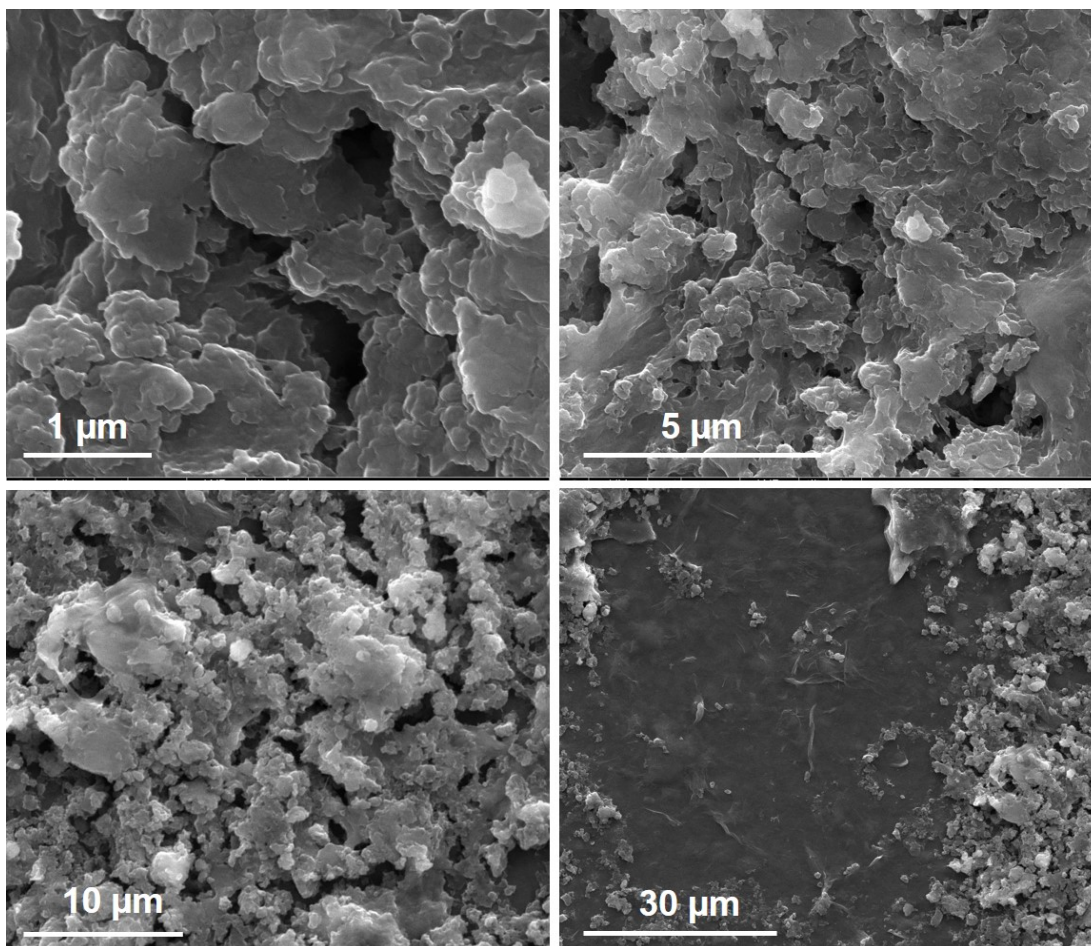


Figure 3.10: SEM images for ERGO:Ni-P-modified FTO at different magnifications

X-ray photoelectron spectroscopic (XPS) measurements of ERGO:Ni-P (Figure 3.11) illustrated similar C1s and O1s to ERGO. The spectrum of N 1s presented a main peak at 399.5 eV which corresponds to pyrrole-like nitrogen.[111] The Nickel 2p spectra of ERGO:Ni-P (Figure 3.11d) showed two peaks attributed oxide and hydroxide forms of nickel with binding energies of about 855.6 and 871.1 eV corresponding to Ni 2p_{3/2} and Ni 2p_{1/2}, respectively, along with their satellites at almost 861.2 and 879.6 eV.[112] The latter peak at 852.4 eV is designated to nickel metal. The C1s spectra also showed a peak at 292.5 eV (Figure 3.11a) and sometimes another at 295 eV (after long sweeps(Figure 3.14)) associated to K2p_{3/2} and K2p_{1/2} signals from residual potassium in PBS solution.[110] Similarly in O1s spectra, an extra peak 536 eV is often detected due to the K₁L₁L₂₃ Auger

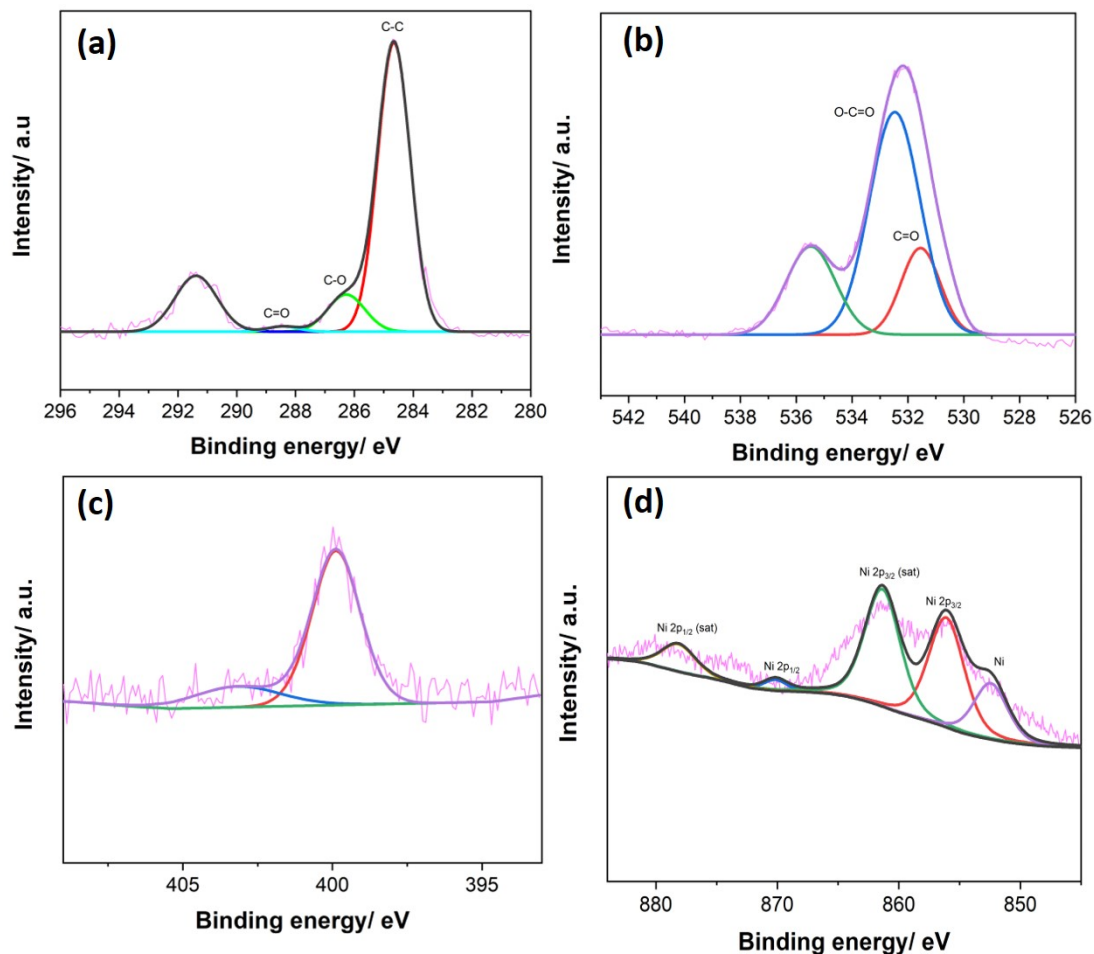


Figure 3.11: High resolution XPS spectra of the (a) C 1s and (b) O 1s (c) N1s and (d) Ni 2p of ERGO:Ni-P

peak of sodium ions present in PBS.[113]The XPS elemental survey showed 73% of the composite is carbon, 1.5% is nitrogen, 21.05% is oxygen and the remaining is nickel. The largest peak ~ 700 eV corresponds to Fluorine coming from FTO. The resulting C/O value in found in XPS (Figure 3.12b) was 3.47 and in EDX is 1.6 (Figure A.2c) .

The crystal structure of the ERGO:Ni-P was characterized by XRD. The XRD measurement for ERGO: Ni-P (Figure 3.12a)demonstrated an extra peak at 8.7° which is equivalent to an interlayer spacing of 1.02 nm. The same peak was also observed in the XRD pattern for Ni-P confirming its identity. This increase in interlayer spacing endorses the formation of Ni-P composite on GO sheets.

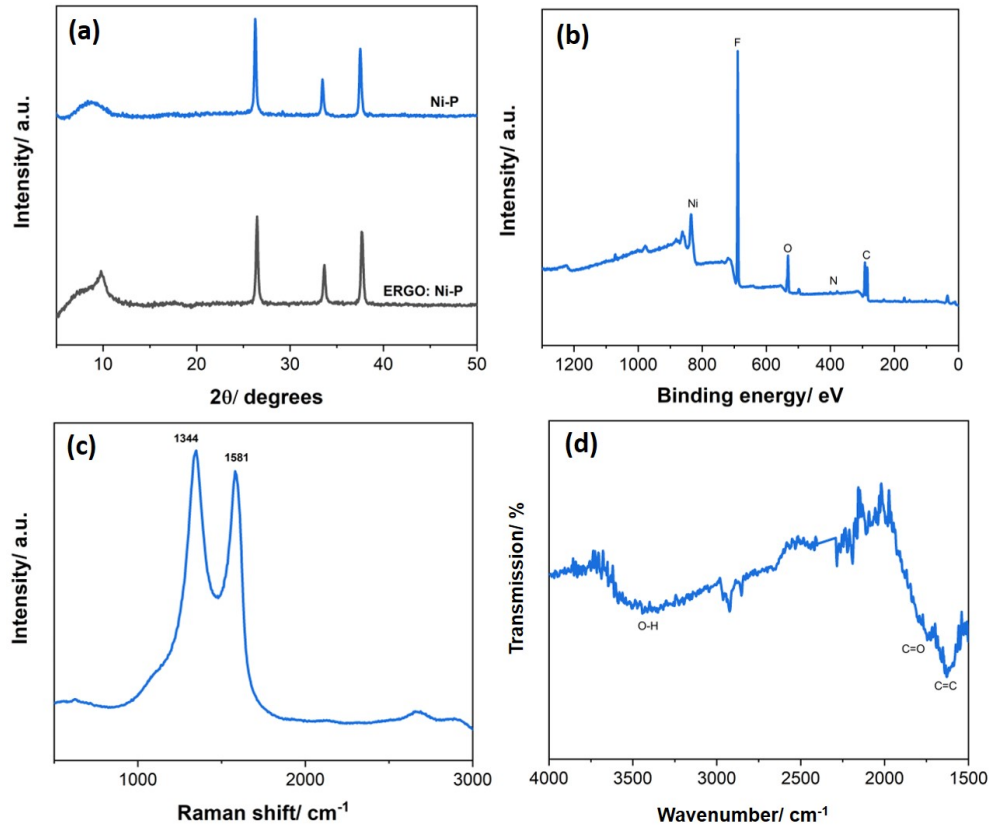


Figure 3.12: (a)XRD patterns for graphite flakes and ERGO: Ni-P-modified FTO (b)XPS elemental survey (c) Raman spectra and (d) FT-IR measurements for ERGO: Ni-P-modified FTO

The structural and vibrational behavior of ERGO: Ni-P was further analyzed by Raman spectroscopy (Figure 3.12c). As predicted, ERGO: Ni-P presented characteristic G and D bands in the region between 1000 and 2000 cm^{-1} . The G band and D bands appeared at around 1592 cm^{-1} and 1344 cm^{-1} respectively. The ratio of intensities of D band to G band was similar to ERGO ~ 1.1 .

The main characteristic transmission signals of ATR FT-IR spectrometer (Figure 3.12d) include a less intense peak at $\sim 3470 \text{ cm}^{-1}$ attributed to O-H stretching of carboxyl groups, an acute peak at $\sim 1740 \text{ cm}^{-1}$ allocated to C=O stretching in carbonyl and carboxyl groups and deep peak at $\sim 1620 \text{ cm}^{-1}$ related to C=C skeletal vibration of unoxidized graphitic domain. [106] Moreover, a transmission peak was noticed just below 3000 cm^{-1} , which are accounted for C-H asymmetric and symmetric stretching vibrations of the $-\text{CH}_2$ groups. [107]

3.2.4.3 Stability of ERGO CB[8]-porphyrin composites

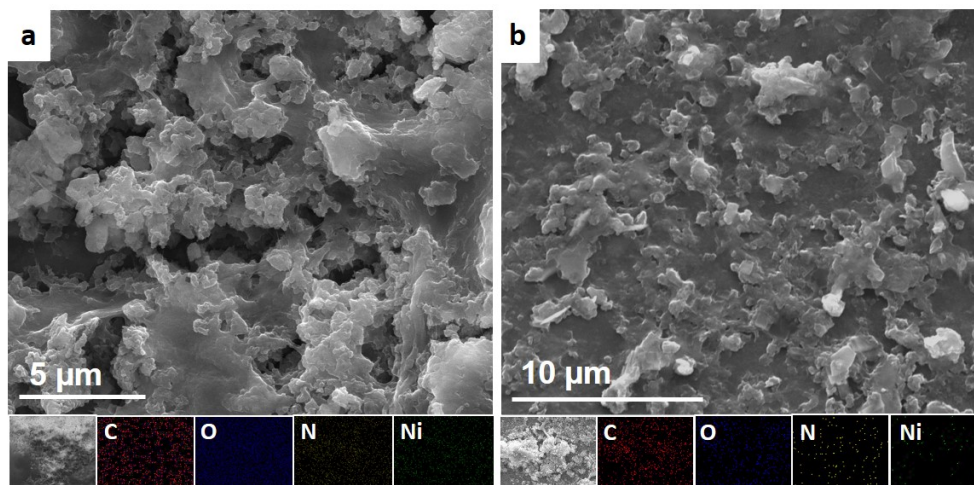


Figure 3.13: SEM images of ERGO: Ni-P (a) before and (b) after 3h CA experiment showing C, O, N and Ni mappings

After carrying out a 3 hour chronoamperometry measurement on the optimum sample, SEM and XPS analysis were performed to examine the durability of this composite. The ERGO: Ni-P coating remained very stable on FTO after CA measurements with no noticeable degradation.

ERGO₁: Ni₂-P displayed insignificant change in morphology and elemental composition. The SEM images of ERGO: Ni-P before and after CA (Figure 3.13) indicate similar porous structures. The elemental mapping of C, O, N and Ni also displayed analogous intensities.

X-ray photoelectron spectroscopic (XPS) measurements of ERGO: Ni-P after CA measurements (Figure 3.14) illustrated similar elemental compositions to initial ERGO: Ni-P. C1s spectra displayed two extra peaks at 292.5 and 295 eV (Figure 3.14(a)) that are linked to K2p_{3/2} and K2p_{1/2} signals from residual potassium in PBS solution. Similarly, O 1s portrayed slight variations with an additional C-OH peak at 533.3 eV and an extra peak 536 eV due to the K₁L₁L₂₃ Auger peak of sodium ions present in PBS.[113] The spectrum of N 1s and Ni 2p presented no

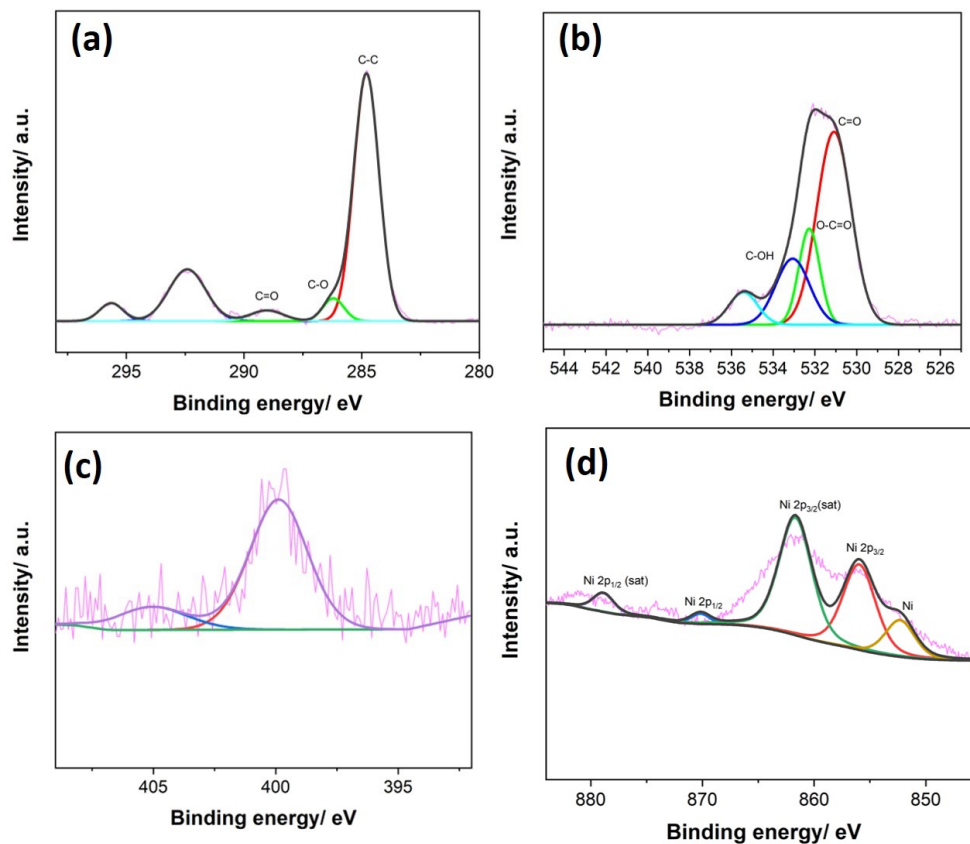


Figure 3.14: XPS spectra of (a) C 1s and (b) O 1s (c) N 1s and (d) Ni 2p after 3h CA for ERGO: Ni-P

change after chronoamperometry measurement. The XPS elemental survey indicated minor change where 71.3% of the composite was carbon, 1.41% was nitrogen, 23.2% was oxygen and the remaining was nickel. The resulting C/O value found in XPS was 3.10 which is comparable to before CA (3.47).

3.3 Electrochemical analysis

A conventional three electrode cell was used for examining the efficiency of catalytic systems for hydrogen evolution reaction. In this regard, Ag/AgCl (3.5 M KCl) was used as the reference electrode, catalyst-modified Fluorine doped Titanium Oxide glass (FTO) as the working electrode, and Pt wire as the counter

electrode. All of the electrochemical experiments were performed using CHI-670 potentiostat at room temperature. The FTO surface was first cleaned with detergent, then with deionized water and isopropanol by ultrasonication for 15 minutes with each. It was then activated by drying in vacuum oven at 450 °C for 2 hours. The reaction system was purged with Argon for 30 min to remove the dissolved gases in electrolyte prior to taking measurements. All potentials were measured versus Ag/AgCl reference electrode and were reported versus the reversible hydrogen electrode (RHE) using the Nernst equation:

$$E_{RHE} = E_{Ag|AgCl|KCl(sat.)} + 0.059pH + E_{Ag|AgCl|KCl(sat.)}^o \quad (3.1)$$

Where E_{RHE} is potential estimated vs. RHE (overpotential), $E_{Ag|AgCl|KCl(sat.)}$ is the measured potential vs. Ag|AgCl|KCl(sat.) electrode (voltage measured in potentiostat) and $E_{Ag|AgCl|KCl(sat.)}^o$ is the standard electrochemical potential of the Ag|AgCl|KCl(sat.) electrode i.e. 0.1976 V. Nernst equation for hydrogen evolution reaction then reduces to:

$$E_{RHE} = E_{Ag|AgCl|KCl(sat.)} + 0.059pH + 0.1976 \quad (3.2)$$

3.3.1 Nickel CB[8]-porphyrin

Table 3.1: Compositions of all Ni-P inks

	CB[8]-Porphyrin(mg)	Nickel acetate (mg)	DH ₂ O (μ l)	Ethanol (μ l)
Ni_{0.5}-P	2	1	125	25
Ni₁-P	2	2	125	25
Ni₂-P	2	4	125	25

The effect of varying nickel concentration was examined by using half (Ni_{0.5}-P), equal (Ni₁-P) and double (Ni₂-P) the weight of nickel acetate with respect to CB[8]-porphyrin framework. The percentage of nickel in the composites were calculated to be 11.2, 23.6 and 47.2% respectively. The ink was prepared by mechanically grinding certain weights of nickel acetate and CB[8]-porphyrin using

pestle and mortar for 10 minutes followed by adding specific volumes of water, ethanol and Nafion (Table 3.1). In most cases, Nafion was used for stable adhesion of ink onto FTO. For the sample the Ni₂-P for instance, the ink used was prepared by loading 4 mg of nickel acetate in CB[8]-porphyrin (2mg) with physical mixing using pestle and mortar for 10 minutes. To this solid mixture, 125 μ l of water, 25 μ l ethanol and 10 μ l of Nafion (5%) were added and stirred magnetically overnight forming a consistent ink. The compositions of the nickel CB[8]-porphyrin inks are shown in the Table 3.1.

Table 3.2: Electrochemical parameters for Ni-P samples from potentiometry

	Onset	$\eta@10\text{mAcm}^{-2}$	b	jo	j @$\eta = -0.894\text{V}$	TOF
Ni₅-P	-288	-967	41.0	0.115	-8.66	0.0837
Ni₁-P	-275	-954	33.4	0.042	-8.7	0.039
Ni₂-P	-253	-894	50.1	0.242	-10	0.0242

The electrochemical performance of all three Ni-P composites was studied using potentiometry measurements. Linear sweep voltammetry was conducted at a scan rate of 1 mVs⁻¹ from 0 to 2 V vs Ag/AgCl in Argon saturated 0.1 M KOH. Ni-P-modified FTO was prepared by simply drop-casting 20 μ l of desired Ni-P ink (after overnight stirring) onto half of clean FTO (1 cm²) then drying it at 60 °C for one hour. The onset and $\eta@10\text{mAcm}^{-2}$ potentials were obtained from linear sweep voltammetry (Figure 3.15a), the Tafel plot was produced using these values at potentials close to onset.(Figure 3.15b)

Table 3.2 shows the activity parameters of all Ni-P composites, where potentials are reported in mV, Tafel slope (b) in mVdec⁻¹, current densities in mAcm⁻² and TOF in s⁻¹.The lowest onset and $\eta@10\text{mAcm}^{-2}$ potentials were observed in the composite with double the weight of nickel acetate with respect to CB[8]-porphyrin (Ni₂-P). Furthermore, this composite attained the largest exchange current density value among the three indicating fastest kinetics.

The turnover frequencies were calculated using the current density at the overpotential of 10 mAcm⁻² for Ni₂-P (j @ $\eta = -0.894\text{V}$) as it is chosen as the optimum sample for this section. Cyclic voltammetry (CA) and chronoamperometry

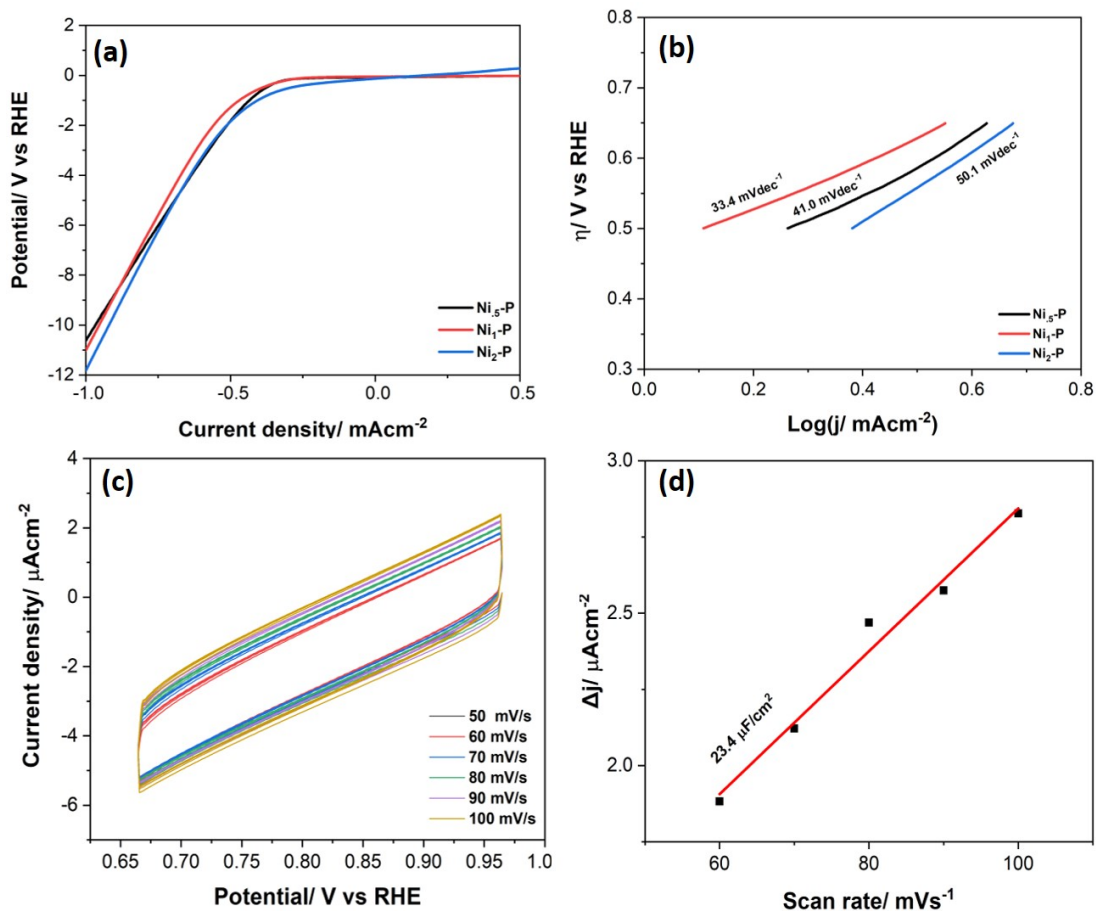


Figure 3.15: (a) Polarization curves of Ni_{0.5}-P, Ni₁-P and Ni₂-P in 0.1 M KOH at scan rate of 1 mV s⁻¹ (b) Tafel plot of same composites showing Tafel slope (c) CV curves in double layer region at scan rates of 50, 60, 70, 80, 90 and 100 mV s⁻¹ of Ni₂-P (d) The capacitive currents at 0.81 V as a function of scan rate for Ni₂-P ($\Delta j = j_{anodic} - j_{cathodic}$)

(CA) measurements were performed on Ni₂-P modified FTO. The current density value obtained from chronoamperometry was used to calculate the number of moles of hydrogen produced per gram in an hour (21.8 mmolh⁻¹g⁻¹). This current density with the $j@ -0.34V$ from linear sweep voltammetry, were used obtain faradaic efficiency. The electroactive surface area was estimated by performing cyclic voltammetry cycles at different scan rates in the non-faradaic region. The difference in anodic and cathodic current densities in each scan rate was plot against scan rate and the slope corresponded to double layer capacitance (23.4 μFcm^{-2}).

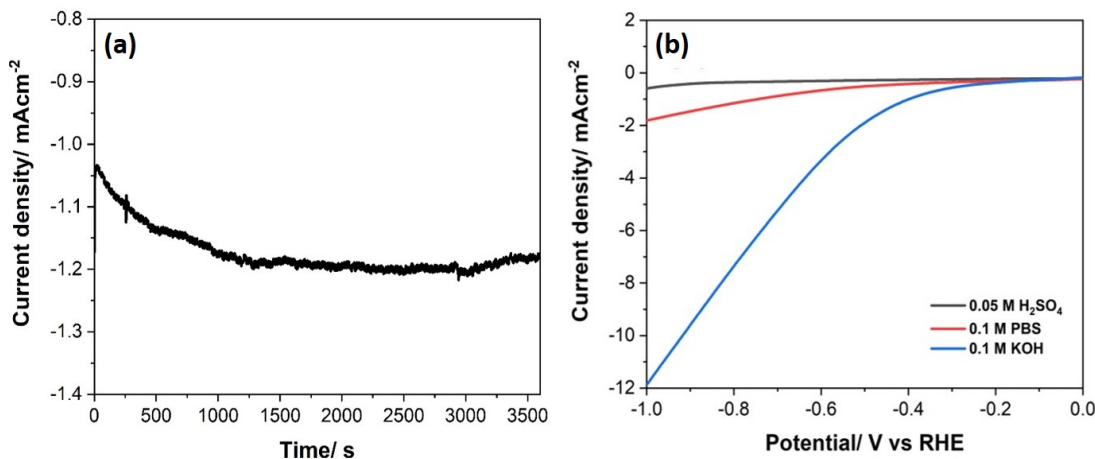


Figure 3.16: (a) Chronoamperometry (CA) for Ni₂-P at -0.34 V in 0.1 M KOH (b) Polarization curves for Ni₂-P in acidic, neutral and basic media at a scan rate of 1 mV/s

The optimum sample with double weight ratio of nickel acetate to CB[8]-porphyrin (Ni₂-P) was further examined in other media (Figure 3.16b). On contrary to its activity in 0.1 M KOH, the composite displayed negligible performance in acidic and neutral media. Consequently, the electrochemical studies of the corresponding GO nickel CB[8]-porphyrin and ERGO nickel CB[8]-porphyrin composites were performed in basic medium (0.1 M KOH).

3.3.2 GO Nickel CB[8]-porphyrin

The effect of integrating graphene oxide into nickel CB[8]-porphyrin framework was examined by using two different sample preparation methods. Initially (section 3.3.2.1), graphene oxide was added to the usual nickel acetate - CB[8]-porphyrin ink and left to stir overnight (GO-Ni-P). In the second part (section 3.3.2.2), a layer of graphene oxide was first dropped casted onto the FTO and left to dry, followed by a layer of nickel acetate - CB[8]-porphyrin ink (GO:Ni-P). Optimization measurements were carried out to find the best sample preparation method and the most ideal compositions of graphene oxide and nickel acetate with respect to CB[8]-porphyrin.

3.3.2.1 All in one ink (GO- Ni-P)

GO-Ni-P composite was prepared by mechanically mixing nickel acetate and CB[8]-porphyrin assembly in certain weight ratios and magnetically stirring overnight. The effect of varying nickel concentration was first examined by using half (GO₁-Ni_{0.5}-P), equal (GO₁-Ni₁-P) and double (GO₁-Ni₂-P) the weight of nickel acetate with respect to CB[8]-porphyrin framework. Using the optimum nickel amount, the influence of graphene oxide concentration was investigated using half (GO_{0.5}-Ni₂-P) and double (GO₂-Ni₂-P) graphene oxide weight with respect to CB[8]-porphyrin. For sample GO₁-Ni₂-P for instance, the ink used was prepared by loading 4 mg of nickel acetate in CB[8]-porphyrin (2mg) and 2 mg GO powder with physical mixing using pestle and mortar for 10 minutes. To this solid mixture, 250 μ l of water, 50 μ l ethanol and 20 μ l of Nafion (5%) were added and stirred magnetically overnight forming a consistent ink. The solvent volumes were chosen with respect to the catalysts CB[8]-porphyrin and graphene oxide, not co-catalyst nickel.

Table 3.3: Compositions of GO-Ni-P samples (all in one ink)

<i>Optimizing Ni</i>					
	CB[8]-porphyrin(mg)	Ni acetate (mg)	GO (mg)	DH ₂ O (μ l)	Ethanol(μ l))
GO ₁ -Ni _{0.5} -P	2	1	2	250	50
GO ₁ -Ni ₁ -P	2	2	2	250	50
GO ₁ -Ni ₂ -P	2	4	2	250	50
<i>Optimizing GO</i>					
	CB[8]-porphyrin(mg)	Ni acetate (mg)	GO (mg)	DH ₂ O (μ l)	Ethanol(μ l))
GO _{0.5} -Ni ₂ -P	2	2	1	188	37
GO ₂ -Ni ₂ -P	2	2	4	375	75

The electrochemical performance of all five GO-Ni-P composites was studied using potentiometry measurements. Linear sweep voltammetry was conducted at a scan rate of 1 mVs⁻¹ from 0 to 2 V vs Ag/AgCl in Argon saturated 0.1 M KOH. GO-Ni-P-modified FTO was prepared by simply drop-casting 20 μ l of desired GO-Ni-P ink (after overnight stirring) onto clean FTO then drying it at 60 °C for one hour.

Table 3.4 shows the activity parameters of all GO-Ni-P composites, where potentials are reported in mV, Tafel slope (b) in mVdec⁻¹, current densities in

mAcm⁻² and TOF in s⁻¹. There is no definite trend on the effect of varying nickel acetate or graphene oxide concentrations, however changing nickel concentration had a higher impact on activity than GO.

Table 3.4: Electrochemical parameters for GO-Ni-P samples (all in one ink)

	Onset	$\eta@10\text{mAcm}^{-2}$	b	jo	j @$\eta = -0.894\text{V}$	TOF
GO_{0.5}-Ni₂-P	-270	-860	45.2	0.219	-9.46	0.0343
GO₂-Ni₂-P	-258	-996	42.7	0.146	-7.27	0.0527
GO₁-Ni₅-P	-185	-917	51.9	0.375	-8.04	0.156
GO₁-Ni₁-P	-180	-929	41.3	0.0811	-8.09	0.0782
GO₁-Ni₂-P	-152	-834	32.3	0.0523	-10	0.0484

The composite with double amount of nickel acetate but equal amount of GO with respect to CB[8]-porphyrin (GO₁-Ni₂-P) exhibited the best activity owing to its smallest onset and potential at 10 mAcm⁻² (Figure 3.17a). The optimum sample attained a Tafel slope of 32.3 mVdec⁻¹ and a low exchange current density value of 0.0523 mAcm⁻². The activity of GO₁-Ni₅-P was found remarkably similar to GO₁-Ni₂-P with even better exchange current density and TOF but poorer potentials.

The electrochemical activity and stability of GO₁-Ni₂-P was further investigated using Cyclic voltammetry (CV) and chronoamperometry (CA) measurements. Cyclic voltammetry was again performed between -0.1 and -0.2 V vs Ag/AgCl (equivalent to 0.76- 0.86 V vs RHE) at six different scan rates (50, 60, 70, 80, 90 and 100 mVs⁻¹) (Figure 3.17c). The double layer capacitance of GO₁-Ni₂-P was found to be 29.3 μFcm^{-2} which is comparable to Ni₂-P indicating the inadequate influence on activity upon mechanical addition of GO to ink (Figure 3.17d). Similarly, the amount of hydrogen produced with and without GO were analogous. Chronoamperometry analysis was used to evaluate the durability of the composite and estimate the theoretical amount of hydrogen produced (mol per gram in an hour) using Faraday's law (Figure A.1). The composite was merely stable after chronoamperometric analysis with few degradations of coating into electrolyte. The amount of hydrogen produced by GO₁-Ni₂-P in one hour was even lower than Ni₂-P (about 19.8 mmolh⁻¹g⁻¹). Furthermore, the faradaic efficiency, approximated using the number of moles of hydrogen produced and the total charge passed during the reaction, was found to be around 89.8% . These

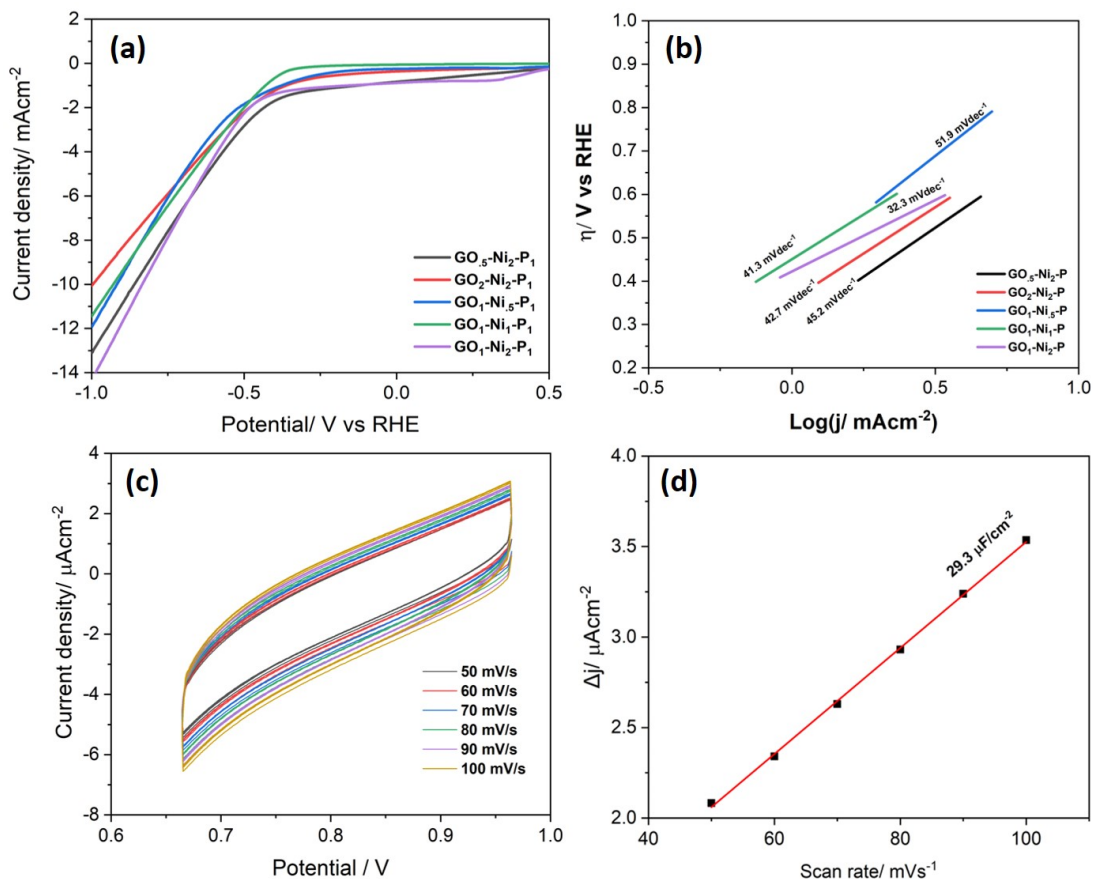


Figure 3.17: (a) Polarization curves of $\text{GO}_{1.5}\text{-Ni}_2\text{-P}$, $\text{GO}_1\text{-Ni}_1\text{-P}$, $\text{GO}_1\text{-Ni}_2\text{-P}$, $\text{GO}_{0.5}\text{-Ni}_2\text{-P}$ and $\text{GO}_2\text{-Ni}_2\text{-P}$ in 0.1 M KOH at scan rate of 1 mV s^{-1} (b) Tafel plot of same composites showing Tafel slope (c) CV curves in double layer region at scan rates of 50, 60, 70, 80, 90 and 100 mV s^{-1} of $\text{GO}_1\text{-Ni}_2\text{-P}$ (d) The capacitive currents at 0.81 V as a function of scan rate for $\text{GO}_1\text{-Ni}_2\text{-P}$ ($\Delta j = j_{\text{anodic}} - j_{\text{cathodic}}$)

electrochemical measurements indicate that the direct assembly of graphene oxide into nickel CB[8]-porphyrin composite does not have a significant effect on catalytic efficiency.

3.3.2.2 Layers (GO:Ni-P)

GO: Ni-P- modified FTO was achieved by first drop-casting a layer of GO ink then a layer of nickel CB[8]-porphyrin composite separately onto a clean FTO. Nickel CB[8]-porphyrin (Ni-P) was prepared as mentioned in the beginning of section

Table 3.5: Compositions of all GO:Ni-P samples

<i>Optimizing Ni</i>					
	Ni-P layer		GO layer		
	CB[8]-porphyrin(mg)	Ni acetate (mg)	GO (mg)	DH ₂ O (μ l)	Ethanol(μ l)
GO ₁ :Ni ₅ -P	2	1	2	125	25
GO ₁ :Ni ₁ -P	2	2	2	125	25
GO ₁ :Ni ₂ -P	2	4	2	125	25
<i>Optimizing GO</i>					
	Ni-P layer		GO layer		
	CB[8]-porphyrin(mg)	Ni acetate (mg)	GO (mg)	DH ₂ O (μ l)	Ethanol (μ l)
GO _{.5} :Ni ₂ -P	2	2	1	63	12
GO ₂ :Ni ₂ -P	2	2	4	250	50

2.3. and later in 3.3.1. For the sample GO₁:Ni₂-P for instance, the ink used was prepared by loading 4 mg of nickel acetate in CB[8]-porphyrin (2mg) with physical mixing using pestle and mortar for 10 minutes. To this solid mixture, 125 μ l of water, 25 μ l ethanol and 10 μ l of Nafion (5%) were added and stirred magnetically overnight forming a consistent ink. The graphene oxide ink was prepared separately by adding 2 mg of graphite oxide powder to 125 μ l of water, 25 μ l ethanol then applying ultrasonication for an hour. Ultimately, The GO: Ni-P modified FTO was established by simply drop-casting 10 μ l of GO ink along with 10 μ l Nafion (5%) covering only half of the FTO (1 cm²). Once this coating dried, a layer of Ni-P was drop-casted(10 μ l) on top. These working electrodes were finally dried at 60 °C for an hour. Note that Table 3.5 only includes the solvent volumes of GO ink, the solvent compositions for Ni-P inks are as stated in the previous sections.

Table 3.6: Electrochemical parameters for GO:Ni-P composites

	Onset	$\eta@10\text{mAcm}^{-2}$	Tafel slope	jo	j @ $\eta = -0.879\text{V}$	TOF
GO _{.5} : Ni ₂ -P	-158	-940	48.5	0.0831	-8.61	0.0208
GO ₂ : Ni ₂ -P	-205	-1040	41.8	0.0737	-6.88	0.0166
GO ₁ : Ni ₅ -P	-271	-1050	53.9	0.169	-6.35	0.0614
GO ₁ : Ni ₁ -P	-164	-982	43.9	0.102	-7.77	0.0376
GO ₁ : Ni ₂ -P	-145	-879	51.3	0.239	-10	0.0242

Table 3.6 shows the activity parameters of all GO-Ni-P composites, where potentials are reported in mV, Tafel slope (b) in mVdec⁻¹, current densities in mAcm⁻² and TOF in s⁻¹. Again, there is no definite trend on the effect of varying nickel acetate or graphene oxide concentrations, however changing nickel concentration had a higher impact on activity than GO.

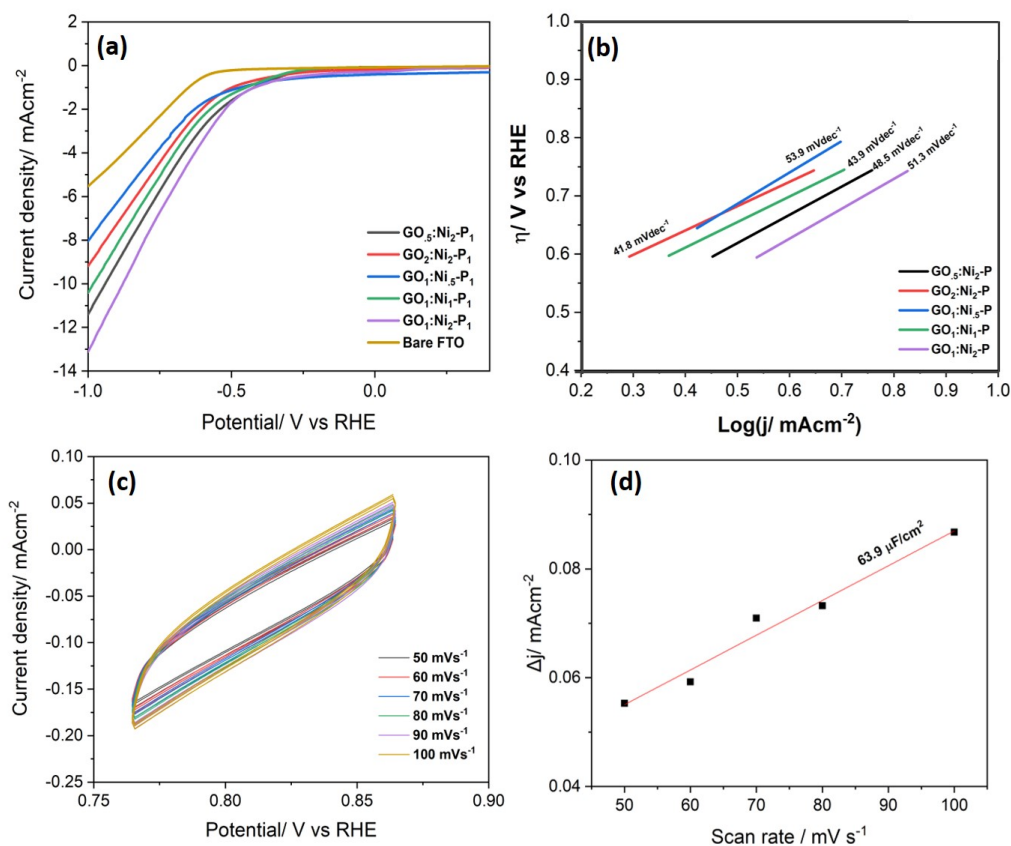


Figure 3.18: (a) Polarization curves of $\text{GO}_1:\text{Ni}_{1.5}\text{-P}$, $\text{GO}_1:\text{Ni}_1\text{-P}$, $\text{GO}_1:\text{Ni}_2\text{-P}$, $\text{GO}_{.5}:\text{Ni}_2\text{-P}$ and $\text{GO}_2:\text{Ni}_2\text{-P}$ in 0.1 M KOH at scan rate of 1 mV s^{-1} (b) Tafel plot of same composites showing Tafel slope (c) CV curves in double layer region at scan rates of 50, 60, 70, 80, 90 and 100 mV s^{-1} of $\text{GO}_1:\text{Ni}_2\text{-P}$ (d) The capacitive currents at 0.81 V as a function of scan rate for $\text{GO}_1:\text{Ni}_2\text{-P}$ ($\Delta j = j_{\text{anodic}} - j_{\text{cathodic}}$)

The composite with double amount of nickel acetate but equal amount of GO with respect to CB[8]-porphyrin ($\text{GO}_1\text{-Ni}_2\text{-P}$) exhibited the best activity owing to its smallest onset and potential at 10 mAcm^{-2} (Figure 3.17a). The optimum sample attained a Tafel slope of 51.3 mVdec^{-1} and exchange current density of 0.239 mAcm^{-2} . This numerical slope value of $\text{GO}_1\text{-Ni}_2\text{-P}$ (51.3 mVdec^{-1}) indicated that it undergoes Volmer–Heyrovsky mechanism for HER.

The electrochemical activity and stability of $\text{GO}_1:\text{Ni}_2\text{-P}$ was further investigated using Cyclic voltammetry (CV) and chronoamperometry (CA) measurements. Cyclic voltammetry was again performed between -0.1 and -0.2 V vs

Ag/AgCl (equivalent to 0.76 - 0.86 V vs RHE) at six different scan rates (50, 60, 70, 80, 90 and 100 mVs⁻¹). The double layer capacitance of Ni₂-P was significantly enhanced upon addition of graphene oxide layer. Using a layer of GO rather than manually mixing with composite improved its double layer capacitance ($C_{dl} = 63.9 \mu\text{Fcm}^{-2}$), hence electroactive surface area, by 2.7 times.

Moreover, Chronoamperometry analysis was used to evaluate the durability of the composite and estimate the theoretical amount of hydrogen produced (mol per gram in an hour) using Faraday’s law (Figure A.1). The integration of graphene oxide has not only improved the electrochemical activity of composite but its stability too. The GO₁:Ni₂-P-modified FTO remained stable without peeling off after chronoamperometric analysis. The amount of hydrogen produced by GO₁:Ni₂-P in one hour was greater than Ni₂-P ($\sim 24.6 \text{ mmolh}^{-1}\text{g}^{-1}$). Furthermore, the faradaic efficiency was found to be much more significant when GO was added as a layer around 98% .

3.3.3 ERGO Nickel CB[8]-porphyrin

3.3.3.1 All in one ink (ERGO-Ni-P)

Table 3.7: Electrochemical parameters for ERGO:Ni-P composites

	Onset	$\eta@10\text{mAcm}^{-2}$	b	jo	j @$\eta = -0.785\text{V}$	TOF
ERGO_{.5}-Ni₂-P	-177	-900	49.6	0.238	-7.63	0.0277
ERGO₂-Ni₂-P	-261	-834	38.2	0.113	-8.77	0.0636
ERGO₁-Ni_{.5}-P	-232	-825	37.1	0.0977	-8.95	0.173
ERGO₁-Ni₁-P	-170	-861	50.7	0.369	-8.35	0.0808
ERGO₁-Ni₂-P	-126	-785	52.9	0.419	-10	0.0484

The reduction of composites was achieved by consecutive cyclic voltammetry scans of GO-nickel CB[8]-porphyrin frameworks (section 3.3.2.1) in 0.1 M PBS. The electrochemical parameters of all ERGO-Ni-P samples were obtained from polarization curves (Figure 3.19a). ERGO₁-Ni₂-P (all in one ink) demonstrated a good electrocatalytic activity, having a low onset (-126 mV), $\eta@10\text{mAcm}^{-2}$ (-785 mV) potentials and large exchange current density (0.419 mAcm⁻²), This

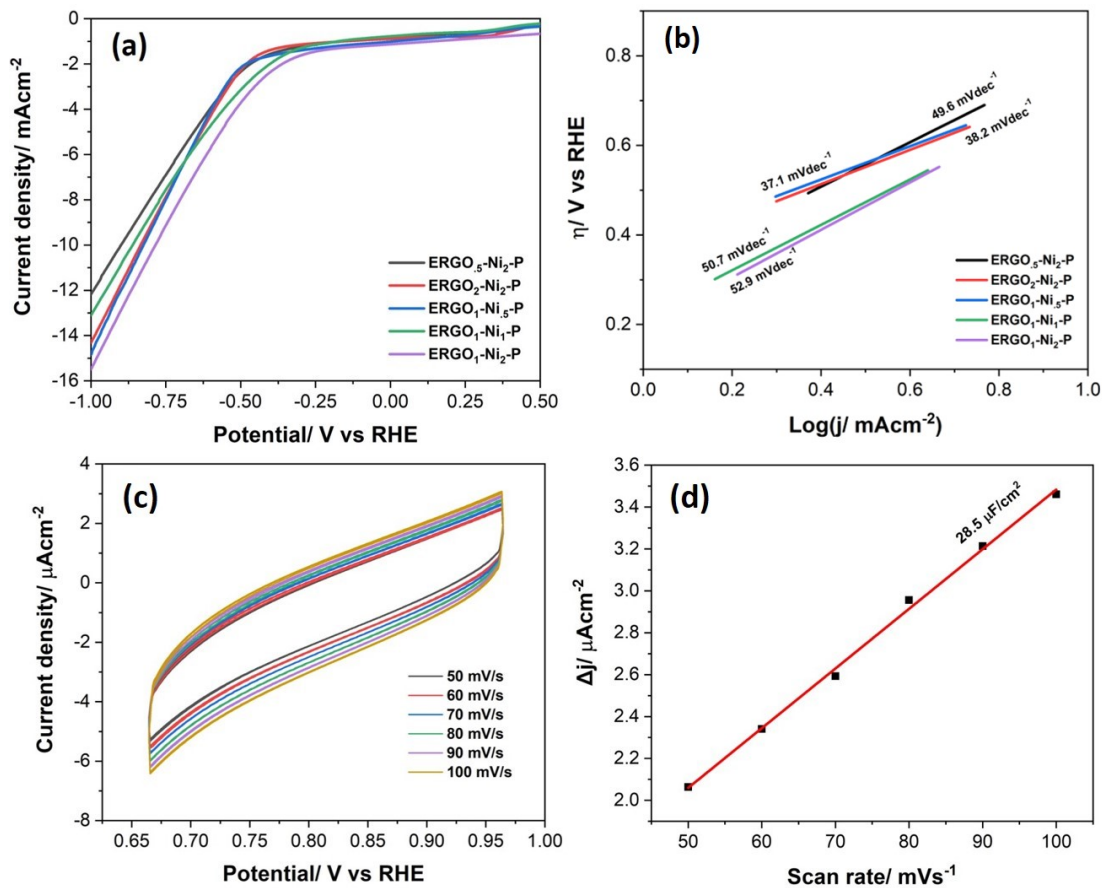


Figure 3.19: (a) Polarization curves of ERGO₁-Ni₅-P, ERGO₁-Ni₁-P, ERGO₁-Ni₂-P, ERGO_{0.5}-Ni₂-P and ERGO₂-Ni₂-P in 0.1 M KOH at scan rate of 1 mV s^{-1} (b) Tafel plot of same composites showing Tafel slope (c) CV curves in double layer region at scan rates of 50, 60, 70, 80, 90 and 100 mV s^{-1} of ERGO₁-Ni₂-P (d) The capacitive currents at 0.81 V as a function of scan rate for ERGO₁-Ni₂-P ($\Delta j = j_{\text{anodic}} - j_{\text{cathodic}}$)

optimum sample attained a Tafel slope of 52.9 mVdec^{-1} which indicated that it undergoes Heyrovsky mechanism for HER. The composite exhibited excellent kinetic activity with better exchange current density than all Ni-P and GO Ni-P composites studied in previous sections.

Table 3.7 shows the activity parameters of all ERGO-Ni-P composites, where potentials are reported in mV, Tafel slope (b) in mVdec^{-1} , current densities in mAcm^{-2} and TOF in s^{-1} . Although ERGO₁-Ni₂-P displayed good electrochemical activity, it presented a quite low C_{dl} implying small electroactive surface area

($C_{dl} = 28.5 \mu\text{Fcm}^{-2}$). Furthermore, the reduction of the composite was not clear as cathodic reduction peak in in 0.1 M PBS was not sharp. Therefore, no further studies were performed using all in one ink method.

3.3.3.2 Layers (ERGO:Ni-P)

Similar to section 3.3.3.1, after dropcasting a layer of GO followed by a layer of Ni-P, the reduction of graphene oxide was achieved by consecutive cyclic voltammetry scans in 0.1 M PBS. The electrochemical parameters of all ERGO: Ni-P samples were obtained from polarization curves (Figure 3.20). All the reduced composites displayed better activities than before reduction, having lower onset and $\eta@10\text{mAcm}^{-2}$ potentials. Among all reduced composites, ERGO₁:Ni₂-P (layers) in specific presented outstanding electrocatalytic activity with very small onset (-30 mV) and $\eta@10\text{mAcm}^{-2}$ (-717 mV) potentials. The exchange current density was also found to be noteworthy (0.745 mAcm^{-2}) and the Tafel slope (53.7 mVdec^{-1}) indicated HER reaction is through Volmer–Heyrovsky mechanism.

Table 3.8 shows the activity parameters of all ERGO-Ni-P composites, where potentials are reported in mV, Tafel slope (b) in mVdec^{-1} , current densities in mAcm^{-2} and TOF in s^{-1} .

Table 3.8: Electrochemical parameters for ERGO:Ni-P composites

	Onset	$\eta@10\text{mAcm}^{-2}$	b	jo	j @$\eta = -717 \text{ V}$	TOF
ERGO_{.5}:Ni₂-P	-186	-887	47.1	0.192	-6.018	0.0291
ERGO₂:Ni₂-P	-191	-949	65.2	0.402	-5.319	0.0257
ERGO₁:Ni_{.5}-P	-270	-1032	44.8	0.103	-4.099	0.0793
ERGO₁:Ni₁-P	-154	-917	60.8	0.335	-5.372	0.052
ERGO₁:Ni₂-P	-30	-717	53.7	0.745	-10	0.0484
Bare FTO	-550					

In comparison to all studied composites, ERGO₁:Ni₂-P revealed the most preminent electrocatalytic activity. It was obvious, given C_{dl} values, that adding a layer of GO instead of mechanical mixing lead to the increase the electroactive surface area. The C_{dl} of ERGO₁:Ni₂-P was almost 8 times as larger as Ni₂-P while the onset and $\eta@10\text{mAcm}^{-2}$ were significantly smaller. TOF presents poor

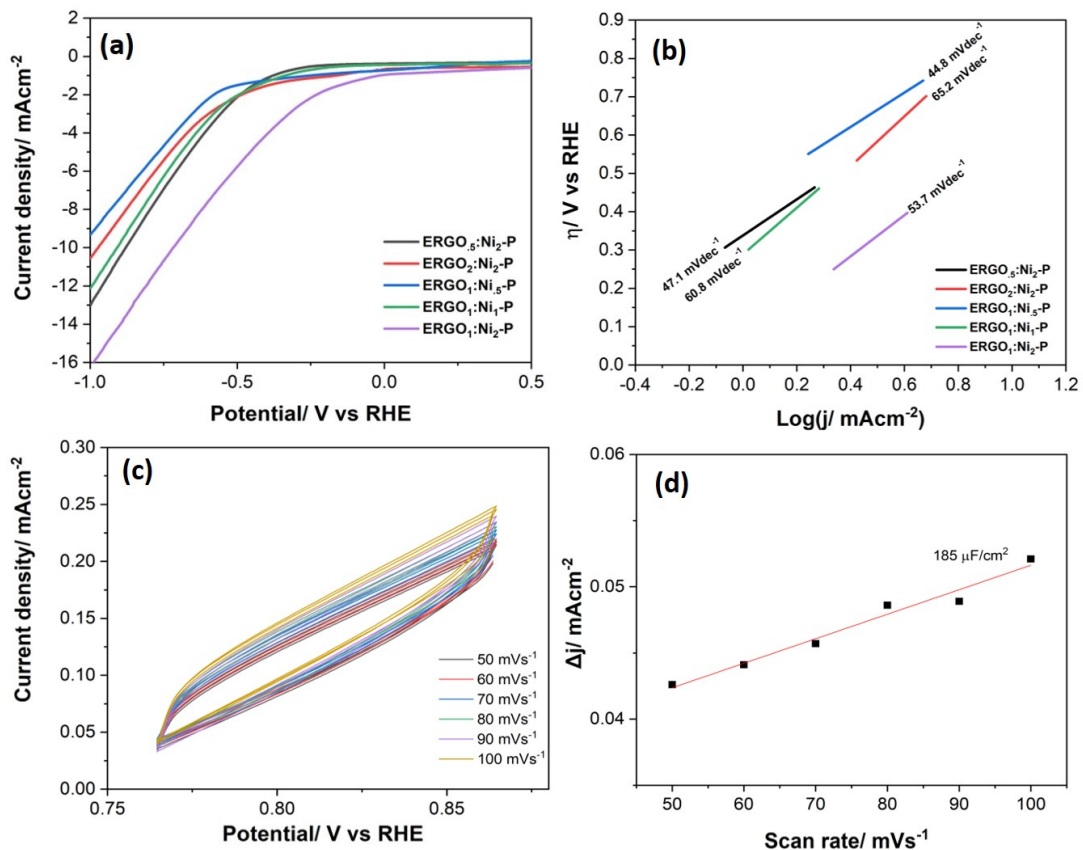


Figure 3.20: (a) Polarization curves of ERGO₁:Ni₅-P, ERGO₁:Ni₁-P, ERGO₁:Ni₂-P, ERGO₅:Ni₂-P and ERGO₂:Ni₂-P in 0.1 M KOH at scan rate of 1 mV s^{-1} (b) Tafel plot of same composites showing Tafel slope (c) CV curves in double layer region at scan rates of 50, 60, 70, 80, 90 and 100 mV s^{-1} of ERGO₁:Ni₂-P (d) The capacitive currents at 0.81 V as a function of scan rate for ERGO₁:Ni₂-P ($\Delta j = j_{\text{anodic}} - j_{\text{cathodic}}$)

evaluation of electrocatalyst as it is fundamentally built on the assumption that all nickel ions are active during HER and the method of calculating surface concentration is insufficient. ERGO₁:Ni₂-P showed magnificent stability after 6000s CA measurement and the amount of hydrogen produced was significantly large ($33 \text{ mmolh}^{-1} \text{ g}^{-1}$). (Figure A.1)

The evident increase in performance of composites upon reduction is most likely due to the fact that reduced graphene oxide is conductive hence, resulting in a faster and easier electron transfer. Moreover, the larger electroactive surface area of electrochemically reduced graphene oxide introduces more active sites that

can promote hydrogen evolution reaction.

3.3.4 The optimum sample

As shown in section 3.3, based on electrochemical activity and stability, the optimum sample composed of a layer of ERGO and a layer of Ni-P, with equal weight of GO and twice nickel acetate with respect to CB[8]-porphyrin. Thus, the electrochemical activity of this composite was further explored. Initially, the effect of nickel, GO, number of layers were studied separately (3.3.4.1) then electrochemical impedance responses were investigated (3.3.4.2) and finally, the activity of ERGO₁:Ni₂-P was analyzed in other mediums (3.3.4.3). In section 3.3.4.3, ERGO₁:Ni₂-P was deeply examined in 1 M KOH medium where it displayed the leading activity with a very low onset, producing a large amount of hydrogen per hour per gram.

3.3.4.1 Effect of GO, Nickel and number of layers

Figure 3.21a portrays the effect of adding nickel salt and graphene oxide separately. It was noted that the presence of nickel salt in the composite, reduces the onset potential and increases the stability for the optimum sample. The composite containing no nickel salt degraded slowly into the electrolyte and ultimately peeled off the FTO. This could be due to the high conductivity of nickel and its ability to act as a metal linker between porphyrin and ERGO, preventing repulsion between the layers. Similarly, graphene oxide enhanced the catalytic activity by around 40% which could be seen by the comparing $\eta@10\text{mAcm}^{-2}$.

The effect of varying the number of layers was also examined for ERGO₁: Ni₂-P in 0.1 M KOH (Figure 3.21b). This was done by alternating deposition of a layer of graphene oxide followed by a layer of Ni-P. Increasing the number of layers lead to a very small change in the performance while ERGO₁: Ni₂-P (one layer) remained with the lowest onset potential, consequently no further investigations have been made on varying the number of layers.

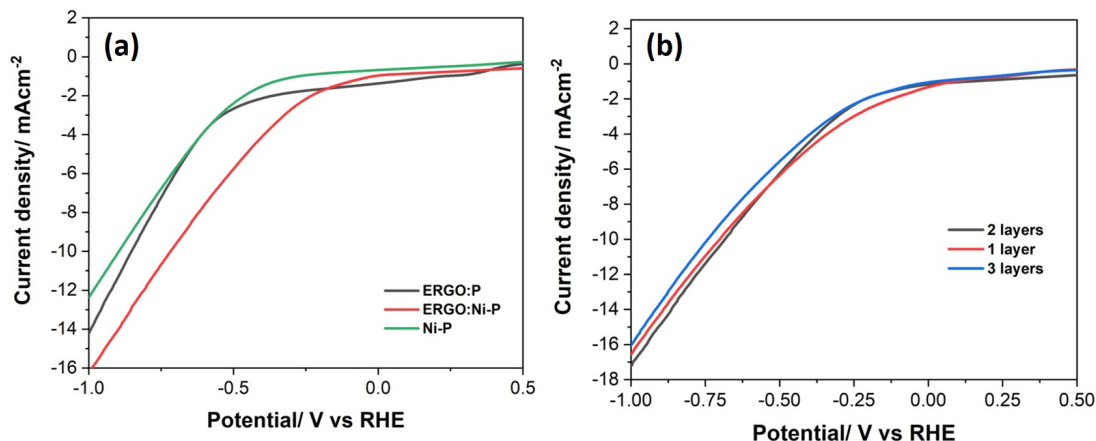


Figure 3.21: (a) Polarization curves showing the effect of adding GO and nickel separately (b) Polarization curve showing the effect of number of layers on ERGO₁:Ni₂-P in 0.1 M KOH

3.3.4.2 Electrochemical Impedance Spectroscopy

To gain further insight into the electrocatalytic activity of ERGO₁: Ni₂-P for HER, electrochemical impedance spectroscopy (EIS) measurements were carried out from 0.1 Hz to 100 kHz. The impedance response of ERGO₁: Ni₂-P can be expressed by an electrical circuit having two capacitance (Q_1 , Q_2) and two resistance (R_1 , R_2) placed in parallel (Figure 3.24). These circuit elements are associated with the high (Q_1 , R_1) and the low frequency (Q_2 , R_2) capacitive loops, respectively.[91] Figure 3.22a,b shows the Nyquist plot and bode plot for the ERGO₁: Ni₂-P in 0.1 M KOH. Both Nyquist and bode plots show two semi-circles; with the first being negligible in comparison to the one at low frequency. The first semicircle, which is associated with hydrogen adsorption, presented a resistance (R_1) of 60 Ω (diameter) while the diameter of second semicircle, which is related to the resistance to the HER kinetics, was found to be around 1000 Ω . Therefore, the total charge-transfer resistance (R_{ct}) is simply the sum of both resistances, in this case it was about 1060 Ω . The resistance R_s represents the uncompensated solution resistance, which was around 50 Ω in 0.1 M KOH. Furthermore, the absence of a Warburg impedance implies a fast-ionic transportation and a kinetically controlled electrochemical reaction.

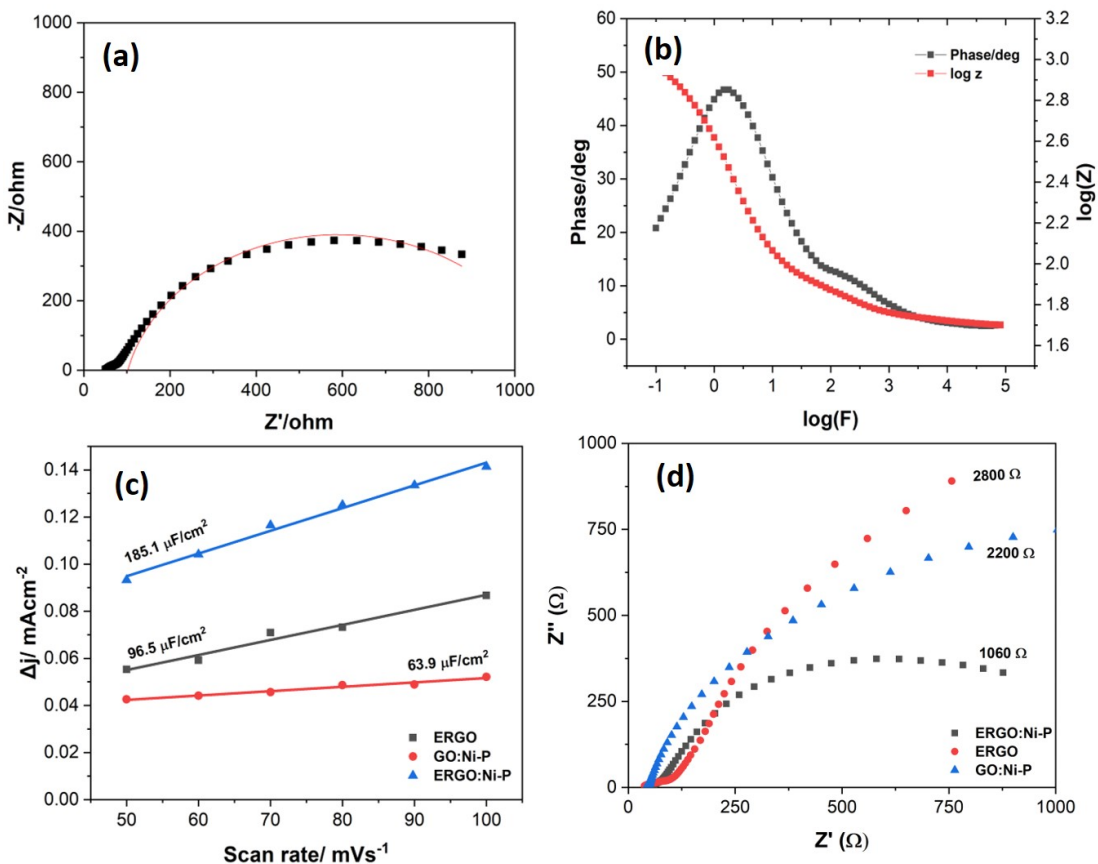


Figure 3.22: (a) Impedance spectra of ERGO₁: Ni₂-P in 0.1 M KOH solution at different applied overpotentials. The inset shows the equivalent circuit (b) Bode plot of ERGO₁: Ni₂-P showing phase and impedance (c) The capacitive currents at 0.81 V as a function of scan rate ($\Delta j = j_a - j_c$) and (d) Impedance spectra of ERGO, GO₁: Ni₂-P and ERGO₁: Ni₂-P modified FTO electrode in 0.1 M KOH.

Furthermore, the charge transfer resistance of ERGO and GO: Ni-P in 0.1 M KOH were found to be 2800 and 2200 Ω respectively (Figure 3.22d). The presence of only one semicircle in GO: Ni-P (0.1 M KOH) on the other hand, suggests a simple impedance response equivalent electrical circuit with only one resistance element (R_1) inside the loop.

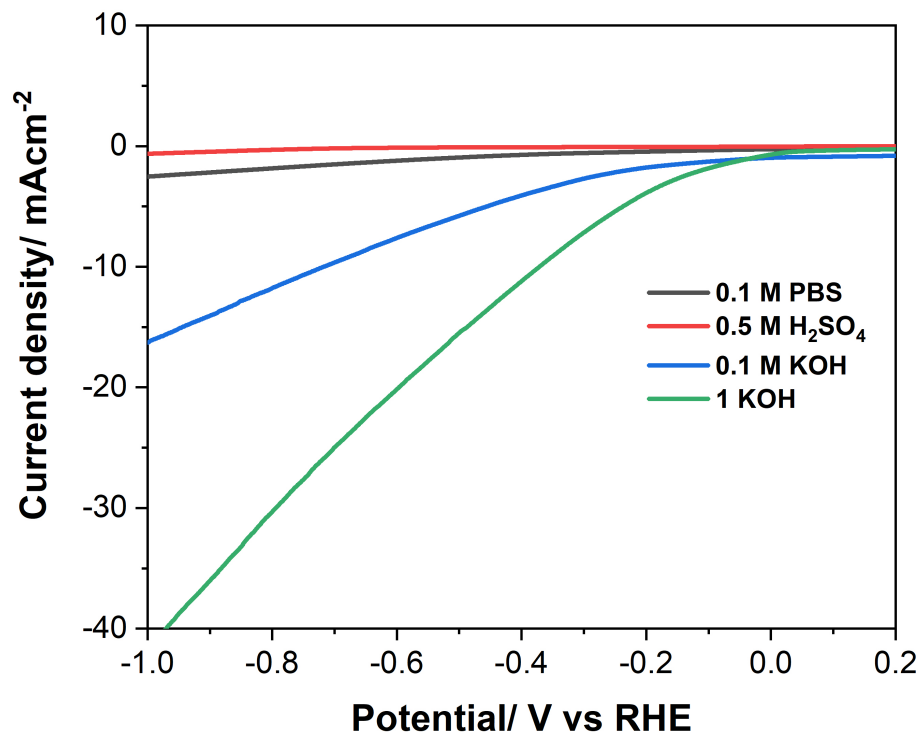


Figure 3.23: Polarization curves for ERGO₁:Ni₂-P in acidic, neutral and basic mediums

3.3.4.3 Optimum sample and electrolyte medium

The electrochemical activity of ERGO₁: Ni₂-P was further investigated in 0.5 M H₂SO₄, 0.1 M PBS and 1 M KOH (Figure 3.23). As predicted, the composite presented negligible performance in acidic and neutral mediums, however its activity was considerable in 1 M KOH. The onset (-20 mV) and $\eta@10\text{mAcm}^{-2}$ (-360mV) potentials were tremendously lower than in all other mediums. Table 3.9 displays the electrochemical parameters comparing both mediums. The exchange current density was also found to be remarkably high (1.14 mAcm⁻²) and the Tafel slope (41.3 mVdec⁻¹) indicated that HER reaction is through Heyrovsky mechanism.

The durability of the electrocatalytic system in 1 M KOH was studied by conducting a chronoamperometry test at -1.2 V vs Ag/AgCl for 12000 seconds as

shown in Figure 3.25c. The polarization curves of ERGO₁: Ni₂-P before and after CA (Figure 3.25d) were comparable, with a minor negative shift of 45 mV at 10 mAcm⁻², signifying its reasonable stability in 1 M KOH. This was also confirmed by SEM images and XPS analysis. ERGO₁: Ni₂-P displayed insignificant change in morphology and elemental (Figure 3.13,3.14).

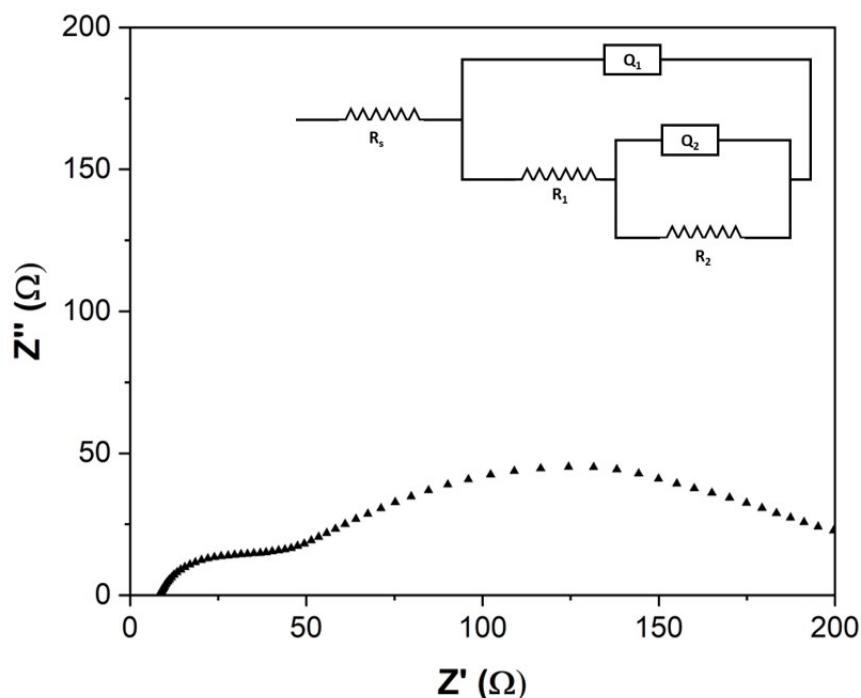


Figure 3.24: Impedance spectra of ERGO₁: Ni₂-P-modified FTO in 1 M KOH. The inset shows the equivalent circuit

Moreover, C_{dl} of ERGO₁: Ni₂-P in 1 M KOH was found to be even more noteworthy (1.67 mFcm⁻²) than in 0.1 M KOH implying better electrocatalytic activity (Figure 3.25b). Table 3.9 Electrochemical parameters for ERGO₁: Ni₂-P in 1 M KOH. As shown in Table 3.9, the amount hydrogen (in mmolh⁻¹g⁻¹) produced in 1 M KOH was almost 1.7 times the amount produced in a dilute basic medium. The impedance spectra in 1 M KOH was also studied (Figure 3.24). The resistance due to hydrogen adsorption on electrode (R_1) was found to be 40 Ω while the second resistance (R_2), which is associated with HER kinetics, was around 170 Ω . Therefore, the resulting total charge-transfer resistance (R_{ct}) (210 Ω) was substantially lower than in 0.1 M KOH confirming the faster kinetics. The

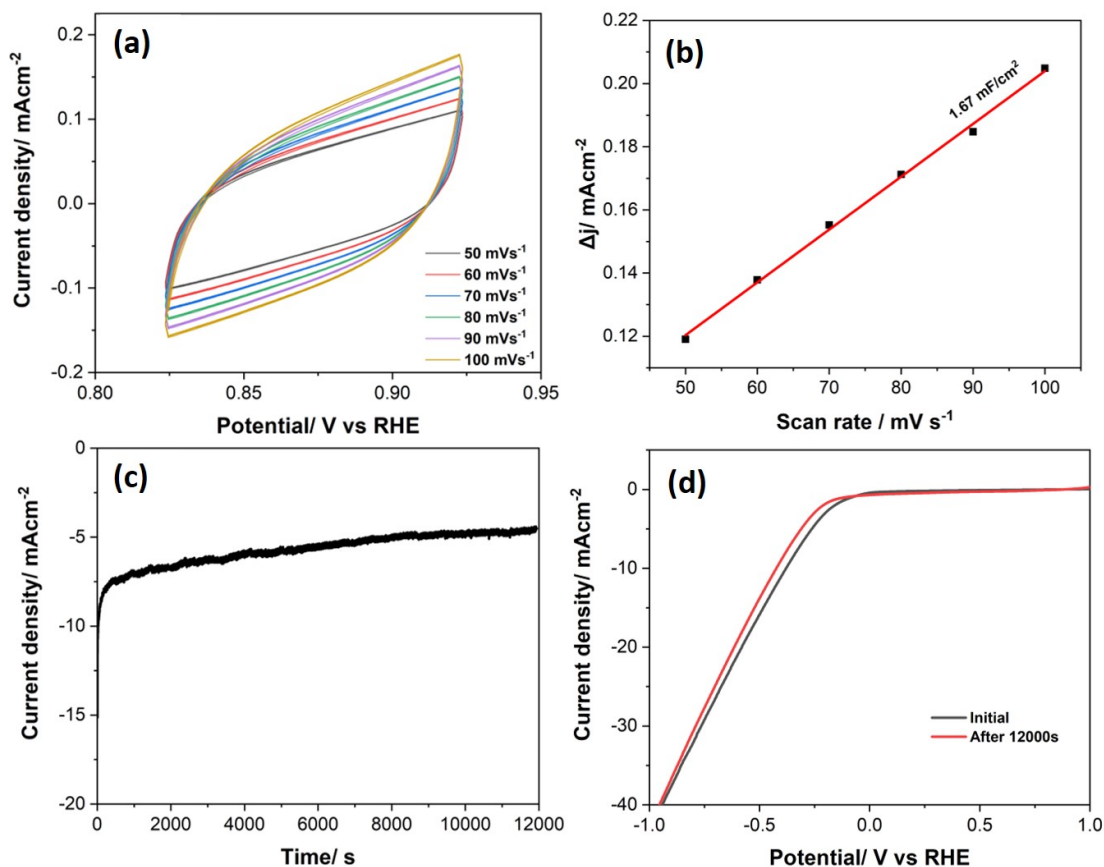


Figure 3.25: (a) CV curves in non-faradaic region at scan rates from 50 to 100 mV/s for ERGO1: Ni₂-P in 1 M KOH (b) The capacitive currents at 0.81 V as a function of scan rate ($\Delta=j_a-j_c$) (c) Chronoamperometry at -1.2 V vs RHE in 1 M KOH for 12000 seconds (d) Polarization curves of ERGO1: Ni₂-P initially and after 12000 seconds chronoamperometry test at -1.2 V vs Ag/AgCl in 1 M KOH.

solution resistance was also much smaller than in 0.1 M KOH (15 Ω). Furthermore, faradaic efficiency (93%) and TOF (0.351 s⁻¹) were clearly enhanced in 1 M KOH.

The optimum sample in this study exhibited better electrocatalytic activity than similar studies using porphyrin for hydrogen evolution reaction. While Huang et.al reported a layer by layer based electrocatalyst ([ERGO@CoTMPyP]₇) with $j@500\text{ mV} = -1.729\text{ mAcm}^{-2}$, charge transfer resistance of 283Ω and a Tafel slope of 116 mVdec⁻¹ [92], Ma et.al synthesized CoTMPyP/ERGO composite with charge transfer resistance of 312.6 Ω, $\eta@1\text{ mAcm}^{-2}$ of -315 mV and Tafel slope of -96 mVdec⁻¹ [91]. This study on the other hand, introduced much more significant parameters with larger current density

Table 3.9: Electrochemical parameter for ERGO1: Ni₂-P in 0.1 and 1 M KOH

	0.1 M KOH	1 M KOH
Onset /mV vs RHE	-30	-20
$\eta@10\text{mAcm}^{-2}$ /mV	-717	-360
Tafel slope /mVdec⁻¹	53.7	41.3
Exchange current density /mAcm⁻²	0.745	1.14
Faradaic efficiency	86.7	93.6
Amount of H₂ produced /mmol h⁻¹g⁻¹	33	56.9
C_{dl} / mFcm⁻²	0.185	1.67
TOF	0.0868	0.351

and lower overpotential values ($j@500\text{ mV} = -15.9\text{ mAcm}^{-2}$ and $\eta@1\text{ mAcm}^{-2} = -82.4\text{ mV}$). Furthermore, the charge transfer resistance and Tafel slope values were also much lower than analogous studies ($R_{ct} = 210\ \Omega$, $b = 40\text{ mVdec}^{-1}$).

All in all, nickel CB[8]-porphyrin composite functionalized on reduced graphene oxide sheets has been proven as a proficient HER catalyst in basic medium. Its efficacy however, was much more significant in 1 M KOH. It exhibited an excellent electrocatalytic activity even after long chronoamperometry measurements. A small Tafel slope of 41.3 mV dec^{-1} indicated a Heyrovsky mechanism while a large exchange current density (1.14 mA cm^{-2}) and a low charge transfer resistance ($210\ \Omega$) specified a fast reaction. It is foreseen that this work may introduce a facile path to design a wide range of low-cost and high-performance organic entities for HER. The excellent catalytic performance of ERGO₁: Ni₂-P arises from the strong electrostatic interaction between positively charge nickel CB[8] porphyrin assembly and negatively charged reduced graphene oxide as well as π - π interactions between the two entities that facilitates the flow of electrons. Moreover, the good conductivity of reduced graphene oxide's and the random porous structure of Ni-P inside ERGO sheets, accelerates charge transfer hence increases hydrogen production efficiency.

Chapter 4

CONCLUSION

In conclusion, this work focuses on the application of a conjugated polymer framework functionalized on electrochemically reduced graphene oxide in electrochemical hydrogen production. Firstly, the electrocatalytic activity of nickel porphyrin samples were examined in acidic, neutral and basic mediums using half, equal and double the weight of nickel salt with respect to porphyrin assembly. The electrocatalytic activities of all samples were evaluated using potentiometry, cyclic voltammetry, chronoamperometry and electrochemical impedance spectroscopy. The most efficient composite composed of double weight of nickel acetate (Ni₂-P) with an onset and $\eta@10\text{mAcm}^{-2}$ potentials of -253 and -894 mV respectively. The amount of hydrogen produced was calculated using current density in chronoamperometry and was found to be $23.4\text{ mmolh}^{-1}\text{g}^{-1}$. The double layer capacitance was derived from capacitive currents in CV, for Ni₂-P C_{dl} was $21.8\ \mu\text{Fcm}^{-2}$.

The second section involves incorporating graphene oxide into the composite. This was achieved in two distinct methods, mechanically adding it to the composite (all in one ink) or by dropcasting a layer GO dispersions first on FTO followed by introducing Ni-P composite (layers). Using a layer of GO then a layer of nickel porphyrin composite was found to be much more effective. Not only do the onset and $\eta@10\text{mAcm}^{-2}$ potentials dropped (-145 and -879 mV) by the addition of GO layer, but the double layer capacitance, hence electroactive surface area,

increased by 2.7 times and so did the efficiency for hydrogen production ($24.6 \text{ mmolh}^{-1}\text{g}^{-1}$) at an even smaller overpotential.

The activities of the composites were further examined by electrochemically reducing graphene oxide via cyclic voltammetry 0.1 M PBS. A large cathodic peak appeared in the first cycle that confirmed irreversible reduction. The composites synthesized by layering again resulted in most superior results, with low onset and $\eta@10\text{mAcm}^{-2}$ potentials (-30 and -717 mV) and extremely high C_{dl} and exchange current density (0.745 mAcm^{-2}). Therefore, the results confirm that reducing GO results in a larger electroactive surface area as well as a faster HER. This prime composite was tested in 0.5 M H_2SO_4 , 0.1 M PBS and 1 M KOH. Its activity was found to be exceptional in 1 M KOH, with extremely low overpotentials, highly significant exchange current density and C_{dl} values. This composite portrayed excellent durability throughout 3h CA measurement with negligible change in activity and morphologies. Electrochemical impedance studies revealed a charge transfer resistance of 210 which is almost one fifth of one calculated for same composite in 0.1 M KOH.

Finally, characterization techniques were utilized to examine the topology and morphology of composite and to approve electrochemical reduction of GO. SEM images of GO and ERGO showed randomly wrinkled sheets with ERGO having rougher surface. ERGO: Ni-P displayed micro voids owing to porphyrin units and at low magnification, ERGO sheets were observed. The reduction of GO was endorsed by XPS analysis that proved drastic decline in intensities of oxygen rich functional groups. The interlayer spacings were derived from XRD patterns. The d-spacing of GO (0.73 nm) was increased by introducing Ni-P (1.02 nm). FT-IR and Raman analysis were also embedded to examine the bonding and vibrational behavior of GO, ERGO and ERGO: Ni-P.

To sum up, nickel porphyrin composite functionalized on reduced graphene oxide sheets (ERGO₁:Ni₂-P) has been proven as a proficient HER catalyst in 1 M KOH. It is hoped that this work would introduce a facile path to design a wide range of low-cost and high-performance organic entities for HER.

Bibliography

- [1] L. Zyga, “How a solar-hydrogen economy could supply the world’s energy needs,” *Phys.org*, 2009.
- [2] J. Töpler, “Hydrogen as energy-storage-medium and fuel-a strong partner of renewable energies,” *Renewable Energy and Environmental Sustainability*, vol. 1, p. 31, 2016.
- [3] B. Rohland, J. Nitsch, and H. Wendt, “Hydrogen and fuel cells?the clean energy system,” *Journal of power sources*, vol. 37, no. 1-2, pp. 271–277, 1992.
- [4] S. Sharma and S. K. Ghoshal, “Hydrogen the future transportation fuel: From production to applications,” *Renewable and sustainable energy reviews*, vol. 43, pp. 1151–1158, 2015.
- [5] D. Das and T. N. Veziro?lu, “Hydrogen production by biological processes: a survey of literature,” *International journal of hydrogen energy*, vol. 26, no. 1, pp. 13–28, 2001.
- [6] N. Muradov and T. Veziro?lu, “From hydrocarbon to hydrogen–carbon to hydrogen economy,” *International journal of hydrogen energy*, vol. 30, no. 3, pp. 225–237, 2005.
- [7] M. Onozaki, K. Watanabe, T. Hashimoto, H. Saegusa, and Y. Katayama, “Hydrogen production by the partial oxidation and steam reforming of tar from hot coke oven gas,” *Fuel*, vol. 85, no. 2, pp. 143–149, 2006.

- [8] C. M. Kalamaras and A. M. Efstathiou, “Hydrogen production technologies: current state and future developments,” in *Conference papers in energy*, vol. 2013, Hindawi, 2013.
- [9] A. Adris, B. Pruden, C. Lim, and J. Grace, “On the reported attempts to radically improve the performance of the steam methane reforming reactor,” *The Canadian Journal of Chemical Engineering*, vol. 74, no. 2, pp. 177–186, 1996.
- [10] Y. Shirasaki, T. Tsuneki, Y. Ota, I. Yasuda, S. Tachibana, H. Nakajima, and K. Kobayashi, “Development of membrane reformer system for highly efficient hydrogen production from natural gas,” *International Journal of Hydrogen Energy*, vol. 34, no. 10, pp. 4482–4487, 2009.
- [11] S. E. Hosseini and M. A. Wahid, “Hydrogen production from renewable and sustainable energy resources: promising green energy carrier for clean development,” *Renewable and Sustainable Energy Reviews*, vol. 57, pp. 850–866, 2016.
- [12] S. E. Hosseini and M. A. Wahid, “Development of biogas combustion in combined heat and power generation,” *Renewable and Sustainable Energy Reviews*, vol. 40, pp. 868–875, 2014.
- [13] M. B. Charles, R. Ryan, R. Oloruntoba, T. von der Heidt, and N. Ryan, “The eu–africa energy partnership: towards a mutually beneficial renewable transport energy alliance?,” *Energy Policy*, vol. 37, no. 12, pp. 5546–5556, 2009.
- [14] M. Hoogwijk, A. Faaij, B. Eickhout, B. de Vries, and W. Turkenburg, “Potential of biomass energy out to 2100, for four ipcc sres land-use scenarios,” *Biomass and Bioenergy*, vol. 29, no. 4, pp. 225–257, 2005.
- [15] T. A. Milne, C. C. Elam, and R. J. Evans, “Hydrogen from biomass: state of the art and research challenges,” tech. rep., National Renewable Energy Lab., Golden, CO (US), 2002.

- [16] M. F. Demirbas, “Hydrogen from various biomass species via pyrolysis and steam gasification processes,” *Energy Sources, Part A*, vol. 28, no. 3, pp. 245–252, 2006.
- [17] M. Asadullah, S.-i. Ito, K. Kunimori, M. Yamada, and K. Tomishige, “Energy efficient production of hydrogen and syngas from biomass: development of low-temperature catalytic process for cellulose gasification,” *Environmental science & technology*, vol. 36, no. 20, pp. 4476–4481, 2002.
- [18] M. Ni, D. Y. Leung, M. K. Leung, and K. Sumathy, “An overview of hydrogen production from biomass,” *Fuel processing technology*, vol. 87, no. 5, pp. 461–472, 2006.
- [19] R. Jalan and V. Srivastava, “Studies on pyrolysis of a single biomass cylindrical pellet?kinetic and heat transfer effects,” *Energy Conversion and Management*, vol. 40, no. 5, pp. 467–494, 1999.
- [20] A. Demirbaş, “Gaseous products from biomass by pyrolysis and gasification: effects of catalyst on hydrogen yield,” *Energy conversion and management*, vol. 43, no. 7, pp. 897–909, 2002.
- [21] N. Chouhan, R.-S. Liu, and J. Zhang, *Photochemical Water Splitting: Materials and Applications*. CRC Press, 2017.
- [22] J. D. Holladay, J. Hu, D. L. King, and Y. Wang, “An overview of hydrogen production technologies,” *Catalysis today*, vol. 139, no. 4, pp. 244–260, 2009.
- [23] A. E. Outlook *et al.*, “Energy information administration,” *Department of Energy*, vol. 92010, no. 9, pp. 1–15, 2010.
- [24] M. E. Lyons and S. Floquet, “Mechanism of oxygen reactions at porous oxide electrodes. part 2?oxygen evolution at ruo2, icro2 and irxru1- xo2 electrodes in aqueous acid and alkaline solution,” *Physical Chemistry Chemical Physics*, vol. 13, no. 12, pp. 5314–5335, 2011.

- [25] Z. Wei, M. Ji, S. Chen, Y. Liu, C. Sun, G. Yin, P. Shen, and S. Chan, “Water electrolysis on carbon electrodes enhanced by surfactant,” *Electrochimica Acta*, vol. 52, no. 9, pp. 3323–3329, 2007.
- [26] D. Tsiplakides, “Pem water electrolysis fundamentals,” *Available from:[cited 2013 August]*, 2012.
- [27] N. Nagai, M. Takeuchi, T. Kimura, and T. Oka, “Existence of optimum space between electrodes on hydrogen production by water electrolysis,” *International journal of hydrogen energy*, vol. 28, no. 1, pp. 35–41, 2003.
- [28] W. Kreuter and H. Hofmann, “Electrolysis: the important energy transformer in a world of sustainable energy,” *International Journal of Hydrogen Energy*, vol. 23, no. 8, pp. 661–666, 1998.
- [29] K. Kinoshita and P. Stonehart, “Modern aspects of electrochemistry,” *Plenum Press, New York*, 1977.
- [30] K. Zeng and D. Zhang, “Recent progress in alkaline water electrolysis for hydrogen production and applications,” *Progress in energy and combustion science*, vol. 36, no. 3, pp. 307–326, 2010.
- [31] Z. Chen, D. Higgins, A. Yu, L. Zhang, and J. Zhang, “A review on non-precious metal electrocatalysts for pem fuel cells,” *Energy & Environmental Science*, vol. 4, no. 9, pp. 3167–3192, 2011.
- [32] V. Vij, S. Sultan, A. M. Harzandi, A. Meena, J. N. Tiwari, W.-G. Lee, T. Yoon, and K. S. Kim, “Nickel-based electrocatalysts for energy-related applications: oxygen reduction, oxygen evolution, and hydrogen evolution reactions,” *Acs Catalysis*, vol. 7, no. 10, pp. 7196–7225, 2017.
- [33] V. Vij, S. Sultan, A. M. Harzandi, A. Meena, J. N. Tiwari, W.-G. Lee, T. Yoon, and K. S. Kim, “Nickel-based electrocatalysts for energy-related applications: oxygen reduction, oxygen evolution, and hydrogen evolution reactions,” *Acs Catalysis*, vol. 7, no. 10, pp. 7196–7225, 2017.

- [34] M. Gong, W. Zhou, M.-C. Tsai, J. Zhou, M. Guan, M.-C. Lin, B. Zhang, Y. Hu, D.-Y. Wang, J. Yang, *et al.*, “Nanoscale nickel oxide/nickel heterostructures for active hydrogen evolution electrocatalysis,” *Nature communications*, vol. 5, no. 1, pp. 1–6, 2014.
- [35] Y. Zheng, Y. Jiao, Y. Zhu, L. H. Li, Y. Han, Y. Chen, A. Du, M. Jaroniec, and S. Z. Qiao, “Hydrogen evolution by a metal-free electrocatalyst,” *Nature communications*, vol. 5, no. 1, pp. 1–8, 2014.
- [36] M. J. Allen, V. C. Tung, and R. B. Kaner, “Honeycomb carbon: a review of graphene,” *Chemical reviews*, vol. 110, no. 1, pp. 132–145, 2010.
- [37] K. S. Novoselov, A. K. Geim, S. V. Morozov, D. Jiang, Y. Zhang, S. V. Dubonos, I. V. Grigorieva, and A. A. Firsov, “Electric field effect in atomically thin carbon films,” *science*, vol. 306, no. 5696, pp. 666–669, 2004.
- [38] M. Hirata, T. Gotou, S. Horiuchi, M. Fujiwara, and M. Ohba, “Thin-film particles of graphite oxide 1:: High-yield synthesis and flexibility of the particles,” *Carbon*, vol. 42, no. 14, pp. 2929–2937, 2004.
- [39] M. Hirata, T. Gotou, and M. Ohba, “Thin-film particles of graphite oxide. 2: Preliminary studies for internal micro fabrication of single particle and carbonaceous electronic circuits,” *Carbon*, vol. 43, no. 3, pp. 503–510, 2005.
- [40] S. Stankovich, D. A. Dikin, G. H. Dommett, K. M. Kohlhaas, E. J. Zimney, E. A. Stach, R. D. Piner, S. T. Nguyen, and R. S. Ruoff, “Graphene-based composite materials,” *nature*, vol. 442, no. 7100, pp. 282–286, 2006.
- [41] J. Filip and J. Tkac, “Is graphene worth using in biofuel cells?,” *Electrochimica Acta*, vol. 136, pp. 340–354, 2014.
- [42] Y. Sun, Q. Wu, and G. Shi, “Graphene based new energy materials,” *Energy & Environmental Science*, vol. 4, no. 4, pp. 1113–1132, 2011.
- [43] C. e. e. Rao, A. e. Sood, K. e. Subrahmanyam, and A. Govindaraj, “Graphene: the new two-dimensional nanomaterial,” *Angewandte Chemie International Edition*, vol. 48, no. 42, pp. 7752–7777, 2009.

- [44] K. S. Kim, Y. Zhao, H. Jang, S. Y. Lee, J. M. Kim, K. S. Kim, J.-H. Ahn, P. Kim, J.-Y. Choi, and B. H. Hong, “Large-scale pattern growth of graphene films for stretchable transparent electrodes,” *nature*, vol. 457, no. 7230, pp. 706–710, 2009.
- [45] S. Park and R. S. Ruoff, “Chemical methods for the production of graphenes,” *Nature nanotechnology*, vol. 4, no. 4, pp. 217–224, 2009.
- [46] G. Shao, Y. Lu, F. Wu, C. Yang, F. Zeng, and Q. Wu, “Graphene oxide: the mechanisms of oxidation and exfoliation,” *Journal of materials science*, vol. 47, no. 10, pp. 4400–4409, 2012.
- [47] Y. Si and E. T. Samulski, “Synthesis of water soluble graphene,” *Nano letters*, vol. 8, no. 6, pp. 1679–1682, 2008.
- [48] S. Pei and H.-M. Cheng, “The reduction of graphene oxide,” *Carbon*, vol. 50, no. 9, pp. 3210–3228, 2012.
- [49] S. Stankovich, D. A. Dikin, R. D. Piner, K. A. Kohlhaas, A. Kleinhammes, Y. Jia, Y. Wu, S. T. Nguyen, and R. S. Ruoff, “Synthesis of graphene-based nanosheets via chemical reduction of exfoliated graphite oxide,” *carbon*, vol. 45, no. 7, pp. 1558–1565, 2007.
- [50] M. J. McAllister, J.-L. Li, D. H. Adamson, H. C. Schniepp, A. A. Abdala, J. Liu, M. Herrera-Alonso, D. L. Milius, R. Car, R. K. Prud’homme, *et al.*, “Single sheet functionalized graphene by oxidation and thermal expansion of graphite,” *Chemistry of materials*, vol. 19, no. 18, pp. 4396–4404, 2007.
- [51] Z.-S. Wu, W. Ren, L. Gao, J. Zhao, Z. Chen, B. Liu, D. Tang, B. Yu, C. Jiang, and H.-M. Cheng, “Synthesis of graphene sheets with high electrical conductivity and good thermal stability by hydrogen arc discharge exfoliation,” *ACS nano*, vol. 3, no. 2, pp. 411–417, 2009.
- [52] S. Stankovich, D. A. Dikin, G. H. Dommett, K. M. Kohlhaas, E. J. Zimney, E. A. Stach, R. D. Piner, S. T. Nguyen, and R. S. Ruoff, “Graphene-based composite materials,” *nature*, vol. 442, no. 7100, pp. 282–286, 2006.

- [53] M. J. Fernandez-Merino, L. Guardia, J. Paredes, S. Villar-Rodil, P. Solis-Fernandez, A. Martinez-Alonso, and J. Tascón, “Vitamin c is an ideal substitute for hydrazine in the reduction of graphene oxide suspensions,” *The Journal of Physical Chemistry C*, vol. 114, no. 14, pp. 6426–6432, 2010.
- [54] G. Williams, B. Seger, and P. V. Kamat, “TiO₂-graphene nanocomposites. uv-assisted photocatalytic reduction of graphene oxide,” *ACS nano*, vol. 2, no. 7, pp. 1487–1491, 2008.
- [55] M. Zhou, Y. Wang, Y. Zhai, J. Zhai, W. Ren, F. Wang, and S. Dong, “Controlled synthesis of large-area and patterned electrochemically reduced graphene oxide films,” *Chemistry—A European Journal*, vol. 15, no. 25, pp. 6116–6120, 2009.
- [56] H.-L. Guo, X.-F. Wang, Q.-Y. Qian, F.-B. Wang, and X.-H. Xia, “A green approach to the synthesis of graphene nanosheets,” *ACS nano*, vol. 3, no. 9, pp. 2653–2659, 2009.
- [57] M. A. Raj and S. A. John, “Fabrication of electrochemically reduced graphene oxide films on glassy carbon electrode by self-assembly method and their electrocatalytic application,” *The Journal of Physical Chemistry C*, vol. 117, no. 8, pp. 4326–4335, 2013.
- [58] I. V. Lightcap, T. H. Kosel, and P. V. Kamat, “Anchoring semiconductor and metal nanoparticles on a two-dimensional catalyst mat. storing and shuttling electrons with reduced graphene oxide,” *Nano letters*, vol. 10, no. 2, pp. 577–583, 2010.
- [59] S. Y. Toh, K. S. Loh, S. K. Kamarudin, and W. R. W. Daud, “Graphene production via electrochemical reduction of graphene oxide: synthesis and characterisation,” *Chemical Engineering Journal*, vol. 251, pp. 422–434, 2014.
- [60] H. Ö. Doğan, D. Ekinçi, and Ü. Demir, “Atomic scale imaging and spectroscopic characterization of electrochemically reduced graphene oxide,” *Surface science*, vol. 611, pp. 54–59, 2013.

- [61] Y. Shao, J. Wang, M. Engelhard, C. Wang, and Y. Lin, “Facile and controllable electrochemical reduction of graphene oxide and its applications,” *Journal of Materials Chemistry*, vol. 20, no. 4, pp. 743–748, 2010.
- [62] K. M. Smith, *Porphyrins and metalloporphyrins*, vol. 9. Elsevier Amsterdam, 1975.
- [63] L. Zang, Y. Che, and J. S. Moore, “One-dimensional self-assembly of planar π -conjugated molecules: adaptable building blocks for organic nanodevices,” *Accounts of chemical research*, vol. 41, no. 12, pp. 1596–1608, 2008.
- [64] Y. S. Zhao, H. Fu, A. Peng, Y. Ma, D. Xiao, and J. Yao, “Low-dimensional nanomaterials based on small organic molecules: Preparation and optoelectronic properties,” *Advanced Materials*, vol. 20, no. 15, pp. 2859–2876, 2008.
- [65] Y. Chen, A. Li, Z.-H. Huang, L.-N. Wang, and F. Kang, “Porphyrin-based nanostructures for photocatalytic applications,” *Nanomaterials*, vol. 6, no. 3, p. 51, 2016.
- [66] T. Hasobe, “Porphyrin-based supramolecular nanoarchitectures for solar energy conversion,” *The journal of physical chemistry letters*, vol. 4, no. 11, pp. 1771–1780, 2013.
- [67] I. Bhugun, D. Lexa, and J.-M. Savéant, “Homogeneous catalysis of electrochemical hydrogen evolution by iron (0) porphyrins,” *Journal of the American Chemical Society*, vol. 118, no. 16, pp. 3982–3983, 1996.
- [68] S. Aronoff, “Perchloric acid titrations of porphyrins in nitrobenzene,” *The Journal of Physical Chemistry*, vol. 62, no. 4, pp. 428–431, 1958.
- [69] Y. Wu, N. Rodríguez-López, and D. Villagrán, “Hydrogen gas generation using a metal-free fluorinated porphyrin,” *Chemical science*, vol. 9, no. 20, pp. 4689–4695, 2018.
- [70] A. Koc and D. Tuncel, “Supramolecular assemblies of cucurbiturils with photoactive, π -conjugated chromophores,” *Israel Journal of Chemistry*, vol. 58, no. 3-4, pp. 334–342, 2018.

- [71] X. Wang, C. Liow, D. Qi, B. Zhu, W. R. Leow, H. Wang, C. Xue, X. Chen, and S. Li, "Programmable photo-electrochemical hydrogen evolution based on multi-segmented cds-au nanorod arrays," *Advanced materials*, vol. 26, no. 21, pp. 3506–3512, 2014.
- [72] D.-J. Qian, S.-O. Wenk, C. Nakamura, T. Wakayama, N. Zorin, and J. Miyake, "Photoinduced hydrogen evolution by use of porphyrin, edta, viologens and hydrogenase in solutions and langmuir–blodgett films," *International journal of hydrogen energy*, vol. 27, no. 11-12, pp. 1481–1487, 2002.
- [73] T. Lazarides, M. Delor, I. V. Sazanovich, T. M. McCormick, I. Georgakaki, G. Charalambidis, J. A. Weinstein, and A. G. Coutsolelos, "Photocatalytic hydrogen production from a noble metal free system based on a water soluble porphyrin derivative and a cobaloxime catalyst," *Chemical Communications*, vol. 50, no. 5, pp. 521–523, 2014.
- [74] Y. Kumar, B. Patil, A. Khaligh, S. E. Hadi, T. Uyar, and D. Tuncel, "Novel supramolecular photocatalyst based on conjugation of cucurbit [7] uril to non-metallated porphyrin for electrophotocatalytic hydrogen generation from water splitting," *ChemCatChem*, vol. 11, no. 13, pp. 2940–2940, 2019.
- [75] T. Nakazono, A. R. Parent, and K. Sakai, "Cobalt porphyrins as homogeneous catalysts for water oxidation," *Chemical Communications*, vol. 49, no. 56, pp. 6325–6327, 2013.
- [76] S. J. Barrow, S. Kasera, M. J. Rowland, J. del Barrio, and O. A. Scherman, "Cucurbituril-based molecular recognition," *Chemical reviews*, vol. 115, no. 22, pp. 12320–12406, 2015.
- [77] S. Gürbüz, M. Idris, and D. Tuncel, "Cucurbituril-based supramolecular engineered nanostructured materials," *Organic & biomolecular chemistry*, vol. 13, no. 2, pp. 330–347, 2015.
- [78] J. Kim, I.-S. Jung, S.-Y. Kim, E. Lee, J.-K. Kang, S. Sakamoto, K. Yamaguchi, and K. Kim, "New cucurbituril homologues: syntheses, isolation,

- characterization, and x-ray crystal structures of cucurbit [n] uril (n= 5, 7, and 8),” *Journal of the American Chemical Society*, vol. 122, no. 3, pp. 540–541, 2000.
- [79] A. Day, A. P. Arnold, R. J. Blanch, and B. Snushall, “Controlling factors in the synthesis of cucurbituril and its homologues,” *The Journal of organic chemistry*, vol. 66, no. 24, pp. 8094–8100, 2001.
- [80] A. I. Day, R. J. Blanch, A. P. Arnold, S. Lorenzo, G. R. Lewis, and I. Dance, “A cucurbituril-based gyroscone: a new supramolecular form,” *Angewandte Chemie*, vol. 114, no. 2, pp. 285–287, 2002.
- [81] S. Walker, R. Oun, F. J. McInnes, and N. J. Wheate, “The potential of cucurbit [n] urils in drug delivery,” *Israel Journal of Chemistry*, vol. 51, no. 5-6, pp. 616–624, 2011.
- [82] B. C. Pemberton, R. K. Singh, A. C. Johnson, S. Jockusch, J. P. Da Silva, A. Ugrinov, N. J. Turro, D. Srivastava, and J. Sivaguru, “Supramolecular photocatalysis: insights into cucurbit [8] uril catalyzed photodimerization of 6-methylcoumarin,” *Chemical Communications*, vol. 47, no. 22, pp. 6323–6325, 2011.
- [83] A. A. Elbashir and H. Y. Aboul-Enein, “Supramolecular analytical application of cucurbit [n] urils using fluorescence spectroscopy,” *Critical Reviews in Analytical Chemistry*, vol. 45, no. 1, pp. 52–61, 2015.
- [84] H. Li and Y.-W. Yang, “Gold nanoparticles functionalized with supramolecular macrocycles,” *Chinese Chemical Letters*, vol. 24, no. 7, pp. 545–552, 2013.
- [85] R. Ge, X. Li, S.-Z. Kang, L. Qin, and G. Li, “Highly efficient graphene oxide/porphyrin photocatalysts for hydrogen evolution and the interfacial electron transfer,” *Applied Catalysis B: Environmental*, vol. 187, pp. 67–74, 2016.
- [86] H. S. Han, H. K. Lee, J.-M. You, H. Jeong, and S. Jeon, “Electrochemical biosensor for simultaneous determination of dopamine and serotonin

- based on electrochemically reduced go-porphyrin,” *Sensors and Actuators B: Chemical*, vol. 190, pp. 886–895, 2014.
- [87] R. Bera, S. Mandal, B. Mondal, B. Jana, S. K. Nayak, and A. Patra, “Graphene–porphyrin nanorod composites for solar light harvesting,” *ACS Sustainable Chemistry & Engineering*, vol. 4, no. 3, pp. 1562–1568, 2016.
- [88] S. Su, J. Wang, J. Wei, R. Martínez-Zaguilán, J. Qiu, and S. Wang, “Efficient photothermal therapy of brain cancer through porphyrin functionalized graphene oxide,” *New Journal of Chemistry*, vol. 39, no. 7, pp. 5743–5749, 2015.
- [89] S. Zhang, S. Tang, J. Lei, H. Dong, and H. Ju, “Functionalization of graphene nanoribbons with porphyrin for electrocatalysis and amperometric biosensing,” *Journal of electroanalytical chemistry*, vol. 656, no. 1-2, pp. 285–288, 2011.
- [90] M. Wei, J. Wan, Z. Hu, Z. Peng, and B. Wang, “Enhanced photocatalytic degradation activity over tio2 nanotubes co-sensitized by reduced graphene oxide and copper (ii) meso-tetra (4-carboxyphenyl) porphyrin,” *Applied Surface Science*, vol. 377, pp. 149–158, 2016.
- [91] J. Ma, L. Liu, Q. Chen, M. Yang, D. Wang, Z. Tong, and Z. Chen, “A facile approach to prepare crumpled cotmpyp/electrochemically reduced graphene oxide nanohybrid as an efficient electrocatalyst for hydrogen evolution reaction,” *Applied Surface Science*, vol. 399, pp. 535–541, 2017.
- [92] D. Huang, J. Lu, S. Li, Y. Luo, C. Zhao, B. Hu, M. Wang, and Y. Shen, “Fabrication of cobalt porphyrin. electrochemically reduced graphene oxide hybrid films for electrocatalytic hydrogen evolution in aqueous solution,” *Langmuir*, vol. 30, no. 23, pp. 6990–6998, 2014.
- [93] Q. Luo, R. Ge, S.-Z. Kang, L. Qin, G. Li, and X. Li, “Fabrication mechanism and photocatalytic activity for a novel graphene oxide hybrid functionalized with tetrakis-(4-hydroxylphenyl) porphyrin and 1-pyrenesulfonic acid,” *Applied Surface Science*, vol. 427, pp. 15–23, 2018.

- [94] D. C. Marcano, D. V. Kosynkin, J. M. Berlin, A. Sinitskii, Z. Sun, A. Slesarev, L. B. Alemany, W. Lu, and J. M. Tour, "Improved synthesis of graphene oxide," *ACS nano*, vol. 4, no. 8, pp. 4806–4814, 2010.
- [95] S. Anantharaj, S. Ede, K. Karthick, S. S. Sankar, K. Sangeetha, P. Karthik, and S. Kundu, "Precision and correctness in the evaluation of electrocatalytic water splitting: revisiting activity parameters with a critical assessment," *Energy & Environmental Science*, vol. 11, no. 4, pp. 744–771, 2018.
- [96] M. de Rooij, "Electrochemical methods: Fundamentals and applications," *Anti-Corrosion Methods and Materials*, 2003.
- [97] S. Jayabal, G. Saranya, J. Wu, Y. Liu, D. Geng, and X. Meng, "Understanding the high-electrocatalytic performance of two-dimensional mos 2 nanosheets and their composite materials," *Journal of Materials Chemistry A*, vol. 5, no. 47, pp. 24540–24563, 2017.
- [98] N. Mahmood, Y. Yao, J.-W. Zhang, L. Pan, X. Zhang, and J.-J. Zou, "Electrocatalysts for hydrogen evolution in alkaline electrolytes: mechanisms, challenges, and prospective solutions," *Advanced science*, vol. 5, no. 2, p. 1700464, 2018.
- [99] Y. Shi and B. Zhang, "Recent advances in transition metal phosphide nanomaterials: synthesis and applications in hydrogen evolution reaction," *Chemical Society Reviews*, vol. 45, no. 6, pp. 1529–1541, 2016.
- [100] X. Bai, Q. Wang, G. Xu, Y. Ning, K. Huang, F. He, Z.-j. Wu, and J. Zhang, "Phosphorus and fluorine co-doping induced enhancement of oxygen evolution reaction in bimetallic nitride nanorods arrays: Ionic liquid-driven and mechanism clarification," *Chemistry—A European Journal*, vol. 23, no. 66, pp. 16862–16870, 2017.
- [101] D. C. Marcano, D. V. Kosynkin, J. M. Berlin, A. Sinitskii, Z. Sun, A. Slesarev, L. B. Alemany, W. Lu, and J. M. Tour, "Improved synthesis of graphene oxide," *ACS nano*, vol. 4, no. 8, pp. 4806–4814, 2010.

- [102] A. Koc, R. Khan, and D. Tuncel, ““clicked” porphyrin-cucurbituril conjugate: A new multifunctional supramolecular assembly based on triglycosylated porphyrin and monopropargyloxycucurbit [7] uril,” *Chemistry–A European Journal*, vol. 24, no. 58, pp. 15550–15555, 2018.
- [103] E. Masson, X. Ling, R. Joseph, L. Kyeremeh-Mensah, and X. Lu, “Cucurbituril chemistry: a tale of supramolecular success,” *Rsc Advances*, vol. 2, no. 4, pp. 1213–1247, 2012.
- [104] J. Lagona, P. Mukhopadhyay, S. Chakrabarti, and L. Isaacs, “Die cucurbit [n] uril-familie,” *Angewandte Chemie*, vol. 117, no. 31, pp. 4922–4949, 2005.
- [105] M. Wang, Q. Wang, W. Zhu, Y. Yang, H. Zhou, F. Zhang, L. Zhou, J. M. Razal, G. G. Wallace, and J. Chen, “Metal porphyrin intercalated reduced graphene oxide nanocomposite utilized for electrocatalytic oxygen reduction,” *Green Energy & Environment*, vol. 2, no. 3, pp. 285–293, 2017.
- [106] S. Y. Toh, K. S. Loh, S. K. Kamarudin, and W. R. W. Daud, “Graphene production via electrochemical reduction of graphene oxide: synthesis and characterisation,” *Chemical Engineering Journal*, vol. 251, pp. 422–434, 2014.
- [107] C. Liu, K. Wang, S. Luo, Y. Tang, and L. Chen, “Direct electrodeposition of graphene enabling the one-step synthesis of graphene–metal nanocomposite films,” *small*, vol. 7, no. 9, pp. 1203–1206, 2011.
- [108] Z. Wang, X. Zhou, J. Zhang, F. Boey, and H. Zhang, “Direct electrochemical reduction of single-layer graphene oxide and subsequent functionalization with glucose oxidase,” *The Journal of Physical Chemistry C*, vol. 113, no. 32, pp. 14071–14075, 2009.
- [109] L. Yang, D. Liu, J. Huang, and T. You, “Simultaneous determination of dopamine, ascorbic acid and uric acid at electrochemically reduced graphene oxide modified electrode,” *Sensors and Actuators B: Chemical*, vol. 193, pp. 166–172, 2014.

- [110] J. A. Quezada-Renteria, C. O. Ania, L. F. Chazaro-Ruiz, and J. R. Rangel-Mendez, “Influence of protons on reduction degree and defect formation in electrochemically reduced graphene oxide,” *Carbon*, vol. 149, pp. 722–732, 2019.
- [111] Z.-H. Sheng, L. Shao, J.-J. Chen, W.-J. Bao, F.-B. Wang, and X.-H. Xia, “Catalyst-free synthesis of nitrogen-doped graphene via thermal annealing graphite oxide with melamine and its excellent electrocatalysis,” *ACS nano*, vol. 5, no. 6, pp. 4350–4358, 2011.
- [112] M. C. Biesinger, B. P. Payne, L. W. Lau, A. Gerson, and R. S. C. Smart, “X-ray photoelectron spectroscopic chemical state quantification of mixed nickel metal, oxide and hydroxide systems,” *Surface and Interface Analysis: An International Journal devoted to the development and application of techniques for the analysis of surfaces, interfaces and thin films*, vol. 41, no. 4, pp. 324–332, 2009.
- [113] S. Fleutot, J.-C. Dupin, G. Renaudin, and H. Martinez, “Intercalation and grafting of benzene derivatives into zinc–aluminum and copper–chromium layered double hydroxide hosts: an xps monitoring study,” *Physical Chemistry Chemical Physics*, vol. 13, no. 39, pp. 17564–17578, 2011.

Appendix A

Data

Figure A.1: Chronoamperometry measurements for (a) Ni-P (b) GO-Ni-P (c)GO:Ni-P and (d) ERGO:Ni-P in 0.1 M KOH

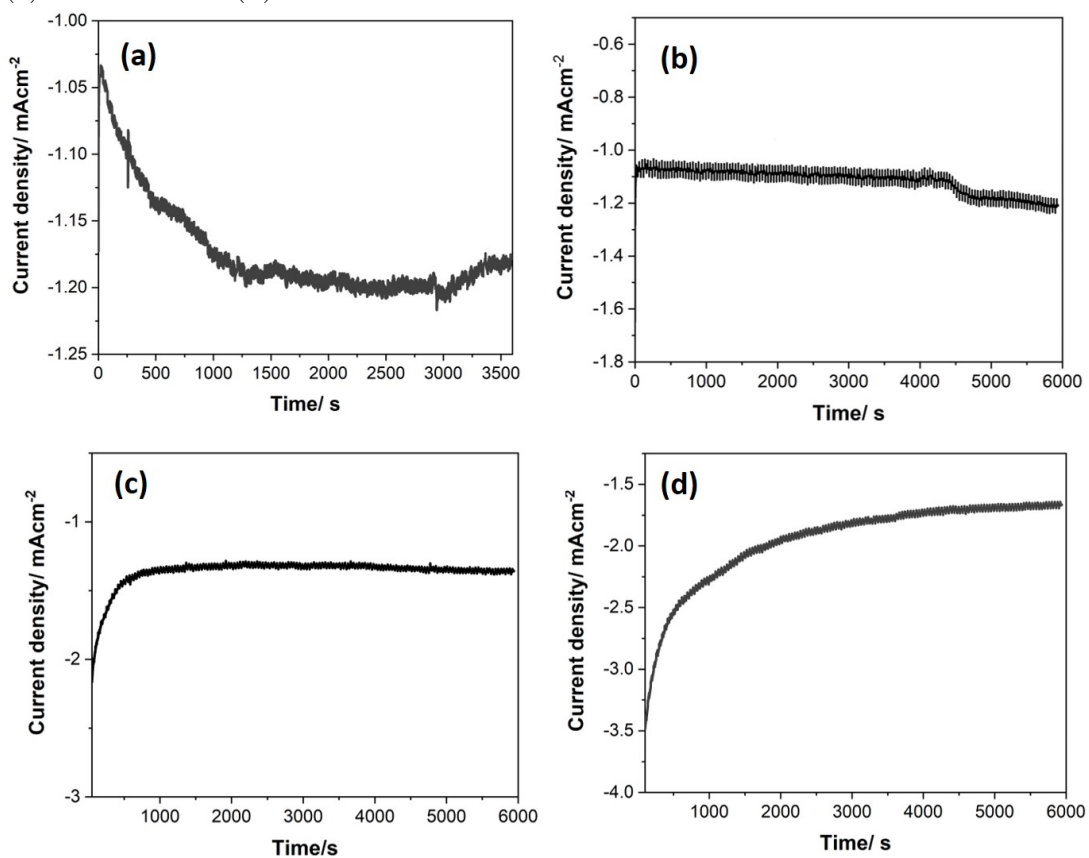


Figure A.2: EDX analysis showing elemental composition for (a) GO (b) ERGO and (c) ERGO:Ni-P

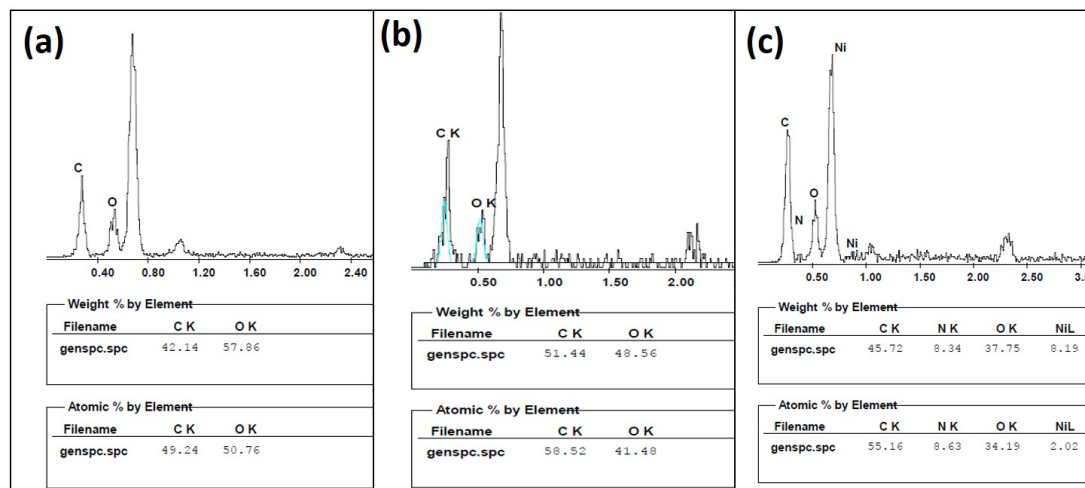


Figure A.3: Cyclic voltammety scans in 0.1 M PBS for (a) GO and (b) GO:Ni-P

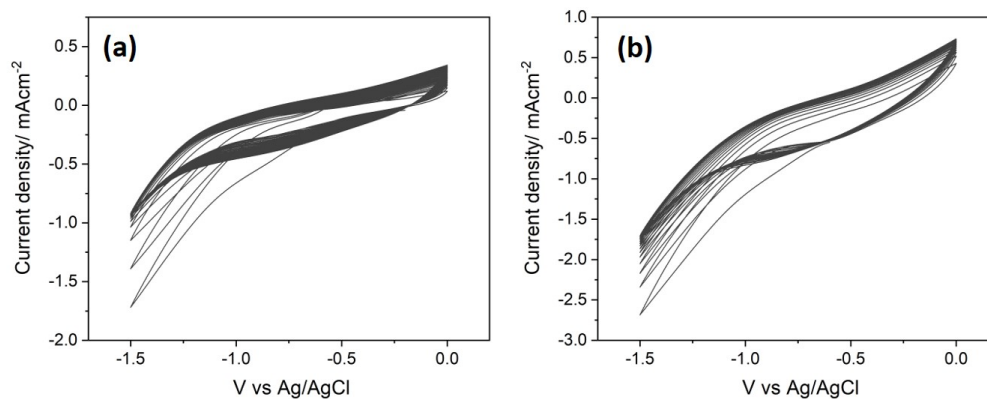


Figure A.4: ^1H NMR for TPP-4(OCH₃)

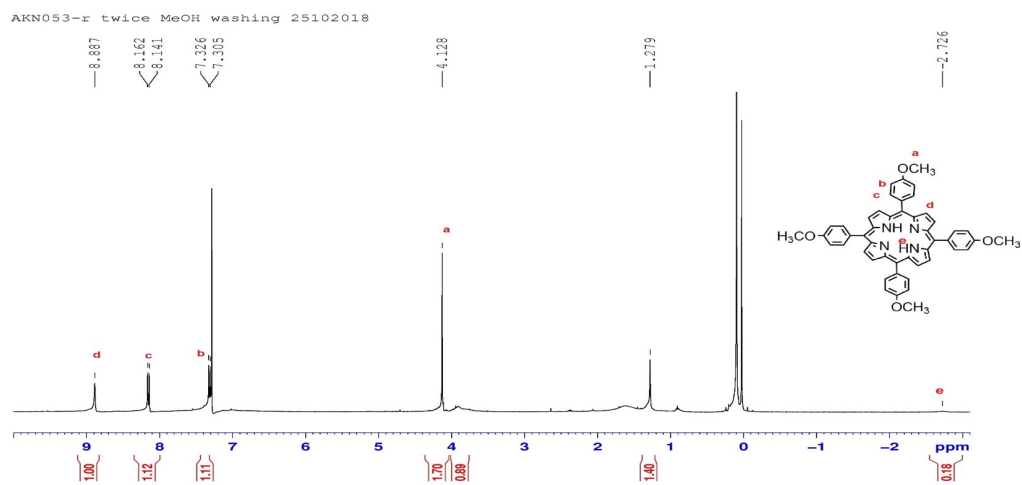


Figure A.5: ^1H NMR for TPP-4OH

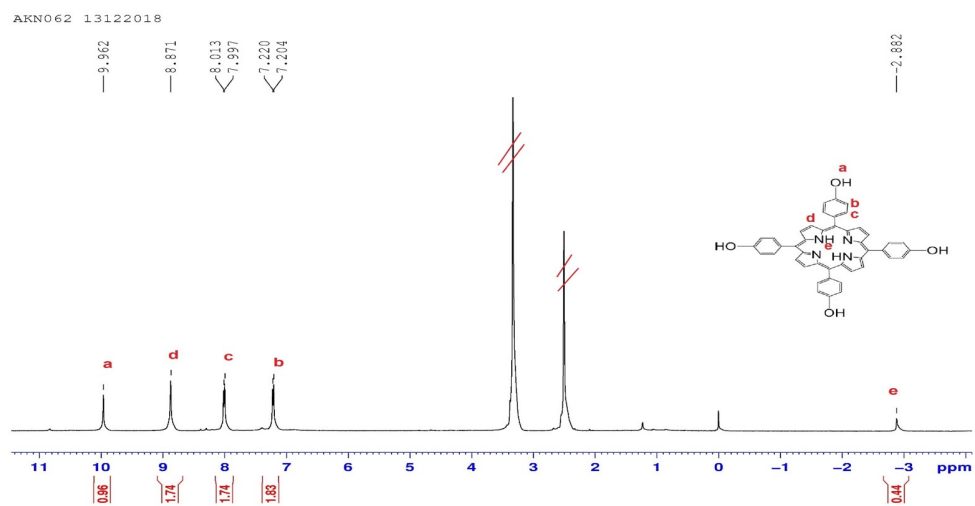


Figure A.6: ESI-MS for TPP-4OH

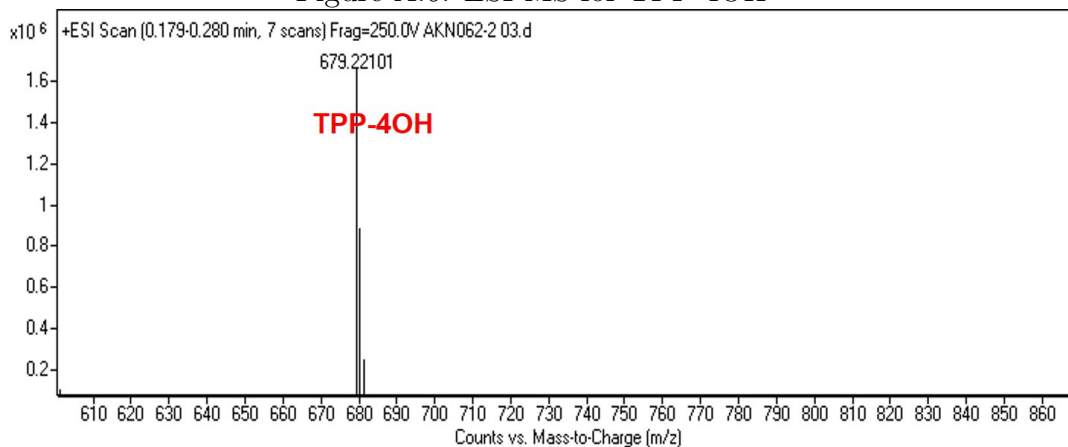


Figure A.7: ESI-MS for TPP-n(OC₃H₆Br)

